論文 / 著書情報
Article / Book Information

題目(和文)	生体分子からなる球状および環状構造体のナノエンジニアリングおよびその構造変換の観察
Title(English)	Nanoengineering of Spheres and Rings Made from Biological Molecules and Observation of Their Structural Transformations
著者(和文)	今村元紀
Author(English)	Motonori Imamura
出典(和文)	学位:博士（理学）, 学位授与機関:東京工業大学, 報告番号:甲第9727号, 授与年月日:2015年3月26日, 学位の種別:課程博士, 審査員:山口　雄輝,工藤　明,徳永　万喜洋,小畠　英理,上野　隆史
Citation(English)	Degree:, Conferring organization: Tokyo Institute of Technology, Report number:甲第9727号, Conferred date:2015/3/26, Degree Type:Course doctor, Examiner:,,,,
学位種別(和文)	博士論文
Type(English)	Doctoral Thesis

DOCTORAL THESIS

Nanoengineering of Spheres and Rings Made from Biological Molecules and Observation of Their Structural Transformations

by

Motonori Imamura

Department of Biological Information
Graduate School of Biological Science and Technology
Tokyo Institute of Technology
FY 2014

Supervised by:

Prof. Yuki Yamaguchi
Department of Biological Information
Graduate School of Biological Science and Technology,
Tokyo Institute of Technology, Yokohama, Japan

This research was conducted under the supervision of:

Dr. Jonathan G. Heddle
Heddle Initiative Research Unit
RIKEN, Wako, Japan

Judges:

Prof. Akira Kudo, Department of Biological Information
Prof. Makio Tokunaga, Department of Biological Information
Prof. Takafumi Ueno, Department of Biomolecular Engineering
Graduate School of Bioscience and Biotechnology
and
Prof. Eiry Kobatake, Department of Environmental Chemistry and Engineering
Graduate School of Interdisciplinary Science and Engineering
Tokyo Institute of Technology, Yokohama, Japan

Overcome the difficulty

困難にうちかて。

-Proverb written on the pencil from Yushima Tenjin-

Table of Contents

Acknowledgements

I would like to express my gratitude to my supervisor at Tokyo Institute of Technology, Prof. Yuki Yamaguchi and former supervisor, Prof. Akira Kudo for guiding me and supporting my working at the Heddle laboratory.

I am grateful to Dr. Jonathan G. Heddle, RIKEN for supervising my research with plenty of stimulating ideas since the fourth year of my undergraduate research; and all the lab members throughout the years who assisted my research and motivated me to pursue a doctoral degree and to study abroad, especially the members with whom I worked for a long period: Dr. Ali D. Malay, Dr. Kazuko Matsubara, Dr. Joanne Yu, Dr. Eleanor Banwell, Dr. Lin Ting-Yu, Dr. Soshichiro Nagano, Dr. Sachin Shah, Shama Shah, Maia Godonoga, Eitaro Kondo and Yumi Michishita.

I would like to thank RIKEN for providing financial support through the Junior Research Associate program and for the cutting edge research environment with their facilities as well as their support services.

It was a valuable opportunity to join the Education Academy of Computational Science (ACLS) from which I was able to take fruitful lectures related to computer science and attend international summer schools. Especially, many thanks go to Prof. Yutaka Akiyama and Dr. Yuichi Nagata for supervising my work as the committee leader of the summer school in 2012. Many thanks to all the staff, teachers and students I worked and studied with through these various activities.

I would like to thank Prof. Toshio Ando at Kanazawa University and his laboratory for the opportunity to learn the high-speed atomic force microscopy (HS-

AFM) technique at the Bio-AFM summer school. Especially, many thanks go to Prof. Takayuki Uchihashi for his support and guidance during that time as well as for contribution to my publication regarding the findings using HS-AFM.

I would like to thank Prof. Mathias Burst for supervising my three month internship at his lab in the Department of Chemistry at University of Liverpool, UK. I would like to thank all the lab members and the staff who supported my research in Liverpool, especially Hadjer Salmi, Dr. Marcin Grzelczak, Dr. Domagoj Belić, Dr. Casper Kunstamann-Oslen, Dr. Dan Bradley, Samantha Chadwick, Malte Strozyk, Oihane Fragueiro, Adam Davidson, Dr. Joan Comenge, Dr. Andy Bates and Jean Wood.

I wish to express my gratitude to Dr. Ali Malay, Riken for practical advice on my research since the first day of Heddle lab, as well as the work related with TRAP-cage research. In addition, I would like to thank Prof. Ulrich Simon and Dr. Annika Leifert, RWTH Aachen University for providing gold nanoparticles; Prof. Fumio Arisaka, Tokyo Tech, for conducting and advising Analytical Ultracentrifugation experiments.

I am deeply grateful to my parents Tetsu and Miyoko Imamura for supporting and encouraging my long educational career at the Tokyo Institute of Technology.

Finally, I would like to express my best gratitude to my wife, Allison Imamura, for all of her support and patience during my busy doctoral student life, and for giving me English advice and discussing my research ideas.

今村元紀

Wako, December 2014

Motonori Imamura

Abbreviations

GNPs	Gold nanoparticles (1.4 nm in **Chapter 2** and larger than 10 nm in **Chapter 3**)
MW	Molecular weight
Au1.4MS	1.4 nm (Au_{55}) GNPs stabilized with mono-sulfonated triphenylphosphine ligands.
Nanogold	Non-Functional 1.4nm GNPs purchased from Nanoprobes (NY, USA)
TRAP	*trp*-RNA binding attenuation protein (Derived from *Geobacillus stearothermophilus*)
TRAP-WT	Wild type TRAP
TRAP-K35C	Mutation of TRAP in which lysine residue 35 was replaced with cysteine
TRAP-cage	Hollow spherical protein which was made from TRAP-K35C with the addition of 1.4 nm GNPs
AFM	Atomic force microscopy
HS-AFM	High speed atomic force microscopy
DTT	Dithiothreitol (a reducing agent)
FFT	Fast Fourier transformation
HP-FFT	High pass frequency filter with FFT
AUC	Analytical ultracentrifugation

DNA	Deoxyribonucleic acid
DNA-MC	DNA minicircle (small closed circular DNA with 168 bp)
PS-DNA	Phosphorothioate modified DNA
BIDBE	*N*,*N*'-bis(a-iodoacetyl)-2,2'- dithiobis (ethylamine)
TEM	Transmission electron microscopy
SEM	Scanning electron microscopy
ESEM	Environmental SEM
AGE	Agarose gel electrophoresis
UV-Vis	Ultraviolet-visible spectroscopy
ss	Single strand
ds	Double strand
fps	Frame per second
Tris-HCl	tris(hydroxymethyl)aminomethane, pH was adjusted to 8 with HCl
PEG/PEG-alkane thiols	Polyethylene glycol-substituted alkane thiol (HS-C11-(EG)6-OH, MW: 468.69)
BSPP	bis-(para-sulfonatophenyl)phenylphosphine dihydrate dipotassium salt
DSC	Differential centrifugal sedimentation
TCEP	Tris-(2-carboxyethyl)phosphine

Chapter 1

Introduction

1.1. Top-down methods and their limitations

Experimentally, the birth of nano science may be Michael Faraday's experiment on gold nanoparticles in 1857 [1]. Conceptually, Richard P. Feynman's 1959 lecture "There's Plenty of Room at the Bottom" is one of the most inspiring lectures for nano-scientists[1]. Another conceptual beginning is the coining of the word "nanotechnology" in 1974 by Norio Taniguchi [2]. Since then, the most famous and successful nanotechnology has been the top-down fabrication technique, where nano-structures are made by carving out a pattern from the uniform surface of a larger material [3, 4].

Since Dr. Gordon Moore's famous prediction of decreases in transistor size in 1965 (so called "Moore's law") [5], the number of transistors on a chip has exponentially increased and the size of the components has been getting smaller and smaller due to the evolution of lithography methods. Intel Corporation's latest CPU (central processing unit) model Core™ M processors have 14 nm feature sizes, and even smaller node CPUs are expected to be produced within a couple of years with (or without) the next generation lithography method of 13.5 nm extreme ultraviolet [6, 7].

However, the technical barriers for fabricating such small components are increasing, and research and development costs for overcoming these barriers are increasing. More importantly, current top-down methods have almost reached the smallest possible limit because fabricating resolution depends on the wavelength of the light source for the lithography. These limitations have triggered a new trend called "More than Moore". This trend was proposed by International Technology Roadmap for

[1] http://www.zyvex.com/nanotech/feynman.html

Semicondoctors (ITRS) in 2005[2] and further discussed in a white paper[3]. In this post Moore era, the industry is not just pursuing smaller processing technology, but also integrating non-digital components into semiconductor technology, such as biosensors. Therefore, small non-digital units which can be combined with conventional digital units are required in the new semiconductor industry.

There are more drawbacks to this top-down method within the nanotechnology field in general. First, lithography methods are developed mainly for silicone-based nanotechnology, because it is semi-conductive, suitable for nano processing and stable, and other materials have not been explored in detail. Second, the structures are restricted to two dimensions. Finally, the structures are static, and dynamic nanoscale devices have not yet been studied very well.

Since top-down methods have been studied intensively within the past half a century, it is now time to consider bottom-up nano fabrication methods.

1.2. Bionano: Bottom-up nano fabrication with biomolecules

Bottom-up nano fabrication (fabricating nano-structures from smaller building blocks), has been studied using both non-biological and biological approaches. Non-biological approaches, such as carbon nanotubes, are promising but not without difficulties such as in the design and control of the nano structures produced [8].

[2] http://www.itrs.net/reports.html

[3] http://www.itrs.net/papers.html

Compared to non-biological approaches, the biological approach is promising. Biomolecules can self-assemble into regular, precise, functional nano structures in nature, and recent progress in biotechnology has enabled the structural design of biomolecules as well. Therefore, the bottom-up method utilizing target-shaped self-assembled biomolecular templates is a promising alternative to the top-down method for fabricating nano structures. Combining these self-assembled biomolecules with non-biological or inorganic particles may overcome limitations in fabricating designed arrangements of these particles at the nano-scale.

The study of the utilization of biomolecules for nanotechnology is called "bionano science" or "bionano technology" (hereafter, "bionano"). The word "Nanobiology" was first coined in a report "Research results report on developing basic technology for understanding bionano mechanics" in 1995 and 1998 from The Research and Development Bureau of The Science and Technology Agency, Japan [9, 10].[4] A Japanese textbook entitled "Introduction of Nanobiology" was published in 1994 by Nobuo Shimamoto [11]. In the same year, an article entitled "The stream of molecular biology" described nanobiology as a new trend in molecular biology written by Junichi Tomizawa [12], who is a pioneer of molecular biology in Japan.

Bionano originated as a branch of molecular biology and biophysics. Therefore, the beginning of bionano was focused more on describing and characterizing biomolecular building blocks using biophysical techniques such as protein X-ray crystallography and electron microscopy.

[4] Now this agency is called Ministry of Education, Culture, Sports, Science and Technology

Since bionano research began, various aspects of bionano research have been developed, and observation techniques in particular have progressed rapidly. Now, bionano not only aims at understanding biomolecular mechanics, but also attempts to design/build nano machines/structures using those biomolecules. To build designed nano machines from biomolecules is still challenging, but the more we understand the mechanism of biomolecules, the more bottom-up nano fabrication becomes feasible.

1.3. Why Biomolecules for Nanotechnology?

Our body is composed of biomolecules such as proteins, nucleic acids, lipids and sugars. These components are several to hundreds of nanometers (nm) in diameter. One nanometer is a 10^{-9} meter or one billionth (thousand millionth) of one meter, which is extremely small and invisible to the naked eye and conventional optical microscopes.

However, from a chemical point of view, biomolecules are large, complicated molecules. Compared to water molecules (H_2O) which have a molecular weight (MW) of 18 daltons (Da), the 8 nm ring protein in **Figure 1.1** has a molecular weight of ~92 kDa, composed of ~13 thousands atoms and self-assembled from 11 peptide chains (11 mer). Due to their small sizes, biomolecules require a lot of effort to observe or predict their character and structures.

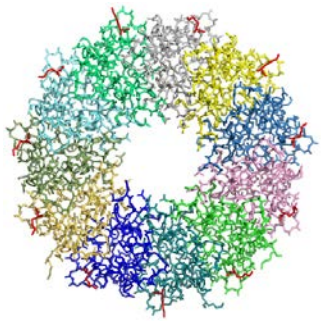

Figure 1.1. Crystal structure of an 11-mer ring protein (PDB 1UTV) [13]
This image is shown in stick view, with each subunits in a different color.

Although biomolecules are difficult to handle, there are two main advantages to using them for nanoscience. First, biomolecules have unique and useful characteristics that no other molecule or the top-down technique can achieve. For example, DNA polymerase derived from *Pyrococcus furiosus* (*Pfu*), used in the polymerase chain reaction (PCR), can elongate DNA with high fidelity (1 mistake per every 1.6 x 10^6 nucleotides [14]). In manufacturing companies, if the production meets a process capability index (Cpk) = 1.67 or a failure ratio of 0.57 ppm (1 mistakes per 1.8 x 10^6) it is considered as good quality production for safety or critical process. Therefore, DNA polymerase is a high-fidelity nano machine. Another example is the ability of biomolecules to self-assemble into larger structures from simple building blocks. For example, Tobacco mosaic virus (TMV) is a tube-shaped assembly, 18 nm in diameter and 300 nm in length. It is composed of 2130 coat proteins and a 6400-nucleotide RNA. In comparison, a single monomer of the coat protein is just 2 nm x 2 nm x 7 nm. Due to the ability of the TMV coat protein to precisely assemble into a stable tube structure, it has been studied as a template for biomineralization [15]. Biomolecules can also be scaled up easily. DNA can be amplified with PCR to produce µg to mg amounts in the lab, and protein can be expressed in *Escherichia coli* (*E. coli*) and purified typically in milligram order. It is also possible to purchase designed sequences of DNA at a relatively low price.

The second advantage is the dramatic progress in the knowledge base and technology of this field. The structure of DNA was first solved in 1953 by James Watson and Francis Crick [16]. Myoglobin was the first protein structure to be solved in 1958 by John Kendrew and his colleagues [17]. Since then, the structures of biomolecules have been solved at an increasing rate. Now, more than 100,000 protein and nucleic acid structures have been registered at the Protein Data Bank (PDB). In addition to the huge

amount of structural information, it is also possible to predict unknown protein structures from comparative modeling or *de novo* simulation. The latter method is restricted to small proteins because it requires huge calculations, which are still difficult even with current supercomputers.

1.4. Nanoengineering of DNA and protein

1.4.1. DNA

The recent progress in DNA nanotechnology has made it possible to self-assemble it into arbitrary shapes in two or three dimensions. This technique was first started by Nadarian Seeman in 1982 [18-20]. The most well-known two-dimensional DNA structure "DNA origami" was introduced by Paul Rothemund in 2006 [21]. DNA origami was subsequently utilized to make DNA molecules of various three-dimensional structures [22], including nanorobots [23]. These results demonstrate the benefit of the programmable structure of DNA. However, the problem with the DNA origami technique is that it requires hundreds of short single strand (ss) DNA (stable strands) and one long ssDNA, which are very expensive (although the price of synthesized DNA is becoming cheaper). By using smaller numbers (types) of DNA, two-dimensional or three-dimensional structures have also been made [24, 25]. Reducing the number of DNAs may restrict the variation of structures, but pursuing simplicity is necessary for practical application to nanotechnology, which requires robustness, reproducibility and low cost.

1.4.2. Protein

The benefit of using protein is that there are unlimited preexisting structures in nature. Therefore protein nanoengineering starts with existing proteins in nature, whose

structures are registered in the Protein Data Bank (PDB). The drawback of protein compared to DNA is its instability. Since the life cycle of protein in nature is usually much shorter than that of DNA, protein tends to lose its functional structure over time. However, there are unusually stable proteins such as those derived from thermophilic bacteria or viruses. These stable structures usually possess symmetry within their structures. Therefore, nanobio scientists usually work on symmetrical proteins, such as ring-shaped, rod-shaped and sphere-shaped proteins.

The symmetry of protein is categorized into four types: Cyclic (C), Dihedral (D), Cubic (C) and Helical (H) as seen in **Figure 1.2** [26]. With cyclic proteins it is possible to find identical structures by rotation. For instance, the ring protein in **Figure 1.1** has the identical structure after each rotation of 360/11 degrees. Therefore this protein has "C11" symmetry. Dihedral proteins are also ring-shaped but with higher symmetry, i.e. possessing the same cyclic symmetry at the opposite side of the cyclic symmetry axis (cyclic symmetry + 2-fold symmetry). Cubic symmetry consists of 3-fold symmetry and other symmetries which are not perpendicular to each other. Cubic symmetry is further categorized into Tetrahedral (T) (3,2 fold symmetries); Octahedral (O) (4,3,2-fold symmetries); and Icosahedral (I) (5,3,2 fold symmetries) symmetries. Helical symmetry has a helix axis, which makes a rod-shaped protein. Because of the symmetry in their structure, these proteins are simple, functional and stable. For example, protein capsids of many viruses employ icosahedral symmetry to protect and carry their genome[5].

[5] http://www.rcsb.org/pdb/staticHelp.do?p=help/viewers/jmol_symmetry_view.html

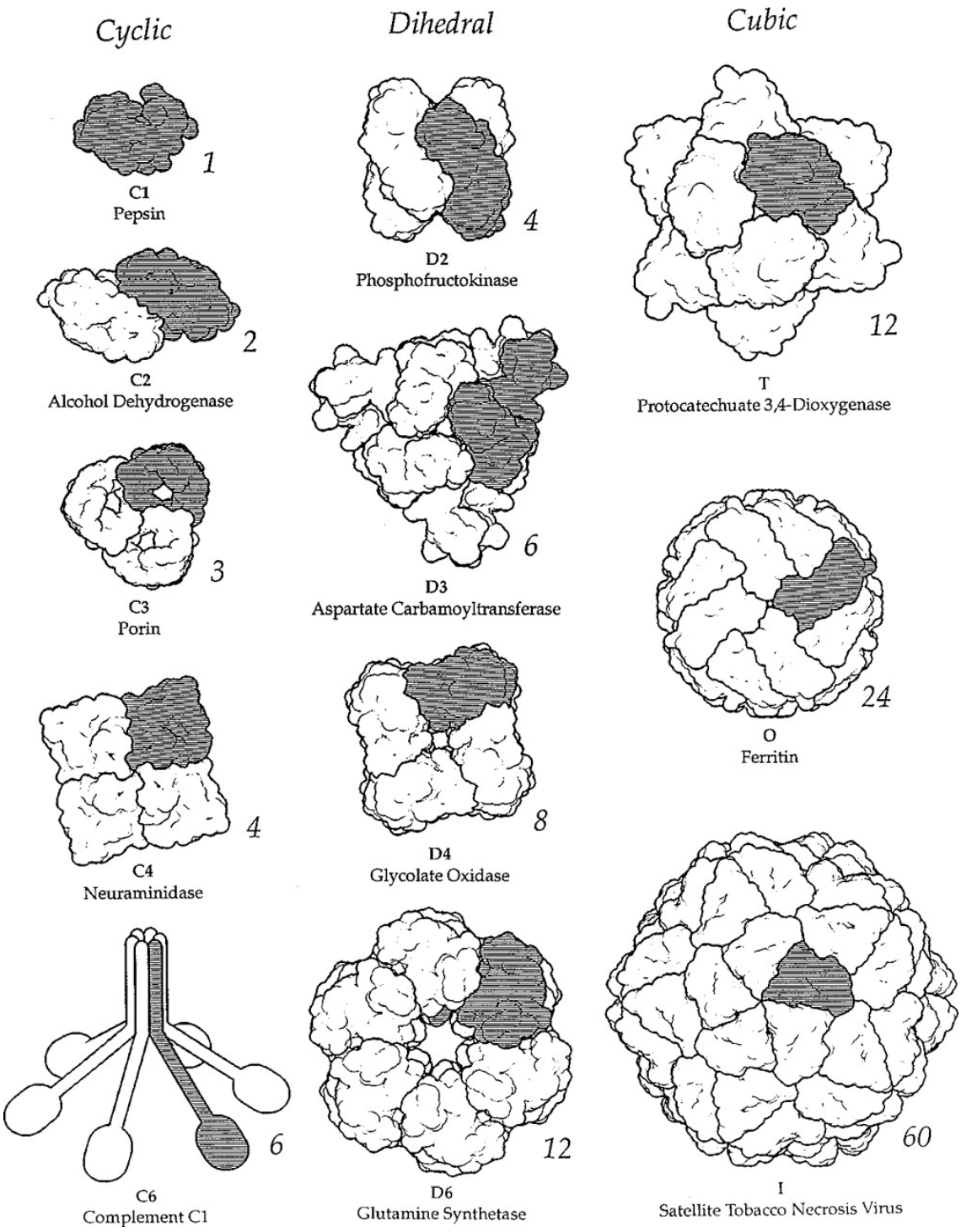

Figure 1.2. Protein symmetry.
Reprinted from Figure 1, page 110, Annual Reviews, Vol. 29, David S. Goodsell and Arthur J. Olson, *Structural Symmetry and Protein Function*. Copyright © (2000), with permission from Annual Reviews [26].

By selecting a very stable protein and mutating its amino acid sequence, it is possible to engineer the protein further for a specific purpose. The protein in **Figure 1.1** (also derived from thermophilus protein) was previously mutated to have cysteine in the central hole to capture gold nanoparticles [27], and the 11-mer symmetry was changed into 12 mer by tandemly connecting two, three, or four subunits [28]. Mutating the top and bottom faces of the 11-mer ring led to formation of a tube structure (stack of rings). Mutating the external "rim" of the protein with cysteines led to formation of a sphere upon addition of gold nanoparticles [29, 30]. It is also becoming possible to design protein nanostructures *ab initio* [31] or predict possible structural changes [32].

1.5. Observation of biomolecules

In any technique, spatial and temporal resolutions are always in conflict with each other. Among high temporal (>5 frame per second) imaging techniques, recent progress in microscopes enables us to observe "atomic resolution" live imaging of non-biological molecules in "high vacuum conditions" using, for example, a transmission electron aberration–corrected microscope [33]. It is also possible to observe "nano-scale resolution" movies of biomolecules with high-speed atomic force microscopy in "liquid condition" **(Chapter 2**). However, "atomic resolution" live images of biomolecules in "liquid condition" is still challenging. Therefore, to know the detail structure and behavior of biomolecules is a challenging topic. Because biomolecules are nanometric, fragile and flexible, a combination of several observation techniques is required to obtain more insights about them. Even though one technique may show a characteristic structure, it is

necessary to confirm the finding with other methods (not only structural observation) to compensate for the uncertainties of each observation method.

Here, I would like to compare X-ray crystallography, transmission electron microscope (TEM), atomic force microscope (AFM) and high-speed AFM (HS-AFM) from my experience (**Table 1**). These four techniques complement each other when it comes to identifying the structure of protein or DNA.

For a protein sample in nanobiology, it is better to start with a sample whose X-ray crystal structures are already solved, because to solve the structure usually takes several years or may not be possible at all in some cases. TEM is the most commonly used technique to observe samples produced in different conditions, because the sample preparation and observation techniques are well established, and obtaining relatively high resolution images can be carried out quickly. After the sample conditions are confirmed by TEM and electrophoresis, there are various observation methods to investigate further. I used HS-AFM to understand the structural dynamics of the protein of my interest (**Chapter 2**). If the protein structures changed or were considered to change with mutation, the highest resolution structural information comes from X-ray crystallography. However, it is not possible to obtain protein crystals with all samples, because making pure crystal requires a highly pure and homogeneous sample and some proteins may not crystallize.

For a DNA sample, the structures are usually designed or are easy to predict, therefore the observations are usually done with AFM. Because DNA is just 2 nm in width, it is difficult to view under TEM unless the DNA is forming a two-dimensional or three-dimensional structure. AFM is very sensitive to the height of samples on a surface

and is commonly used for observing DNA structures on the mica surface, which is atomically flat.

Besides the techniques introduced here, there are many more techniques for viewing high-resolution images such as high resolution electron microscope, NMR (nuclear magnetic resonance), cryo-electron microscopy and super-resolution fluorescent microscopy [34].

Table 1. Comparison of observation techniques for biomolecules

Methods	Spatial resolution	Temporal resolution	Suitable for DNA or for Protein	Limitation	Benefit
X-ray crystallography	0.1-0.5 nm	NA	Both	The most difficult technique in this list.	Highest resolution and a trustable structure can be obtained.
80 kV TEM	2-5 nm	1 s to 1 min	Protein	Staining and drying of sample required; high energy electron beam; vacuum conditions; transmitted electron density images frequently cause artifacts.	Low technical barriers
AFM	1-10 nm in x, y; 0.1-1.0 nm in z dimension	1-5 min/frame	Both	Sample must be on a flat surface. Takes a lot of time and effort to obtain good images in liquid conditions.	Liquid observation is possible, contrast for flat sample is high
HS-AFM	1-5 nm in x, y, 0.1-0.5 nm in z dimension	0.1-20 fps	Both	The sample must be on a flat surface. Only the top surface of the sample can be observed	Liquid observation, high temporal and high resolution are possible

1.6. High-speed atomic force microscopy

Amongst the observation techniques described above, I used high-speed atomic force microscopy in **Chapter 2.** Atomic force microscope (AFM) has high spatial resolution especially in the z direction and can observe biomolecules in liquid conditions. Tapping mode AFM can scan the sample surface softly, so it is suitable for biological samples. The basic mechanism of high-speed atomic force microscopy (HS-AFM) is the same as for tapping mode atomic force microscopy (AFM). The difference between them is in the scan speed. In contrast to conventional AFM, HS-AFM can take images more than 1000 times faster (1-5 min per image for conventional AFM, 0.05-1 seconds per image for HS-AFM). In addition to the high temporal resolution; high-spatial resolution (1-2 nm in x, y dimensions, 0.1-0.2 nm in z dimension [35]) is possible using sharp tips that are fabricated by electron-beam deposition (EBD) and plasma etching. In addition, HS-AFM is designed specifically for liquid observation (for many conventional AFMs, it is much more technically difficult to observe in liquid than in air). These advantages makes HS-AFM one of the most outstanding techniques for observing biomolecules. Since HS-AFM data is more like a "movie" than an "image", the imaging speeds are usually expressed in frames per second (fps). For example, 0.05 second per image is expressed as 20 fps.

1.6.1. How does HS-AFM achieve high speed[6]?

To achieve such a high-speed observation with a minimal tip force to the sample, considerable development of atomic force microscopy has been carried out, most notably

[6] This chapter references citation 36. Ando, T., T. Uchihashi, and T. Fukuma, *High-speed atomic force microscopy for nano-visualization of dynamic biomolecular processes.* Progress in Surface Science, 2008. **83**(7-9): p. 337-437, 37. Uchihashi, T., N. Kodera, and T. Ando, *Guide to video recording of*

by the Ando group in Kanazawa University, Japan [36]. As shown in **Figure 1.3**, tapping mode AFM is composed of piezo driver, scanner (composed of x, y and z piezoelectric actuators), cantilever, laser diode and lens, photodetector, feedback control system, and monitor. In the HS-AFM system, most of these units are replaced by the units capable of operating 10-1000 times faster.

AFM is a type of Scanning probe microscope (SPM), the images of AFM are obtained from the scanning information of the AFM probe (or "AFM tip"). If there are 100 pixels along the y axis (number of scan lines: *N*), the AFM tip scans the sample 100 times (only left-to-right or right-to-left direction is recorded). This means that if the frame speed is 20 fps, AFM tip scans 2000 times per second (2 kHz). If the image also has 100 pixels in the x direction, AFM tip should move faster than the frequency of 200 kHz, and feedback loop of the AFM should also target around these values.

structure dynamics and dynamic processes of proteins by high-speed atomic force microscopy. Nature protocols, 2012. **7**(6): p. 1193-206.

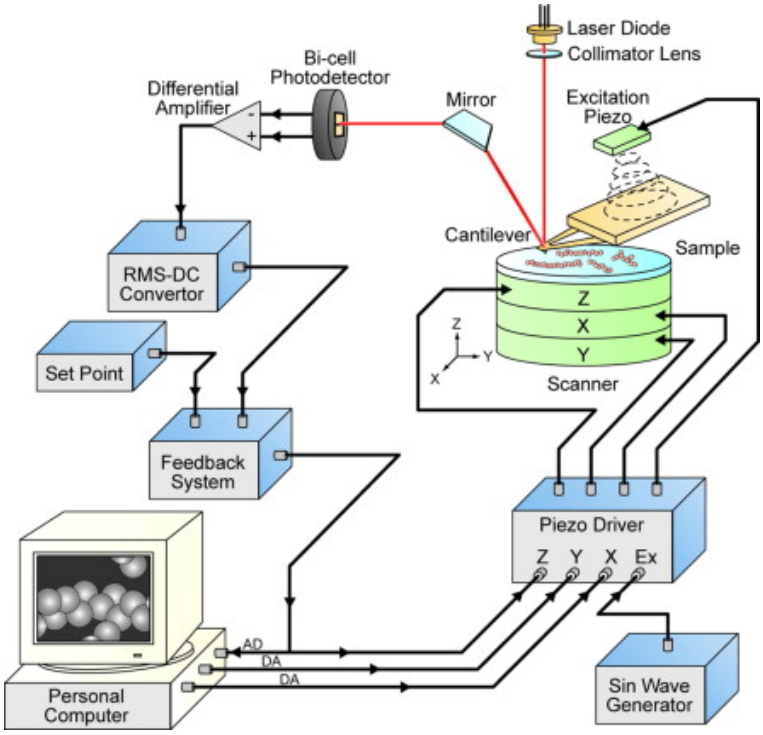

Figure 1.3. Tapping-mode AFM system. [7]

[7] Reprinted from Figure 1, Progress in Surface Science, Vol. 83, Toshio Ando, Takayuki Uchihashi and Takeshi Fukuma, *High-speed atomic force microscopy for nano-visualization*, Page341, Copyright (2008), with permission from Elsevier.

Resonance frequency *f*, spring constant *k*, and tapping force *F* of a rectangular cantilever shown in **Figure 1.4** can be estimated in the following **equations.**

$$f = \frac{d}{L^2} C_2 \quad \textbf{(1)}$$

$$k = \frac{w d^3 C_1}{L^3} \quad \textbf{(2)}$$

$$F = k C_3 \sqrt{A_0^2 - A_{sp}^2} \quad \textbf{(3)}$$

where, C_1 and C_2, C_3 are constants derived from the materials (Young's modulus, density and quality factor of resonance sequence, respectively). A_0 and A_{sp} are free amplitude and set point amplitude (the amplitude when tapping the sample) and *w*, d and L are as shown in **Figure 1.4**. From these three equations, to meet both high frequency and weak tapping force requirements, the cantilever needs to be as small as possible.

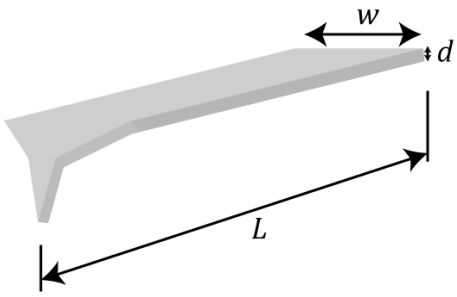

Figure 1.4 HS-AFM cantilever

HS-AFM's cantilever is extremely small compared to a normal AFM tip (*L* = 9-10 µm, *w* = 2 µm, *d* = 90 nm; BL-AC10DS, Olympus, Tokyo). Thanks to this small cantilever, a high-resonant frequency is possible (f_c = 0.6 MHz in water) meeting the requirements for the HS-AFM observation. As a comparison, the typical frequency of

AFM tips for non-high-speed AFM is about 50-200 kHz in air (frequency in liquid is usually l ~1/3 of the frequency in air).

The most difficult part of developing HS-AFM was mentioned as mechanical [36], that is, piezoelectric actuator does not have high frequency. At the resonance frequency of the piezoelectric actuator, it is hard to control precisely the vibrating piezoelectric actuator. This problem was solved by putting the same piezoelectric actuator in the counter direction. Two z-piezoelectric actuators vibrate in opposite directions, to cancel the vibration (**Figure 1.5**).

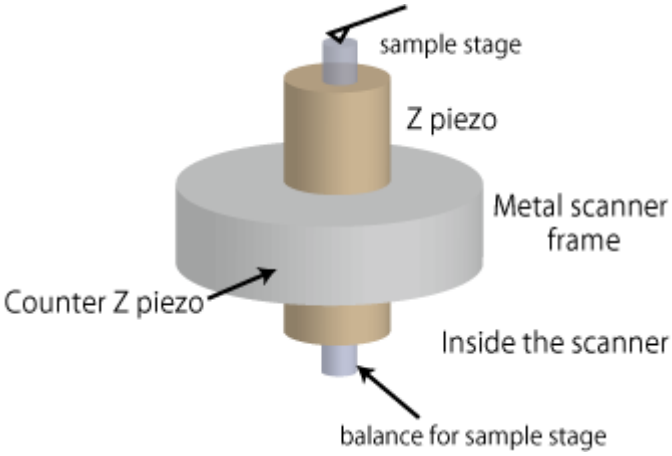

Figure 1.5 The scheme of z piezo and counter z piezo [36].

Since HS-AFM first observed the dynamics of biomolecules in 2001 and 2002 [38, 39], this technique has steadily improved and has become more reliable [35]. In addition to the high temporal and high lateral resolution under liquid condition, a wide range of physiological buffer condition is allowed. It is also possible to add small amount of samples or buffers during observation ([40], **Chapter 2**).

1.7. Gold Nanoparticles

In some cases, the biomolecule itself does not have the required properties for a certain nanotechnology application. Therefore, combining it with a metallic particle is necessary to make functional nano structures. One promising candidate is the gold nanoparticle (also called gold colloids) since it is stable and has useful properties.

The most famous use of gold nanoparticles (GNPs) in history is stained glass. The still beautiful colors of stained glass made hundreds of years ago suggest that GNPs can be very stable and have different characteristics from the bulk. Scientific studies with GNPs were undertaken 150 years ago by Faraday, who examined how gold particles react with light [1]. The synthesis of GNPs has been made possible since the 1950s by the techniques such as the Turkevich-Frens method [41-43] and the Brust method [44]. The applications of GNPs are also studied in a variety of fields such as nanotechnology, chemical or bio sensors; and medical treatment [45-47]. This is because GNPs can be functionalized with stabilizing ligands and because the absorption of visible light wavelengths is different depending on the size of the particles or the dispersity (so-called surface plasmon absorption) [48]. Recently, the oxidative activity of small (~1.4 nm) GNPs has gained attention [49-53]. Given the established characters of large (>5 nm) GNPs and the new findings for small (<5 nm) GNPs, GNPs have the potential to be combined with biomolecules to obtain new functional nano structures [54-56].

1.8. Optical Metamaterials[8]

My interest for GNPs-combined biomolecules is in their application as a "metamaterial". In nature, the path of the light bends (refracts) between glass, water and air, but never refracts negatively (refraction index in vacuum is 1.0; water 1.3; glass ~1.5)

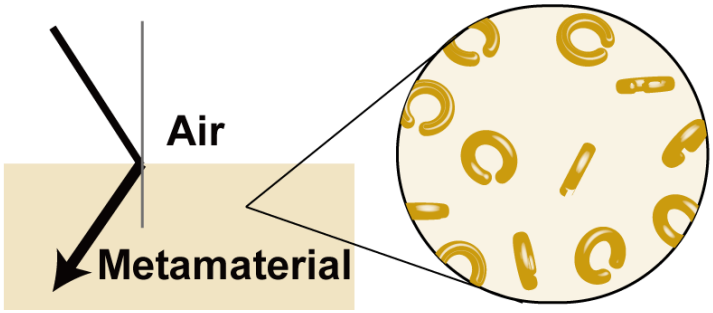

Figure 1.6. Refraction of light in metamaterials and its component.

In comparison, metamaterials are suggested to refract light negatively (or with a smaller index than in vacuum) as shown with the arrow in **Figure 1.6** [57]. The index of refraction ($\boldsymbol{n}$) is shown in **Equation (4).**

$$\boldsymbol{n} = \sqrt{\boldsymbol{\varepsilon}} \times \sqrt{\boldsymbol{\mu}} \qquad \textbf{(4)}$$

Where ε is relative permittivity, and μ is relative permeability. Briefly, ε shows how much the material responds to an electric field, and μ shows how much the material responds to a magnetic field. Visible light is a type of electromagnetic wave; therefore **Equation (4)** describes how the material responds to the electromagnetic wave of light.

[8]This section is referencing to the following book and literature.

Teruya Ishihara, 2007 "Metamaterial:New Technology and Its Application", CMC Publishing Co.,LTD

Takuo Tanaka, 2013 "Optical metamaterials and metal nanoparticles" Bulletin of Solid State Physics and Applications, Japan Society of Applied Physics.

Usually, both ε and μ are positive. μ is always +1 in the frequency of the visible light. A material with negative ε makes the equation an imaginary value. This means that the amplitude of light decays exponentially, or that the material does not transmit the light. Metal is the representative of a material with negative ε. When both ε and μ are negative, refraction n is also negative. This negative permittivity and permeability are suggested to cause various interesting phenomena. Reflection, scattering, absorption and refraction are all caused by the reaction to the electric part of the light, i.e. response of permittivity (ε). Therefore, if we can shift the permeability (μ) value from 1, an unusual phenomenon should occur, and it should be possible to combine various ε and μ values.

To shift the permeability (μ) from 1, the material should respond to a high frequency of visible light (4 – 7.5 x 10^{14} Hz or 0.4-0.75 peta Hz). The reason that μ is 1 is because there are no materials which can respond to such a high frequency in nature. Since it was first suggested by Pendry in 1999 [58], various metallic nano structure units have been reported to respond to the permeability. One famous unit is the split ring resonator (SRR) [59]. A SRR has ring structure with one or more than one splits as shown in the circle in **Figure 1.6** (This figure shows one split SRR only). The ring structure works as "coil"(*L*), and the split works as "capacitor" (*C*). The combination of "*L*" and "*C*" (so called LC circuit) makes a SRR possible to respond to a certain frequency of light. SRRs need to be smaller than the wavelength of light to react with the frequency of visible light. Although metamaterials are constructed from metallic nano structures, individual SRR units are too small for light (400 – 700 nm) to interact with, but a large number of SRR units together can interact with light and are recognized as materials with special properties; therefore they are collectively called a meta "material" instead of meta

"structure." In addition, it is preferred to array SRR units randomly as shown in **Figure 1.6** in order to have an isotropic reaction to the light as a whole. In comparison, photonic crystals are composed of periodic nano structures (such as holes on silicon), whose periodicity and structures are approximately a few wavelengths of light. By changing the pattern of periodic nano structures, it is possible to manipulate the path of the light. The periodic arrangement of these nano structures in a photonic crystal is recognized by light as structures, rather than as materials. Photonic crystals and metamaterials have similar (or sometimes the same) effect against light, but the arrangement pattern is important in the photonic crystal, while it is not necessary for metamaterials [60][9].

Currently, such metallic structures are made using a top-down method. However, to fabricate such a material at the nanoscale, which is necessary to respond to visible light, is still challenging, and to fabricate millions or billions of these nano structures to make a "material" is not practical using the top-down technique. $1cm^3$ of MTMs requires trillions of units if each unit is arrayed 1000 nm apart in x, y and z directions. Therefore, using a bottom-up method employing biomolecules with GNPs could be the solution for this problem.

1.9. Aim of the research

The properties of GNPs at the nanoscale make them attractive for construction of nanometric materials including metamaterials. To do this GNPs may need to be arranged with specific geometries and spacings. As some biomolecules can self-assemble into

[9] http://www.brl.ntt.co.jp/group/ryouna-g/index.html

regular nano structures, attachment of GNPS onto such biomolecules could result in an ideal building block for nanotechnologies, possibly possessing unusual properties very different from their original characteristics.

In the Heddle lab, attempts to interact GNPs with a circular protein TRAP (*trp*-RNA binding attenuation protein) resulted not in a SRR unit structure of a metamaterial by utilizing biomolecules as a template of GNPs but rather, when a mutant of the TRAP was used, a dramatic protein structural change occurred [30]. This resulted in the assembly of a larger hollow spherical structure (TRAP-cage). While different from the initial purpose, this is an unprecedented finding, and raised many scientific questions. Understanding the mechanism of the TRAP-cage formation became a major aim in this thesis. Initial characterization of TRAP-cage and condition of TRAP-cage formation was reported [30] (Summarized in **Chapter 2.1.2**). My project focused on investigating the structural details and dynamics of TRAP-cage assembly via high-speed atomic force microscopy (HS-AFM) in **Chapter 2**.

I returned to the original idea of using a biomolecule to template GNPs using annular small DNA structures (DNA minicircles) to achieve initial aim. Unlike the TRAP protein, DNA minicircles do not break down easily since the entire structure is covalently connected. In addition, phosphorothiorate-modified DNA (PS-DNA) can be used to attach GNPs to the DNA backbone in a programmable fashion. (**Chapter 3**)

Chapter 2

High-Speed AFM Observation of Protein Structural Transformation

2.1. Introduction

Chapter 2 is based on the paper, Imamura, *et al.*, *Nano Letters*, 2015 [40][10].

2.1.1. *Geobacillus stearothermophilus* TRAP

TRAP (*trp*-RNA binding attenuation protein) is found in the Gram-positive bacterium, *Geobacillus stearothermophilus (G. stearothermophilus)*, whose name was recently revised from *Bacillus stearothermophilus* [61, 62]. As the name indicates, this species can survive extreme environments such as hot springs, deserts and the bottom of the ocean. *G. stearothermophilus* is part of the same family as the well-known *Bacillus subtilis* (*B. subtilis*), which is commonly found in soil, a variant of which is used in the Japanese traditional fermented soybean food "*Natto*". The thermophilic nature of *G. stearothermophilus* has been used as a test for the sterilization processes. Recently, proteins derived from *G. stearothermophilus* have been utilized for molecular biology, e.g. DNA polymerases for loop-mediated isothermal amplification (LAMP) [63].

TRAP proteins derived from *B. subtilis* and *G. stearothermophilus* has been well studied since the first identification of the sequence of *B. subtilis* TRAP in 1990 [64]. The crystal structures of TRAP from both species have been determined [13, 65-69], and the biological role has been elucidated [70-72]. Both TRAP proteins are thermostable and their amino acid sequences are very similar (~75% identity[66]), but *G. stearothermophilus* TRAP has higher thermostability than those of other well-known *Bacillus* species [73]. This protein does not undergo aggregation even after boiling [74]. Because of this robustness and its characteristic well-known ring structure, TRAP has

[10] Adapted with permission from (Imamura, *et al*., *NanoLett*.). Copyright © (2015) American Chemical Society.

been used for bionano science via engineering the amino acid sequence. In 2007, Heddle *et al*. mutated Arg 66, which is located in the inner holes of the ring, into cysteine (R66C) to capture GNPs in the central cavity. By adding titanium-binding peptide sequences at the N- or C-terminus, TRAP was able to place GNPs on a titanium substrate [27]. Since I used only *G. stearothermophilus* TRAP in this thesis, "TRAP" in this thesis refers to TRAP derived from *G. stearothermophilus*.

2.1.2. Ring protein TRAP transforms into a sphere in the presence of gold nanoparticles

Since *B. subtilis* TRAP has a longer history than *G. stearothermophilus* TRAP, amino acid sequence numbering is sometimes based on *B. subtilis*[11]. In this thesis (and the papers concerning TRAP-cage), amino acid sequences are numbered directly from the sequence of *G. stearothermophilus* TRAP as shown in **Figure 2.1**.

Figure 2.1 Amino acid (aa) sequence of *G. stearothermophilus* TRAP wild type (74 aa)

By using a similar approach to that used in the R66C mutant to capture GNPs in the center of TRAP, Lysine (K) 35 located at the outer rim of TRAP was mutagenized to cysteine (K35C) in order to attach GNPs. In a previous report, this TRAP-K35C mutant resulted in the assembly of a large, hollow spherical protein superstructure in the presence of 1.4 nm Au_{55} gold nanoparticles (GNPs), while there was no effect on the ring structure in the absence of GNPs (**Figure 2.2 a-d**, page 40) [30]. In that report, this superstructure

[11] R66C mutant in the previous example is equivalent of R64C in this thesis.

was called a “capsid-like structure (CLS)”, but in this thesis it will be called “TRAP-cage”.

From this unexpected result, many interesting questions arose. Since such gold-induced protein structural change has never been reported before, the mechanism of the structural change was unknown. Well-known effects of GNPs on protein include the formation of “corona” structures (where protein nonspecifically aggregates around GNPs) and protein aggregation. In the previous report, characteristics of TRAP-cage and its formation conditions were discussed [30]. In summary:

- TRAP-cage has two distinct diameters, either ~16 nm or ~20 nm. When the concentration of gold nanoparticles is higher than the protein concentration, TRAP-K35C tends to form the smaller size. The larger structure is investigated in this thesis.
- The TRAP-cage formation reaction is specific. The size of GNPs has to be 1.4 nm in diameter, TRAP needs to have K35C mutation, and the buffer pH has to be ~8. TRAP-cage did not form with anything larger (10 nm) or smaller (undecagold, 0.8 nm). R56C, substitution of an amino acid in vicinity of K35 to cysteine, also did not work. Moreover, pH $\leq$ 7 or $\geq$9 did not allow the formation of regular TRAP-cage structure.
- GNPs are sometimes, but not always, associated with the sphere structure, suggesting a nonspecific, stochastic binding as shown in **Figure 2.2 e**. The fact that GNPs are not absolutely required suggests a catalytic role for GNPs [50]. As I mentioned in **Chapter 1.7,** the catalytic activity of GNPs is a recent topic of interest for small GNPs.

In addition, further characteristics were revealed in a follow-up study by Dr. Ali Malay (*manuscript in preparation*).

- The TRAP-cage structure is highly thermostable, like the original TRAP ring.

- TRAP-cage is disassembled and reverted back to the original TRAP ring structure with the addition of a reducing agent (DTT).

Although production and basic characterization of TRAP-cage has been achieved, much remains to be studied including its detailed structure and dynamics, i.e. the mechanism of TRAP-cage formation remains unknown. Since recent progress in high-speed atomic force microscope (HS-AFM) developed in Prof. Ando's group, Kanazawa University showed its usefulness in observing dynamic protein activities (**Chapter 1.6**), in this thesis, I used HS-AFM to investigate the TRAP-cage structure and dynamics with the kind support of the Ando group in Kanazawa University, especially Assoc. Prof. Takayuki Uchihashi.

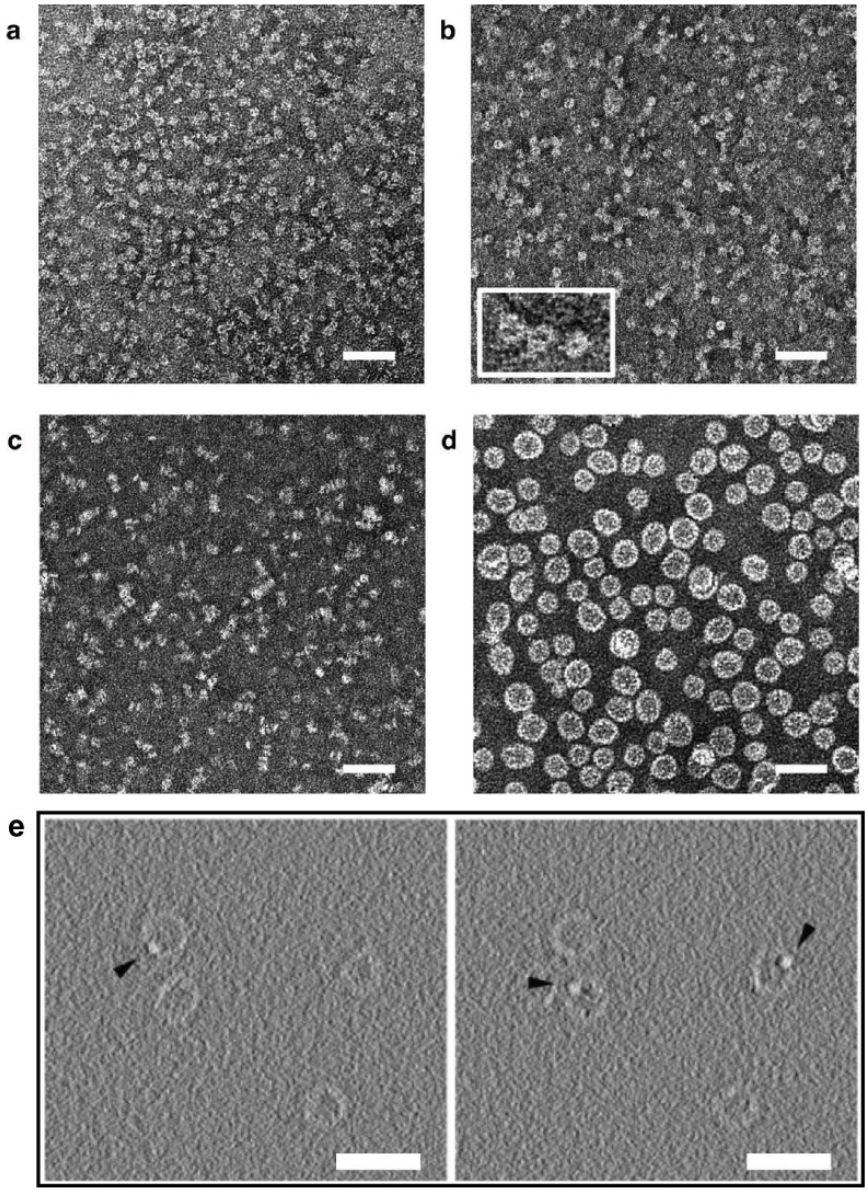

Figure 2.2 Addition of 1.4 nm GNPs allows the formation of TRAP-cage from TRAP-K35C but not from TRAP-WT. [12]
TEM image of (**a**) TRAP wild type (TRAP-WT); (**b**) TRAP-K35C (inset, region enlarged 3.5 times); (**c**) TRAP-WT incubated with 120 µM 1.4 nm GNPs; (**d**) TRAP-K35C incubated with 120 µM 1.4 nm GNPs. (**e**) Cryo-EM derived sectional views of the same TRAP-cage particles (different depth). Large particles of approximately ~7 nm are indicated as black arrow. Scale bar = 40 nm.

[12] Adapted with permission from Figure 2 (page 2057) and Supporting Figure (page 9), Malay A.D. *et al*., *Gold Nanoparticle-Induced Formation of Artificial Protein Capsids*. Nano Letters. Copyright © (2012) American Chemical Society.

2.2. Materials and Methods

2.2.1. Purification of TRAP

Genes encoding TRAP from *G. stearothermophilus* were sequence-optimized for expression in *E. coli* (Genscript Corporation, NJ, USA) and cloned into ampicillin-resistant pET21b (Merk Millipore, MA, USA) at NdeI and BamHI restriction enzyme sites as reported previously [28]. Plasmid containing the gene for mutant was a kind gift of Ali Malay [30].

E. coli BL21 DE3 cells (Agilent Technologies, CA, USA) were transformed with cloned plasmid vectors (pET21b) encoding either TRAP-WT or TRAP-K35C. A single ampicillin (100 µg/ml or ~0.3 mM)-resistant colony (containing ampicillin-resistant plasmid pET21b) was picked from the LB-ampicillin agar plate with a sterilized tip. The single colony was incubated overnight at 37 ℃ in 100 ml LB medium containing ampicillin (100 µg/ml). This was transferred into 1-3 liters of LB medium containing ampicillin (100 µg/ml). Protein expression was induced by 0.4 mM isopropyl β-D-1-thiogalactopyranoside (IPTG) when the absorbance (OD_{600}) of the cell culture became 0.4-0.6, and further incubated for 3 h. The cell culture was centrifuged and the cell pellets were kept at -20 or -80 ℃ in a buffer containing 20 mM Tris-HCl pH8 (at room temperature: RT) and 2mM DTT ("Buffer A" in this chapter. DTT can be substituted with another reducing agent TCEP) until used.

Frozen cell pellets were resuspended in 40-50 ml of Buffer A, and lysed by sonication (power 8-10, duty 40, ~100 times using standard tip equipped with ultrasonic disruptor, UD-211, TOMY Digital Biology CO., LTD, Tokyo, Japan). The lysates were centrifuged at 40,000 *g* for 1 h at 4 °C. The supernatant fraction was heated at 80 °C for

10 min, cooled on ice, and centrifuged again at 40,000 *g* for 1 h at 4 °C. The supernatant was loaded on HiTRP QFF ion exchange column (2 x 5 ml) and eluted with 0-1 M NaCl gradient with an AKTA purifier (GE Healthcare Life Science). TRAP usually elutes in the early fractions. The purity of the fractions was checked with SDS-PAGE [13] (e-PAGEL 5-20%, ATTO Corporation) to select relatively pure TRAP protein fractions. The 10 kDa monomer band and the 80 kDa 11mer ring band are visible on the SDS-PAGE gel. The selected fractions were mixed and concentrated using Amicon Ultra 10 kDa MWCO centrifugal filter units (Merk Millipore). The concentrated sample was subjected to gel filtration chromatography with a HiLoad 16/60 Superdex 200 column in 20 mM Tris-HCl pH 8.0 and 0.15 M NaCl ("TRAP-cage Buffer") at 4 °C. Usually TRAP elutes at approximately 70-90 ml. TRAP proteins were usually pure at this stage, but if the purity was not sufficient, the selected fractions from gel chromatography were dialyzed into 20 mM Tris-HCl pH 8.0, and then the sample was loaded onto an affinity column, HiTrap Heparin HP, and eluted with a 0-1 M NaCl gradient. Protein concentrations were calculated using the BCA protein assay kit (Pierce Biotechnology) or calculated from the absorbance at 280 nm using an extinction coefficient of 8250 M^{-1} cm^{-1} (Coefficient calculated based on trp-liganded TRAP-K35C using PROTEIN CALCULATOR [14]). TRAP-WT was produced in a similar fashion but omitting the Hi TRAP Q FF column step and was a kind gift from Soshichiro Nagano, RIKEN Japan.

[13] ~1-10 µl of the samples were mixed with 2x loading dye, ~8M urea and β-mercaptoethanol, and incubated at 94 °C for 5 min and loaded on the SDS-PAGE gel

[14] http://protcalc.sourceforge.net/

2.2.2. Gold nanoparticles

I have used two types of 1.4 nm GNPs (Au_{55} core cluster). One is called Au1.4MS and the other is called Nanogold. Details are follows:

Au1.4MS: Negative charged GNPs

Au_{55} core cluster with monosulfonated triphenylphosphine ligands: $Au_{55}(Ph_2PC_6H_4SO_3Na)_{12}Cl_6$ (called "Au1.4MS") [75-77] was provided by Annika Leifert and Ulrich Simon, RWTH Aachen University, Germany.

Au1.4MS was derived from $Au_{55}(PPh_3)_{12}Cl_6$. Triphenylphosphine (PPh_3) was replaced by mono-sulfonated triphenylphosphine (3−(diphenylphosphino)benzenesulfonic acid sodium salt) via a two-phase ligand exchange reaction [78]. The structure of Au_{55} and the protecting ligands is shown in **Figure 2.3** and **Figure 2.4** [78-80]**.** Au1.4MS has a negative surface charge due to the terminal sulfonate groups, and Au1.4MS including its ligand shell is approx. 2.1 nm in diameter [40].

Nanogold: neutral GNPs

Similarly to Au1.4MS, this GNP is based on a Au55 core with a triphenylphosphine-based water soluble neutral ligand. This non-functionalized

Nanogold (“Nanogold” in this thesis) was purchased from Nanoprobes, Inc. (NY, USA). The exact outer ligand information for this particle is not available from the manufacturer.

Both Nanogold and Au1.4MS appeared to catalyze TRAP-cage structure formation. In this thesis, I used both Nanogold and Au1.4MS.

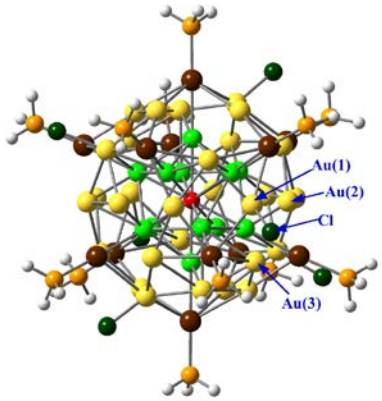

Figure 2.3 Computational model of $Au_{55}(PH_3)_{12}Cl_6$.
This computational model shows close-to-icosahedral geometry (distorted icosahedral geometry). For this model, PH_3 ligands were chosen instead of PPh_3 to reduce the computational cost for finding the optimum geometry of Au_{55} cluster with ligands. Central Au (red) is surrounded by a 12 Au shell (green), and a 42 Au shell, 12 vertices Au (brown) and 30 face centered Au (yellow). Cl is shown as dark green and each PH_3 is shown in orange and white. Reprinted with permission from (Figure S1 of ref. [79]). Copyright (2009) American Chemical Society.

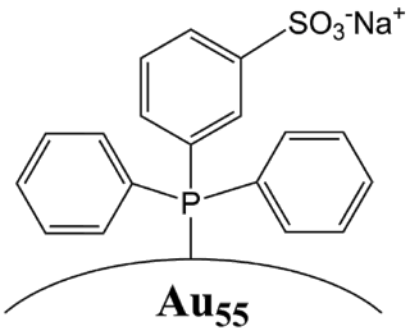

Figure 2.4 Monosulfonated triphenylphosphine ligands on Au_{55}
See the text for the detail of this ligand.

2.2.3. TRAP-cage formation

In order to form TRAP-cage, GNPs are necessary. However, the presence of GNPs may cause problems for downstream experiments and applications. For example, strong absorbance of GNPs in the UV region interferes with biological analysis such as concentration measurements. 1.4 nm GNPs may also have bio-toxicity [80, 81], a potential drawback for applications as a drug carrier. Therefore, the Heddle lab has been investigating alternative, GNP-free methods of TRAP-cage formation. Recently, TRAP-cage has been made without GNPs; however, the reaction has poor yield and it is not very reproducible. Therefore, I have carried out most of my experiments with TRAP-cage formed in the presence of GNPs. TRAP-cage is approximately 20 nm in diameter. When the concentration of GNPs became higher (equal to approx. two times TRAP monomer protein concentration and higher), a smaller (~15 nm) TRAP-cage was formed dominantly with Nanogold [30].

TRAP-cage made with GNPs: To 0.26 mg/ml (32 µM) of purified TRAP-K35C, 12 to 60 µM of 1.4 nm GNPs was added and incubated for at least 1 h at RT in a buffer containing 20 mM Tris-HCl, pH 8 and 0.15 M NaCl (TRAP-cage buffer). NaCl was sometimes omitted in order to slow TRAP-cage's motion during HS-AFM observation.

TRAP-cage made without GNPs (not reproducible): K35C-TRAP was oxidized in air at room temperature by allowing to stand in TRAP-cage buffer for several days, and then denatured in 2-8 M urea. After the removal of urea, TRAP-cage was formed.

2.2.4. HS-AFM observation

All the images in this thesis were taken using a HS-AFM instrument constructed by the Ando group at Kanazawa University, Japan [36, 82]. Diluted protein samples

(typically in a range of 0.3 to 127 μM TRAP subunits) were loaded onto freshly cleaved mica, incubated there for 2 to 5 min and washed with the buffer used in TRAP-cage formation. For TRAP-WT, NaCl was omitted from the observation buffer in order to slow its motion. HS-AFM imaging was undertaken as in previous reports [37, 83]. Briefly, a small cantilever tip, BL-AC10DS or BL-AC7DS-KU2 (Olympus, Tokyo), was sharpened individually by electron-beam deposition and plasma etching. Images were taken with oscillation amplitude typically between 2 to 6 nm (peak to peak) after the AFM tip approached the sample. Imaging rate, scan size, and parameters of feedback control were continuously optimized to enable the clearest possible visualization with the minimum tip force reaching the sample. In case of *in situ* addition of gold nanoparticles, DTT, or HCl, in order to prevent damage to the scanner, the sample surface was momentarily released from the AFM tip and a minimal amount of liquid was added (1-2 μl). To reduce the risk of scanner breakage, the area around the z piezo actuator and sample stage was coated with a water resistant Fluoride (FluoroSurf, FluoroTechnology Co., Ltd., Aichi, Japan).

2.2.5. HS-AFM image processing and analysis

IGOR Pro (WaveMetrics)-based software for HS-AFM, developed by the Ando Group at Kanazawa University was used to process the image, using features such as Gaussian/averaging filtering, FFT frequency filtering, automatic flattening and drift compensation of images. Further individual image refinement (flattening and adjusting color scale) and 3D reconstruction, measurement of height line profiles, measurement of distances (differences in x, y and z values between two points), frame averaging, marking the center of the TRAP cavity from processed images and superimposing the marks onto the original images, and calculating the height of TRAP-cages (determining height

maxima in individual cages and normalizing against background height information) were performed using the Gwyddion SPM Data Visualization and Analysis Tool [84]. Extraction of maximum values from the height line profiles and histogram construction were carried out using MATLAB (MathWorks, Inc.). The time counter in the images is based on the real time. So, when there is a gap between observation (typically within 10 s), the time counters were running for this interval. For example, in **Figure 2.10**, page 59, the running time of 585 s includes 30 s (in total) of gap between observations.

2.2.6. Analytical ultracentrifugation (AUC)

In order to identify the molecular weight of TRAP-cage, analytical ultracentrifugation was conducted, with the kind help of Prof. Fumio Arisaka, Tokyo Institute of Technology. TRAP-cage was purified with a sucrose density gradient (5% increments gradient of 20% to 45%), at 40,000 rpm for 2 h. The optical density of the protein sample was adjusted to be 0.5 to 1 prior to the sedimentation velocity experiments. AUC was performed using Beckman-Coulter Optima XL-1. The centrifugation speed was 40,000 rpm at 20℃. The data was fitted and analyzed with SEDFIT (National Institutes of Health, USA) software. The AUC experiment and SEDFIT analysis was kindly done by Prof. Fumio Arisaka.

2.3. Results

Of particular interest in this research are i) the conformational changes that the TRAP rings undergo with the addition of GNPs, ii) the higher resolution structure of the cage, and iii) the role of GNPs in TRAP-cage assembly. In this thesis, I address all of these questions with HS-AFM.

2.3.1. WT versus K35C

The crystal structure of the TRAP-WT oligomer shows that it resembles a conical cylinder with a central cavity [13]; the "top" surface having an outer diameter of 8.5 nm, the "bottom" surface 7 nm, a height of around 3.5 nm, and a central cavity measuring 1.5-2 nm across (**Figure 2.5 A)**. AFM results showed that both TRAP-WT and TRAP-K35C appeared identical (**Figure 2.5 B and C**), with a diameter of 11 nm and a height of 4-6 nm. This HS-AFM image is consistent with the structure obtained from X-ray crystallography, considering the effects associated with HS-AFM imaging, such as motion of the TRAP protein, the radius of the HS-AFM tip and the parachuting effect (

Figure 2.6).

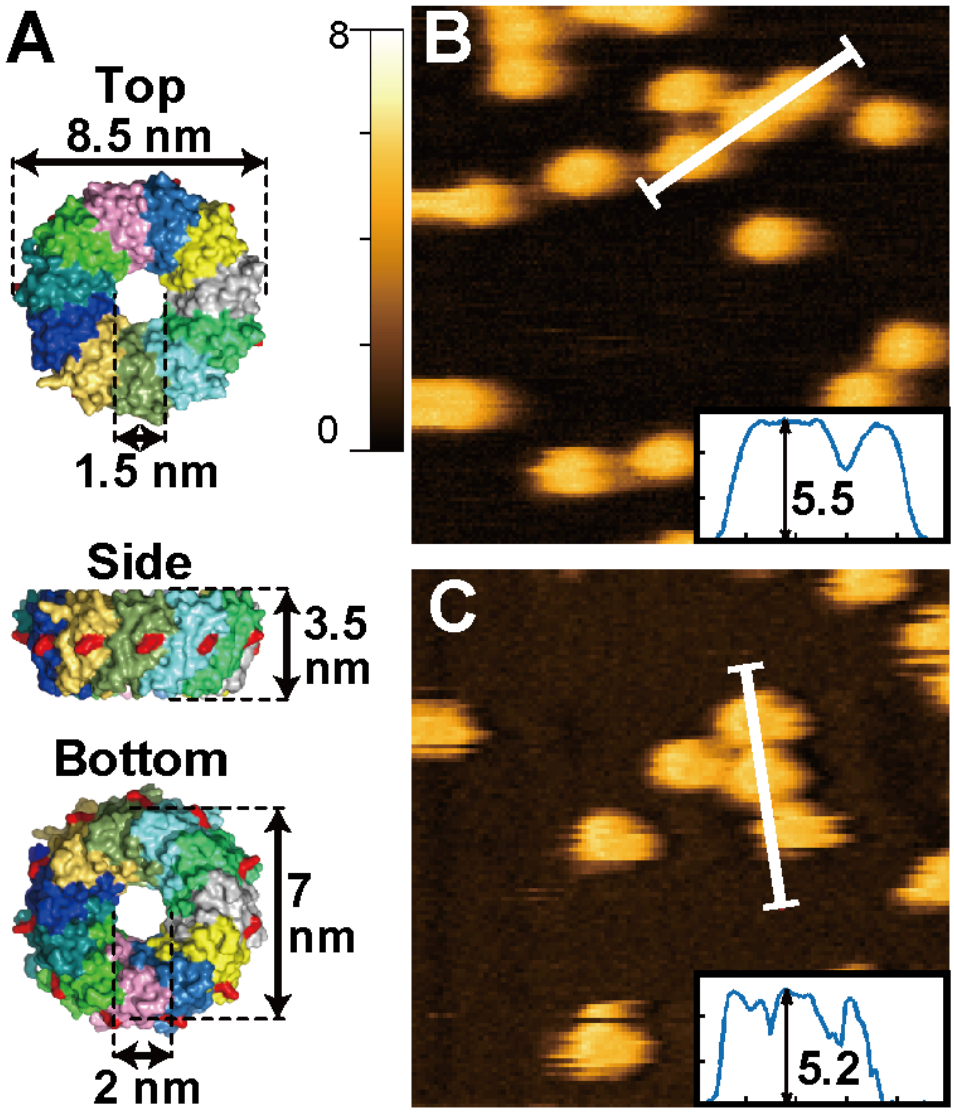

Figure 2.5. TRAP ring structure.[15]
(A) Crystal structure of TRAP (PDB 1UTV) [13]. All images are shown as surface views, with each of the 11 monomers shown in a different color. The position of the mutagenized residue Lys35 is shown in red. The dimensions of the protein were measured by referencing the distance between atoms calculated from PyMOL [85]. **(B)** and **(C)** HS-AFM images of **(B)** TRAP-WT and **(C)** TRAP-K35C, showing a 100 nm x 100 nm area. The white lines show the path of the line height profiles which are shown in the insets (50 nm x 6 nm) of each panel with the height of the highest peak (in nm) marked.

[15]Reprinted with permission from (Figure 1 of Imamura, *et al*., *NanoLett*.). Copyright (2015) American Chemical Society

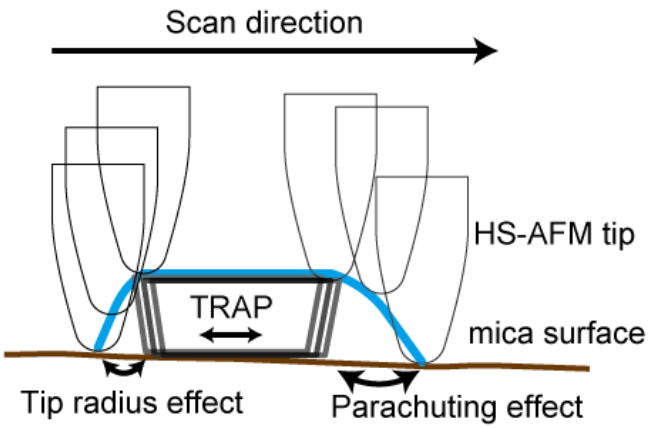

Figure 2.6. Various effects in HS-AFM imaging
When the AFM tip scans along TRAP protein, the HS-AFM image shown by the blue line is obtained. Due to the motion of protein, tip radius effect, parachuting effect, the tilt of mica surface and mechanical noise, the obtained image varies from the real structure of the object [37].

2.3.2. TRAP movement on the mica surface

Both TRAP-WT and TRAP-K35C moved randomly and individually on the mica surface. Compared to TRAP-K35C, TRAP-WT moved too fast to track the behavior in the same TRAP-cage Buffer. Therefore, I focused on analysis of TRAP-K35C movement.

TRAP-K35C moved incrementally in each HS-AFM frame, and intermittent large displacement was observed (**Figure 2.7**). This could be because the binding of the TRAP ring to the mica surface is electrostatic and is not strong enough to retain the TRAP ring for a prolonged period of time at 150 mM NaCl.

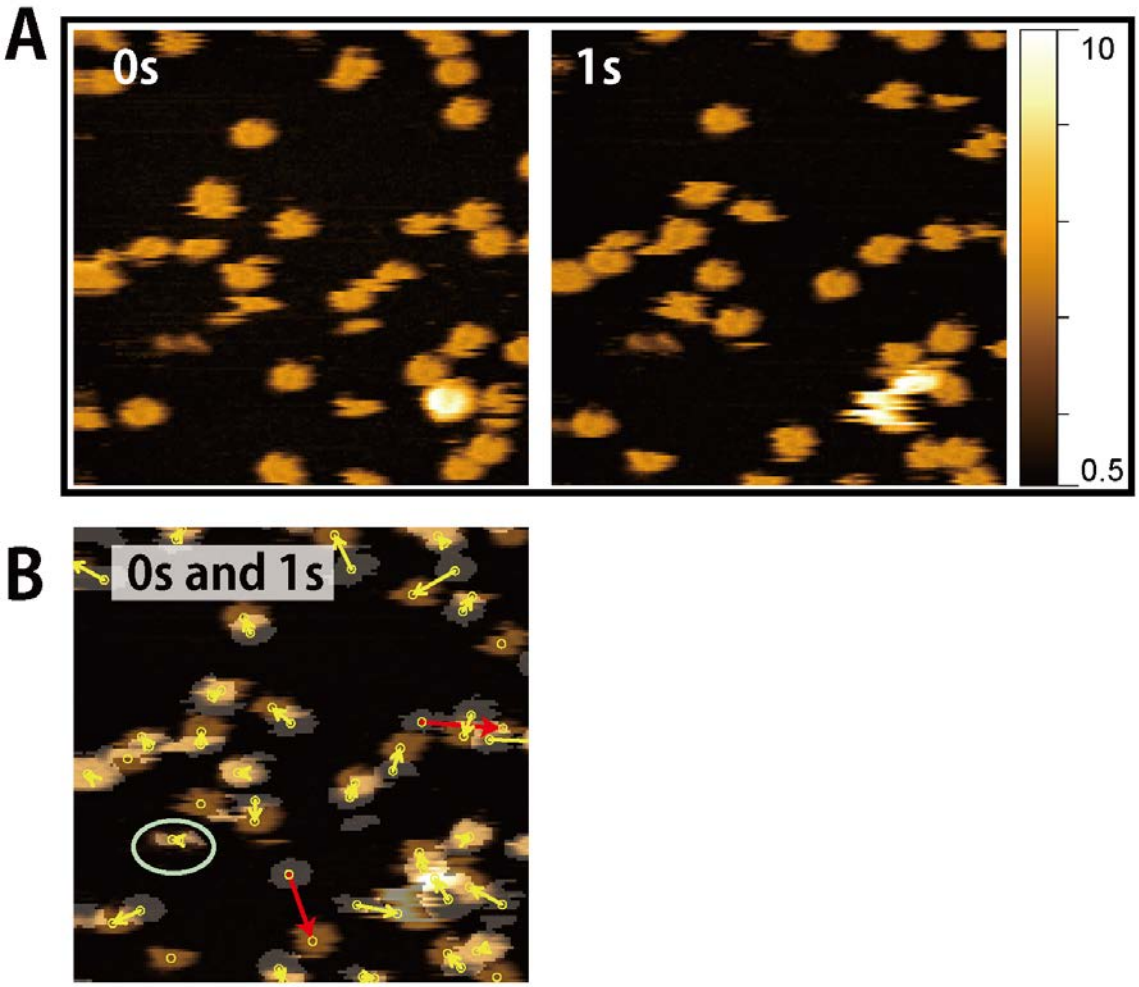

Figure 2.7. Movement of TRAP-K35C during one second.
(A) The same TRAP-K35C sample at different times (0 s and 1s)

(B) Superimposed images of (**A**)**.** The binary image of 0s was superimposed on the image of 1 s**.** Each TRAP movement is shown as yellow arrows. Long displacements are indicated by red arrows. The circled particle (possibly not a TRAP ring) did not move during 15 s of observation.

Images were taken at 1 frame per second (fps) over an area of 150 nm x150 nm. Image was flattened and the height scale range was adjusted from 0.5 to 10 nm.

2.3.3. Tracking analysis of TRAP-K35C

46 TRAP-K35C proteins were tracked over 16 seconds (397 movement as a total). Each K35C-TRAP's movement was tracked manually, their center points were also marked manually, and the XY coordinates were extracted usng ImageJ software. In Brownian motion, the mean squared displacement (MSD) $< d^2(\mathrm{r}) >$ is known to have a linear dependence on time (t). In two-dimensional diffusion, MSD follows

$$< x^2(\mathrm{r}) > \approx 4Dt \qquad \textbf{(5)}$$

where *D* is the diffusion coefficient. Based on this equation, the diffusion coefficient can be estimated from the MSD. From the particle tracking analysis of TRAP-K35C, the diffusion coefficient was estimated as 22 [nm^2/s] as shown in **in HS-AFM is usually small. If the area of the observation** was wider, longer step distance could have been observed more frequently.

Figure 2.8

The theoretical diffusion coefficient was also calculated from the Stokes-Einstein equation. Since TRAP is a ring and not a sphere, I assumed that it was closer to oblate ellipsoid. The Stokes-Einstein equation for oblate ellipsoid can be expressed according to the following equation [86].

$$D = \frac{kT}{6\pi\eta(\alpha^2\beta)^{1/3}}[nm^2/s] \qquad \textbf{(6)}$$

Where, k is Boltzmann constant (1.38×10^{-23} [JK^{-1}] or 1.38×10^{-20} [$gm^2s^{-2}K^{-1}$]), T is absolute temperature (298 [K]), α and β are the radii of the long and short axes of oblate ellipsoid, respectively (4 nm and 2 nm each), and η is viscosity of water (0.891 $gm^{-1}s^{-1}$).

From this equation, theoretical diffusion coefficient was calculated as 7.7 x 10^7 [nm^2/s], which is much larger than that estimated from the HS-AFM observation. This result supports the suggestion of an interaction between the protein and the mica surface. The histogram of the distance of each step against probability was close to a Lévy flight distribution, which is a type of random walk model with a "heavy tail" (probability of long step distance is higher than Brownian motion). Lévy flight can be expressed according to the following equation [87] [16].

$$\mathrm{p}(r) \propto |r|^{-\alpha} \qquad 1 < \alpha < 3 \qquad \textbf{(7)}$$

From the HS-AFM observation, it is difficult to observe large movements because the area observed in HS-AFM is usually small. If the area of the observation was wider, longer step distance could have been observed more frequently.

[16] Introduction to the theory of Lévy flights by A.V Chechkin, R. Metzler, J. Klafter, and V.Yu. Gonchar (found online)

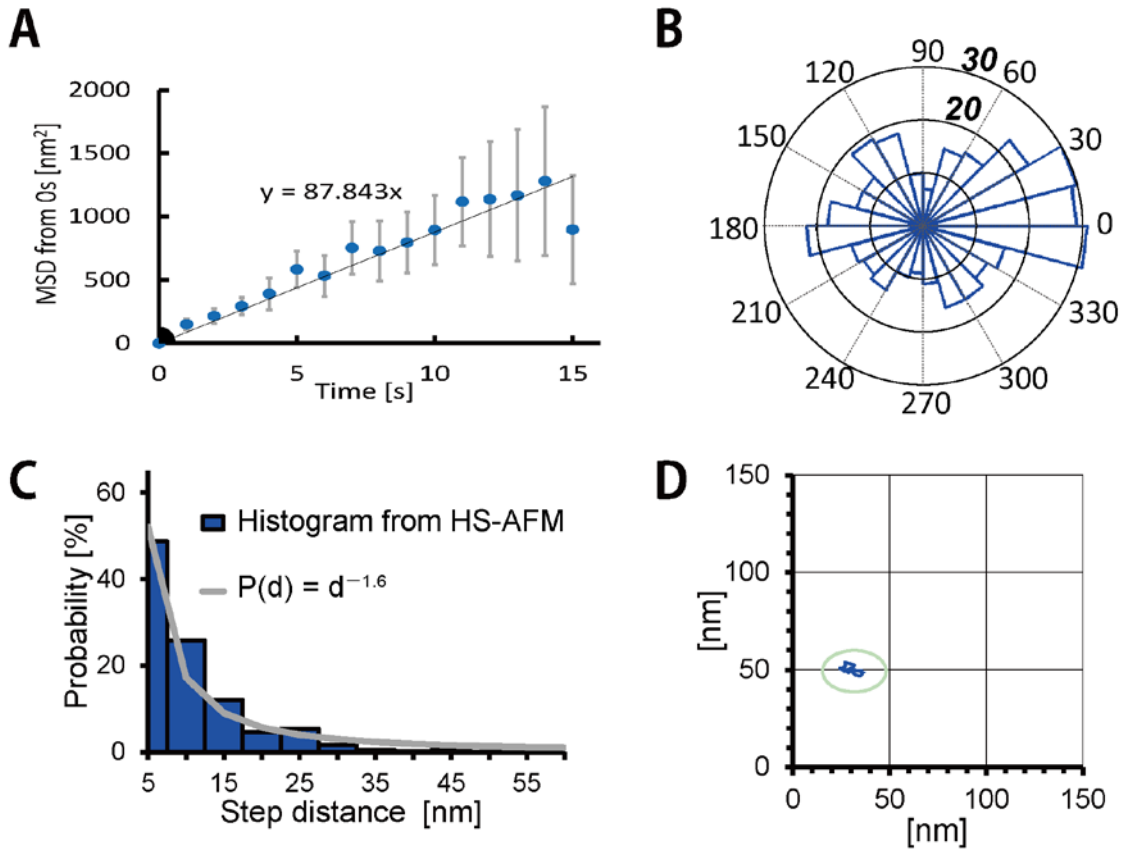

Figure 2.8. Random movement of TRAP-K35C on mica

(A) Mean squared displacement (MSD) from 0 s (y axis) against time (x axis). The error bar shows the standard error.

(B) Histogram of directions of movement.

(C) The histogram of the distance of each step and theoretical Lévy curve based on Lévy distribution.

(D) One particle, circled in **Figure 2.7 B**, did not move on the surface of mica. Therefore, this particle is a useful indicator of the drift effect in AFM image analysis. This graph shows a 15 s (16 fames) tracking of the particles. x and y axes correspond to those of the AFM image in **Figure 2.7**.

2.3.4. TRAP-K35C and GNPs

Next, Nanogold or Au1.4MS (see **Chapter 2.2.2** for details) was added to TRAP-K35C to understand the intermediate structure in the TRAP-cage assembly process.

Nanogold

Nanogold was added at 0 s to the final concentration of 3.75 µM and further added at 249 s to the final concentration of 7.5 µM (**Figure 2.9**). For more than 100 s, little structural change of TRAP-K35C was observed. However, the motion of TRAP-K35C became gradually slower. This slower motion after addition of GNPs could be due to stronger interactions between TRAP-K35C and mica mediated by Nanogold and/or to the formation of larger structures (larger particles should move more slowly on the mica surface). This slower motion can be judged by the outline and the central cavity of TRAP-K35C becoming more well-defined (**A - E**). The image became noisier after (**F**), due to the consumption of the tip and accumulation of some dust.

Since TRAP-K35C tends to bind to mica surface more strongly with the addition of GNPs, formation of three-dimensional TRAP-cage spherical structure is disfavored. Therefore, in this observation (**Figure 2.9**) (and only in this observation among all the HS-AFM imaging), TRAP-K35C was added in solution (< 0.1 nM) prior to the addition of GNPs. This caused the increase in occupancy of TRAP-K35C on the mica surface over time.

Interestingly, when the mica surface was fully covered with protein, a second layer of protein, which is not in contact with the mica surface, forms (see images after (**D**)) and TRAP-K35C gradually formed aggregated structures (**H - J**). However, this aggregation structure did not form the 20 nm diameter TRAP-cage structure. As shown

in the line profile in (**J**), even rare large aggregates were only approximately 10 nm in height.

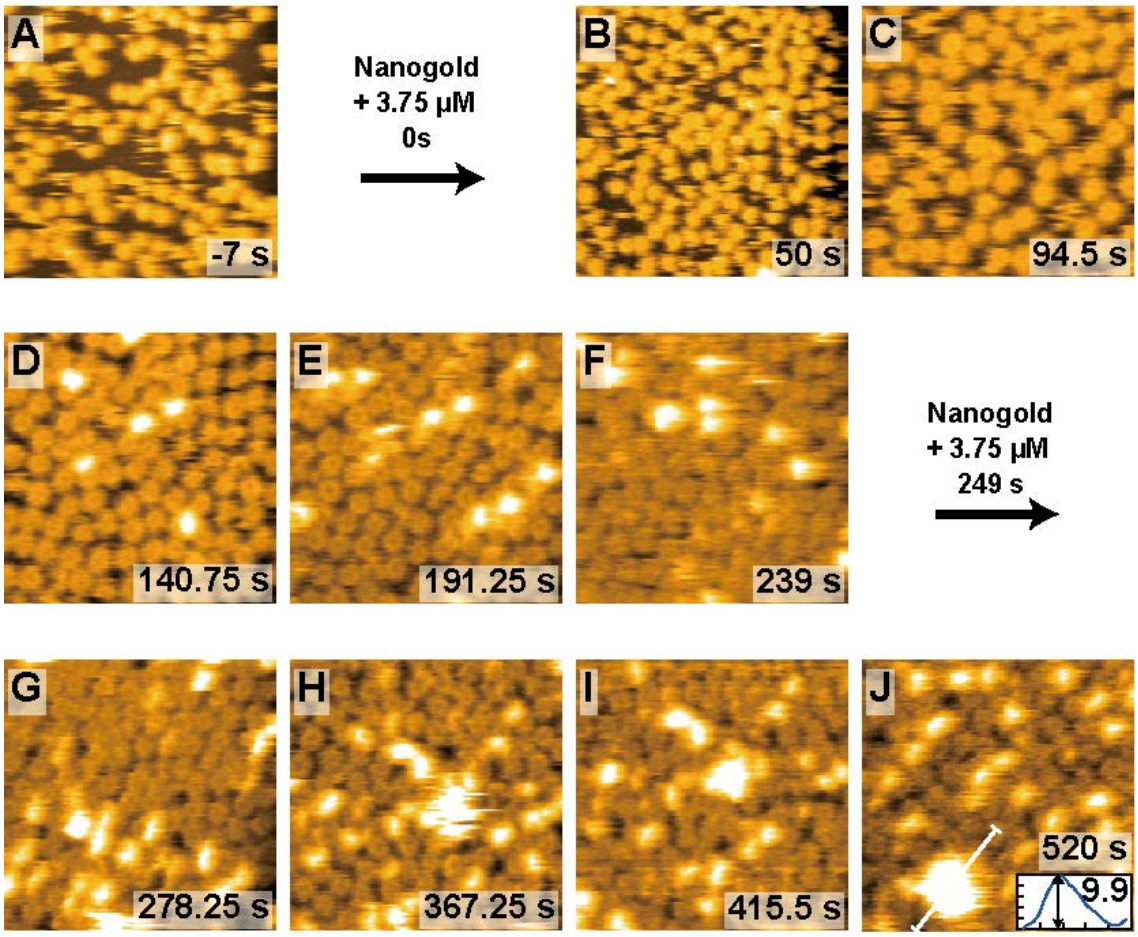

Figure 2.9. TRAP-K35C and Nanogold
(**A**) Before addition of Nanogold. (**B** - **J**) After the addition of Nanogold. Nanogold was added to the final concentration of 3.75 µM at 0 s and further added to the final concentration of 7.5 µM at 249 s. HS-AFM images are 150 nm x 150 nm for (**A)** and (**B**); 100 nm x 100 nm for (**C** - **J**) in size. Height color scale was set to a total range of 7 nm for all images. White line in (**J**) is the path of the line height profiles, which are shown in the insets (50 nm x 10 nm) with the height of the highest peak (in nm) marked.

Au1.4MS

Addition of 1.4 μM Au1.4MS to TRAP-K35C on the mica surface led to a rapid increase in the height of the observed structures, which corresponds to the binding of Au1.4MS to the central cavity of the protein (**Figure 2.10 A**). Compared to Nanogold, Au1.4MS interacted more strongly with TRAP-K35C especially at the protein cavity, and also caused substantial aggregation. In the protein aggregates, the outline and central cavity of individual ring structure was not discernible, which was different from those observed after the addition of Nanogold. The aggregated structure initially underwent frequent structural changes via shuffling of protein subunits (or rings), but appeared to gradually become more rigid. After ~150 s, free TRAP or its subunits had almost completely gone, and the aggregated structure showed less frequent structural changes.

Although Au1.4MS bound to the protein was recognizable, free Au1.4MS was not visible, possibly due to no interaction with mica or to the limited spatial and temporal resolution of HS-AFM.

Addition of DTT to the Aggregation

Hypothesizing that the aggregation was formed via disulfide bonds between cysteines of TRAP-K35C, the effect of a reducing agent, dithiothreitol (DTT), was tested. The addition of 1.4 mM DTT gradually reversed the aggregation such that discrete TRAP rings again became visible (**Figure 2.10 B**). Also, Au1.4MS was no longer visible on the protein surface after DTT treatment as evidenced by the fact that the height profile became almost the same as for the original TRAP-K35C (Compare **A-i** and **B-iv**). In **B-iv,** some aggregates remained, but eventually almost all aggregates returned to a non-aggregated form (**B-vii** and **viii**). Further addition of 1.4mM DTT 100 s later did not speed up the disaggregation process, and aggregation processes were still observed (**iv**-**vi**),

suggesting some form of competitive process, which is not surprising given the simultaneous presence of both DTT and GNPs.

Initial quick disaggregation and later slow disaggregation by DTT could be different processes. In the initial quick disaggregation process, Au1.4MS may also be involved in addition to disulfide bond breakage. Since the Au1.4MS disappeared from the aggregated structure and its height was reverted back to that of original TRAP-K35C.

Compared to the previous report

The binding of GNPs onto TRAP-cage is in contrast to the previous report showing that GNPs (Nanogold) were not found in the TRAP-cage structure [30]. The reason for the difference between previous report and this study could be due to the different outer ligand of GNPs and/or the reaction conditions. In the previous report, the TRAP-cage was formed in solution and Nanogold (neutral charge) was used. In this study, Au1.4MS (negative charge) was used, and TRAP-cage was not formed probably because of interactions between TRAP-K35C and the mica surface.

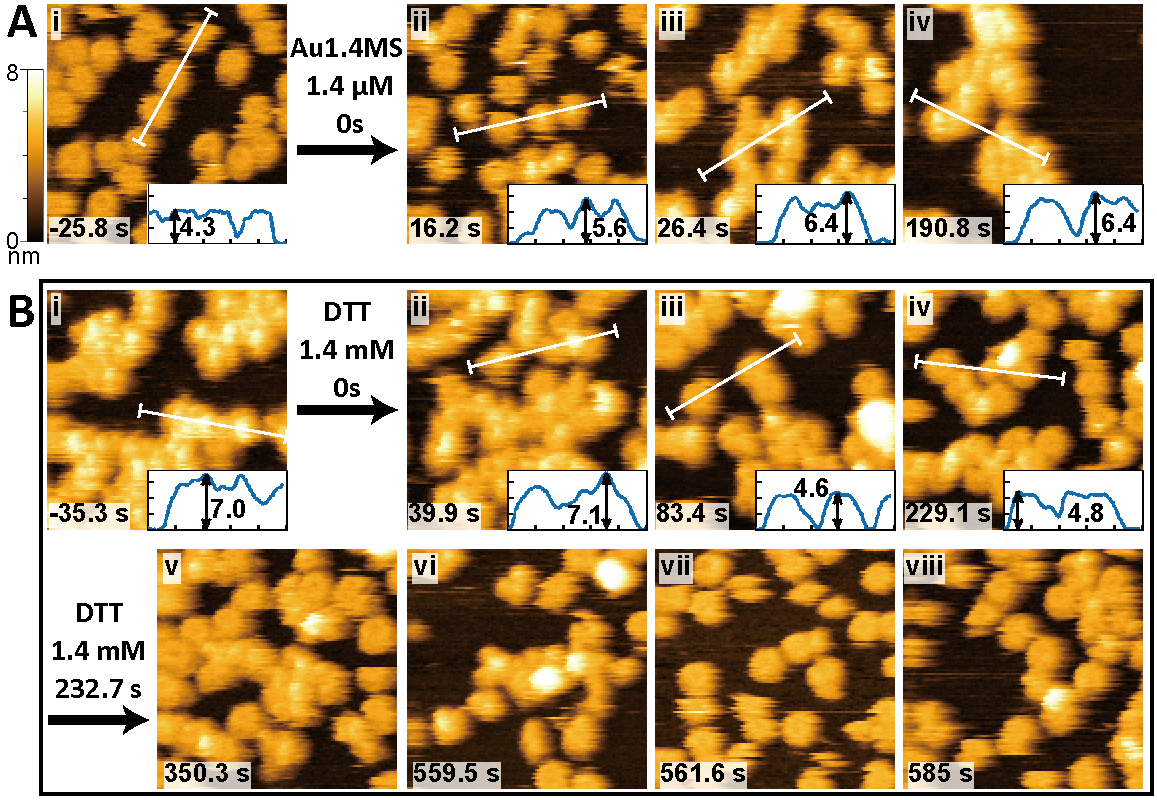

Figure 2.10. Dynamic effects of Au1.4MS and DTT on TRAP-K35C. [17]
All HS-AFM images are of areas 80 nm x 80 nm in size. **(A)** Addition of Au1.4MS to TRAP-K35C: (**i**) TRAP-K35C before addition of Au1.4MS. (**ii-iv**) show the same location after the addition of 1.4 µM Au1.4MS. **(B)** Addition of DTT to the same sample as in **(A)**, at a different location on the mica surface: (**i**) 421.7 s after initial Au1.4MS addition (35.3 s before addition of DTT); (**ii**)-(**vi**) show the same location after the addition of 1.4 mM DTT. (**v-viii**) show after addition of another 1.4 mM DTT at 232.7 s. (**v**) and (**vi**) are the same location as (**iv**). Observation location was moved in (**vii**) and in (**viii**). White lines are the paths of line height profiles which are shown in the insets (50 nm x 7.5 nm) of each panel with the height of the highest peak (in nm) marked.

[17] Adapted with permission from (Figure 2 of Imamura, *et al.*, *NanoLett.*). Copyright (2015) American Chemical Society

Protein Shuffling

Notably, in the both aggregation process and disaggregation process via the addition of Au1.4MS and DTT, TRAP-K35C frequently changed its structure which appeared to be due to subunit shuffling between and within the rings as shown in **Figure 2.11**. This suggests that TRAP-K35C was rearranged into an irregular shape by the addition of Au1.4MS, then subsequently formed TRAP-cage as a regular structure. This flexible protein shuffling is possibly a key to finding the lowest energy TRAP-cage structure. There are 11 identical cysteines around the TRAP-K35C ring. If the TRAP-K35C was a rigid structure, it would perhaps not allow TRAP-K35C sufficient flexibility to form such a regular sphere-like structure.

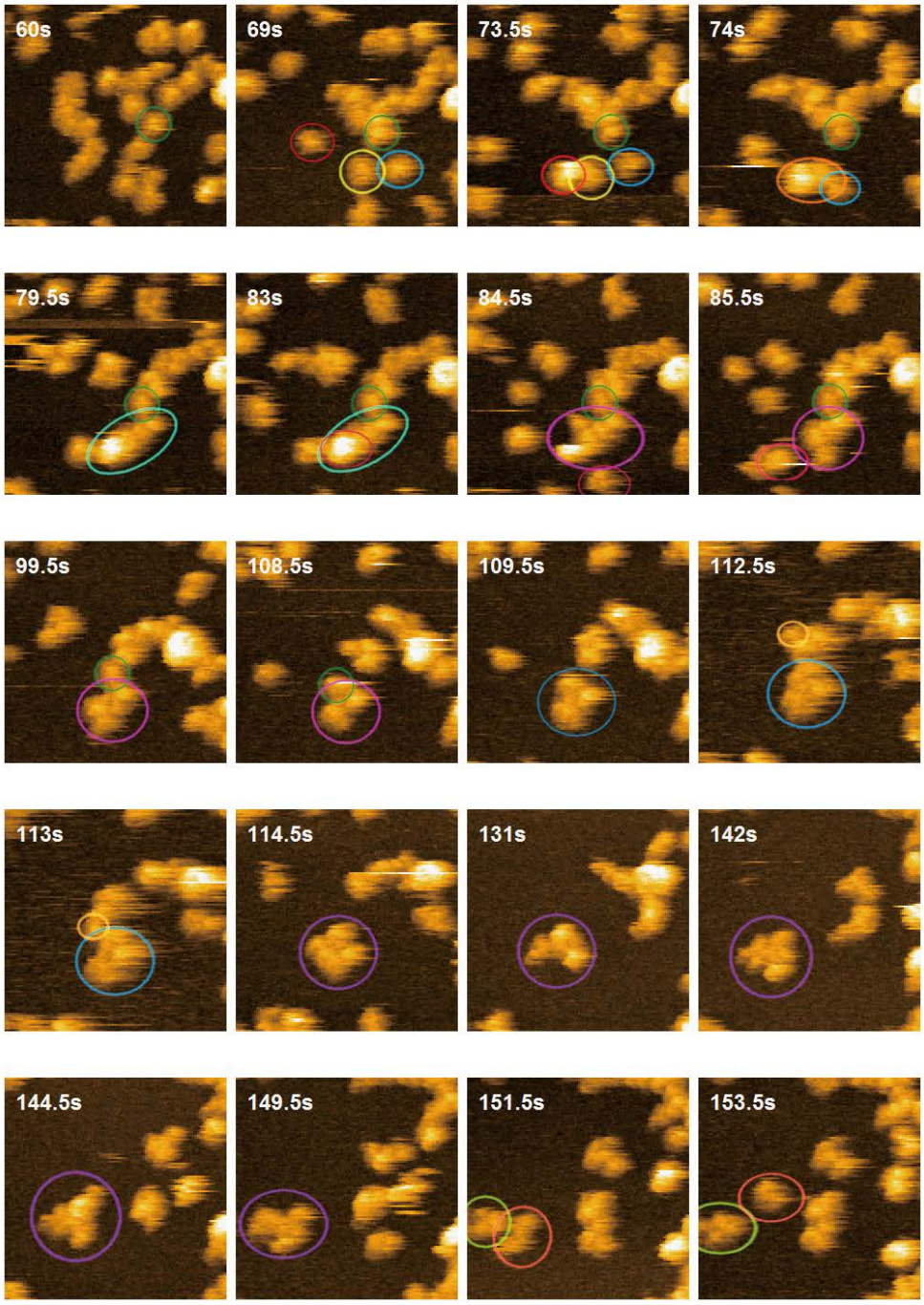

Figure 2.11. Protein shuffling following addition of Au1.4MS [18]
All HS-AFM images are of areas 80 nm x 80 nm in size. 1.4 µl of Au1.4MS was added at 0 s. The circles are one or several TRAP-K35Cs. When they combined or split, the circle's color is changed. The scale bar is 20 nm.

[18] Adapted with permission from (Movie S4 of Imamura, *et al*., *NanoLett*.). Copyright (2015) American Chemical Society

2.3.5. WT-TRAP with GNPs

As a control experiment, wild type (TRAP-WT) was reacted with GNPs. No aggregation was observed but the protein was still able to capture GNPs in the central cavity of the ring (**Figure 2.12**). Compared to the fast binding of Au1.4MS on the TRAP-K35C mutant, binding of Au1.4MS in the central cavity on TRAP-WT was slow and not as efficient (**B**). Nanogold was also slowly bound to the TRAP-WT, but it was even slower than Au1.4MS binding on TRAP-WT as there are still empty TRAP-WT at 400 s (**F**). TRAP-WT were also observed after incubating (20 hours) with GNPs in a test tube, to confirm that TRAP-WT does not form any higher-order structures. Interestingly, from this pre-incubated sample, GNPs accumulated in the central cavity of TRAP-WT (**G**-**J**). Compared to the homogeneous binding of Nanogold (**I**, **J**), some aggregation was also seen with the incubation of Au1.4MS (**G**, **H**). In both cases, TRAP-cage or any higher ordered structures were not observed.

The binding of GNPs in the central cavity of TRAP-WT rings, which was also observed in TRAP-K35C, may be due to size/charge matching and is likely not relevant to the aggregation or cage formation mechanism.

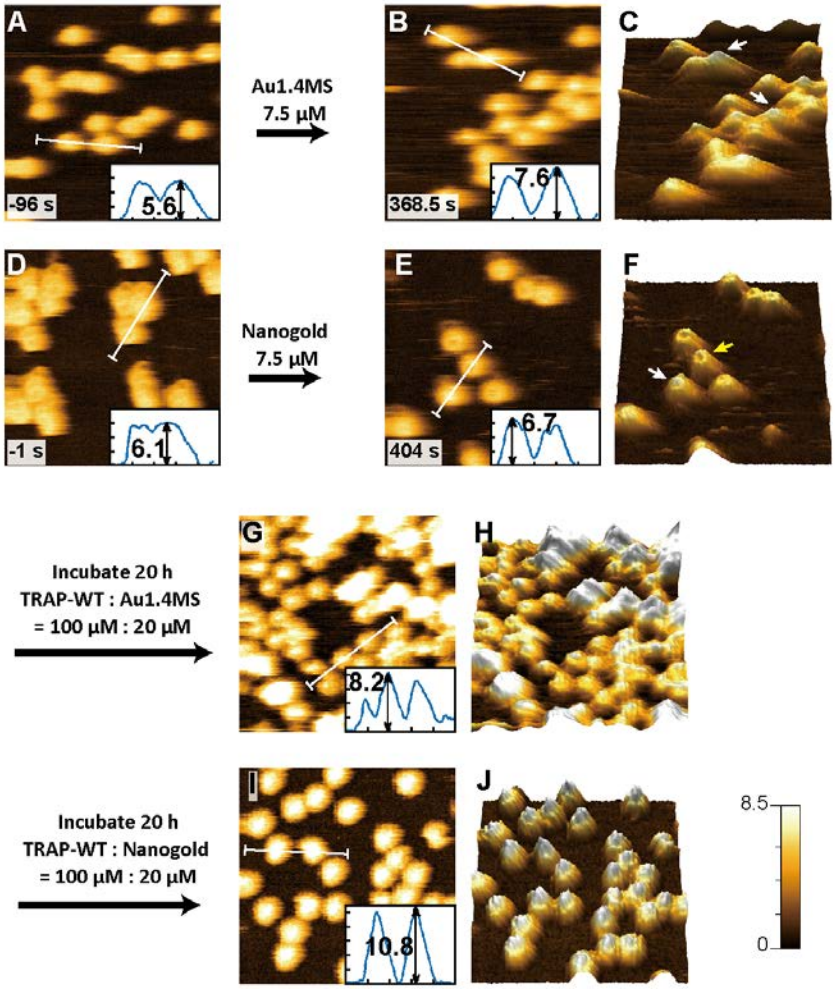

Figure 2.12. No structural change of TRAP-WT with Au1.4MS and Nanogold[19]
HS-AFM continuous images of TRAP-WT before (**A**), and 368.5 s after the addition of 7.5 µM Au1.4MS (**B**); before (**D**), and at 404 s after the addition of 7.5 µM Nanogold (**E**). HS-AFM images after 20 h incubation of TRAP-WT in test tube with Au1.4MS (**G**) and Nanogold (**I**). (**C**), (**F**), (**H**) and (**J**) are 3D reconstruction images of (**B**), (**E**), (**G**) and (**I**) respectively. The white arrows in (**C**) and (**F**) indicate TRAP-WT captured Au1.4MS and Nanogold, and the yellow arrow in (**F**) indicates empty TRAP-WT.

White lines represent the path of the height profiles that are shown in the insets: 50 nm x 8 nm in (**A**), (**B**), (**D**) and (**E**); 50 nm x 9 nm in (**G**); 50 nm x 11 nm in (**I**).

Observations were done under 20 mM Tris-HCl, pH 8, without NaCl. Observed area was 100 nm x 100 nm for all images. Color scale for the all the AFM images are shown on the bottom right.

[19] Adapted with permission from (Figure S1 of Imamura, *et al*., *NanoLett*.). Copyright (2015) American Chemical Society

2.3.6. Comparison of TRAP-cages made with Au1.4MS and Nanogold

TRAP-K35C was incubated with GNPs in the test tube to form TRAP-cage structures. The TRAP-cage structures were overall monodisperse, “spherical” structures as previously reported [30]. The average size was measured from the highest point of the each TRAP-cage, since the measured horizontal (x, y) dimensions were larger than actual size because of the previously mentioned effect in **Figure 2.6**. The typical HS-AFM images and their histograms of TRAP-cage made with Au1.4MS (**A**) and (**B**) and Nanogold (**C**) and (**D**) were shown in **Figure 2.13**.

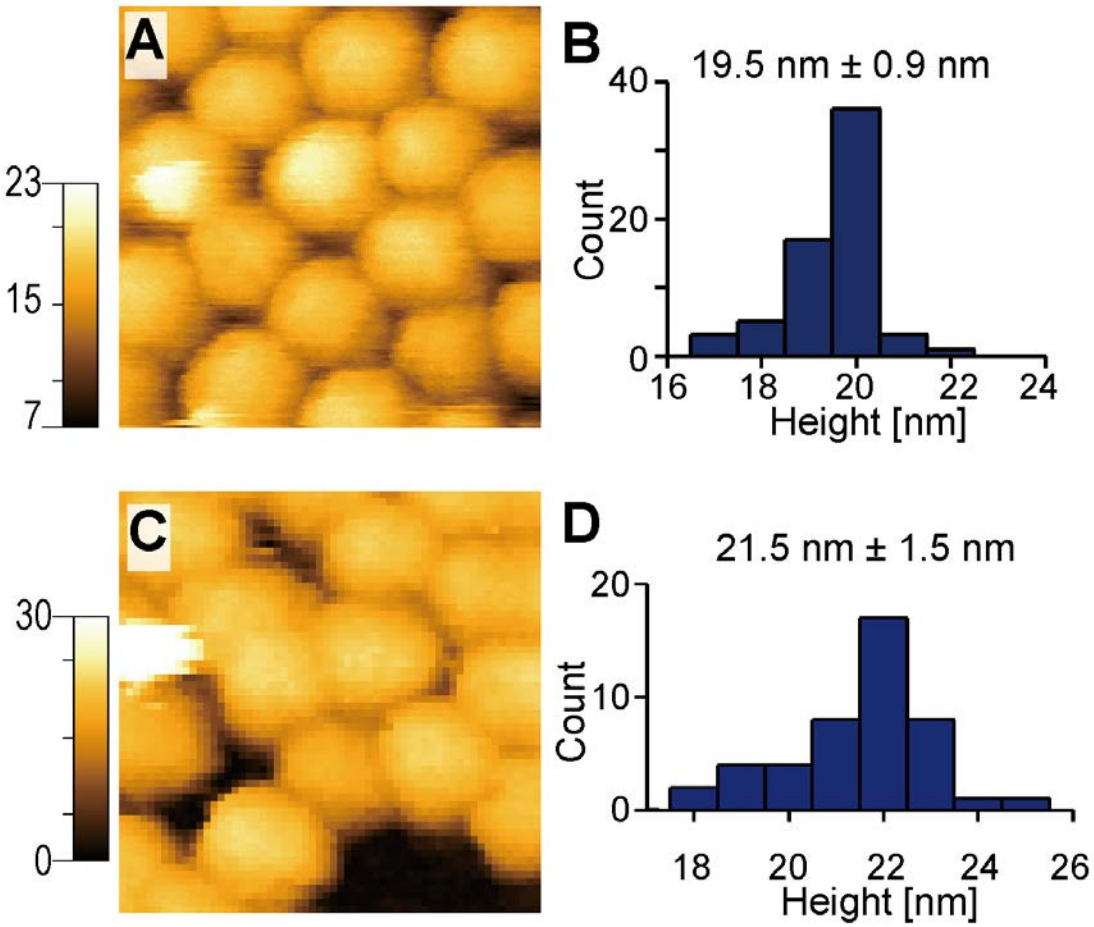

Figure 2.13. TRAP-cage made with Au1.4MS and Nanogold, and histogram of height.[20]

(A) TRAP-cage made with Au1.4MS with an average height of 19.5 nm ± 0.9 (SD) from 65 measurements (**B**). (**C**) TRAP-cage made with Nanogold with an average height of 21.5 nm ± 1.5 (SD) from 49 measurements (**D**). Both images are 100 nm x 100 nm.

[20] Adapted with permission from (Figure 3A of Imamura, *et al*., *NanoLett.*). Copyright (2015) American Chemical Society

2.3.7. Detailed TRAP-cage structure achieved with image processing

While some of the images of TRAP-cage appear to show some regular texture, (noticeable when viewing the images as a fast frame movie), there are limitations to what can be observed. This is because the height information of the image is expressed as a color table. In real life, light sources and shadows make it easier to recognize subtle 3D texture. To construct a 3D image including shadows is possible, but to do so for each of the thousands of images within the HRTEM movies was not practicable. Therefore, I used a high pass frequency filter of a fast Fourier transform (HP-FFT) and a Gauss/Average filter. The high pass filter removes (flattens) the large structural information (at the level of the spherical structure of the TRAP-cage), which makes it easier to see the texture on the TRAP-cage. Gauss/Average filtering removes the mechanical noise (the Gauss filter has a stronger effect than an Average filter).

By selecting optimum image processing condition with optimum contrast, ring structures in the TRAP-cage could be clearly identified (**Figure 2.14**). These images allow me to see for the first time that the building block of the cage was TRAP rings themselves rather than smaller protein subunits or other distorted or incomplete structures.

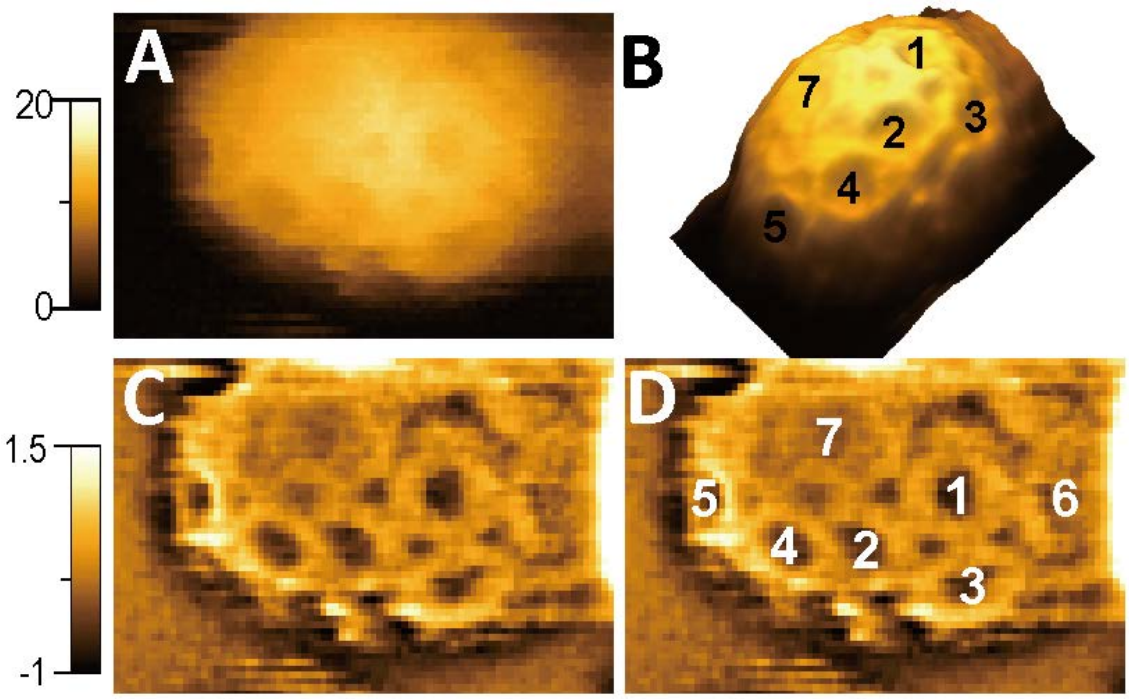

Figure 2.14. Detailed TRAP-cage structure revealed with image processing[21]
Detailed analysis of a single TRAP-cage structure: (**A**) unprocessed HS-AFM image; (**B**) 3D reconstruction image of Gauss filtered (3 x 3 pixel) image of (**A**) with identifiable rings numbered; (**C**) same image as (**A**) after the application of Gauss filter (3 x 3 pixel) and high pass FFT (HP-FFT) frequency filter (10nm); (**D**) same image as (**C**) with a number assigned to each identifiable TRAP ring. The images all measure 40 nm x 25 nm. Color scales on the left indicate the color mapping of the height information of HS-AFM images in nm.

[21] Reprinted with permission from (Figure 3B of Imamura, *et al*., *NanoLett*.). Copyright (2015) American Chemical Society

2.3.8. Estimation of the diameter of rings on the TRAP-cage

To rule out the possibility that the ring structures observed in the cage were different from the original TRAP ring structures, their diameters were estimated from the distance between the central cavities of adjacent rings (**Figure 2.15**, Page 70). The reason for this indirect measurement was because the location of the holes were easier to distinguish than the location of the edges of rings.

From the processed AFM image **(A)**, the *xy* coordinates of the holes (the center of the rings) were marked and converted into a binary image which was then superimposed onto the unprocessed HS-AFM image **(B)**. Using these coordinates the distances between adjacent central holes were measured (shown as white line segments). The linear distance between adjacent holes (*H*), as shown in **(C)**, was calculated from coordinates of the central holes in 3D space (Δx, Δy and Δz), which had to be adjusted for deviations in the *x* and *y* directions. The observed Δx and Δy values are usually greater than the actual distances due to the various effect explained in **Figure 2.6**, page 50. Therefore, Δx and Δy were adjusted by assuming the TRAP-cage structures to be perfectly spherical as shown in the following equations.

$$\Delta x_{adj} = \Delta x \times \frac{1}{n} \sum_{i=1}^{n} \left(\frac{2r_z}{r_x + r_y} \right) \quad \textbf{(8)}$$

$$\Delta y_{adj} = \Delta y \times \frac{1}{n} \sum_{i=1}^{n} \left(\frac{2r_z}{r_x + r_y} \right) \quad \textbf{(9)}$$

Where r_x, r_y and r_z is the radius of each TRAP-cage in the *x*, *y* and *z* direction respectively and n is the number of measurements taken.

The distance between adjacent holes (H_{adj}) was calculated as follows:

$$H_{adj} = \sqrt{\Delta x_{adj}{}^2 + \Delta y_{adj}{}^2 + \Delta z^2} \quad \textbf{(10)}$$

Since *H* is expressed from *r* as:

$$H = 2r \sin\theta \quad \textbf{(11)}$$

The diameter (*D*) can be expressed from *r* and *H* as:

$$D = \frac{2rH}{\sqrt{4r^2 - H^2}} \quad \textbf{(12)}$$

$$\because\ D = 2r\tan\theta = 2r\frac{\sin\theta}{\cos\theta} = \frac{2r\sin\theta}{\sqrt{1-\sin^2\theta}} \quad \textbf{(13)}$$

Where $0° < \theta < 90°$.

Calculation of the angle between rings

From the above calculation, the dihedral angle between the ring structures (θ') was also obtained from the following equation.

$$\theta' = 2 \times (90 - \sin^{-1}\theta) \quad \textbf{(14)}$$

From 73 measurements from 20 TRAP-cage structures, the mean distance of the holes (H_{adj}) was calculated as 6.7 nm $\pm$ 1.4 (SD). The average diameter of the ring (*D*) was calculated as 7.5 nm $\pm$ 1.9 (SD), and the average angle between rings was 138° $\pm$ 10 (SD). The histogram of each results are shown in **Figure 2.15 (D)** and (**E).** From this calculation, the rings on the TRAP-cage were found to be approximately equal to the expected diameters of the original TRAP rings.

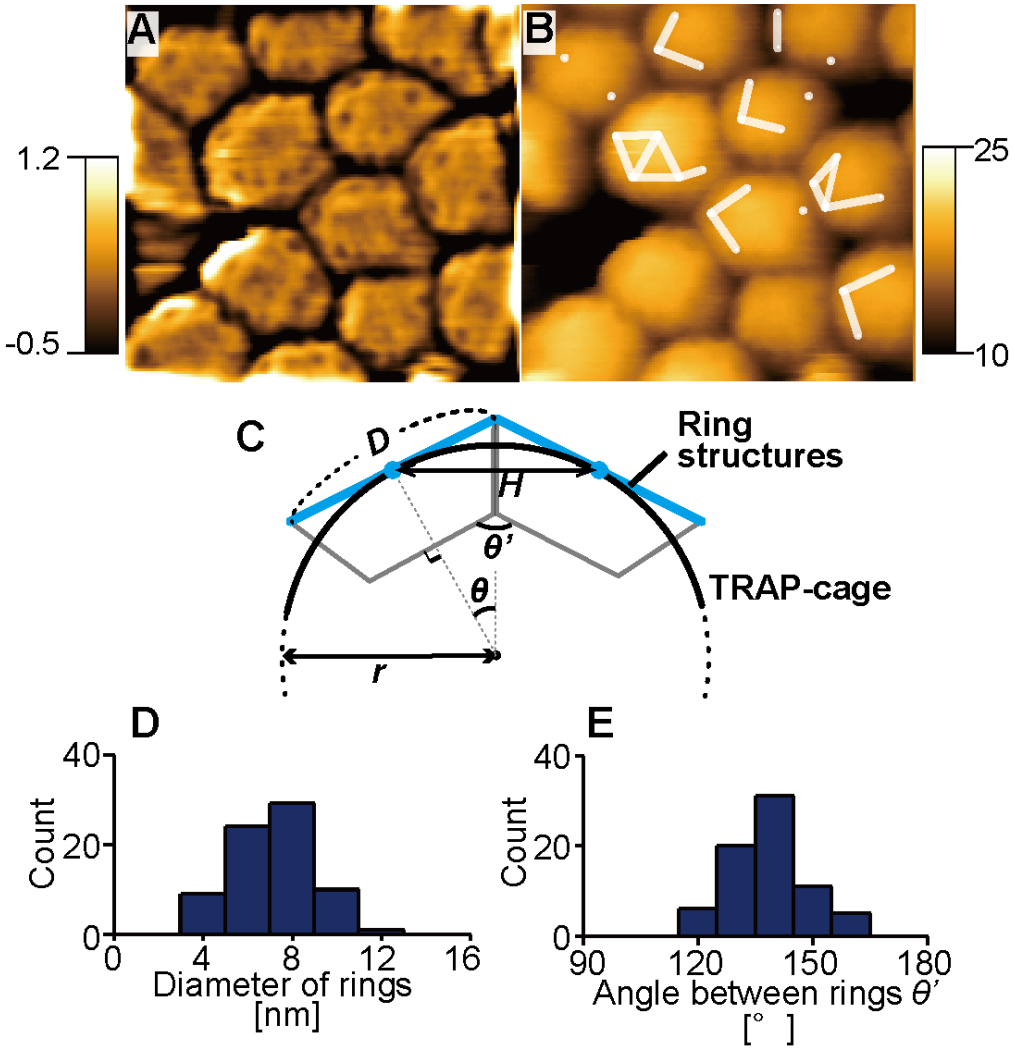

Figure 2.15 Ring structures in the Au1.4MS TRAP-cage[22]
(**A**) Average image of 8 HS-AFM frames which were processed using a high pass FFT frequency filter and averaging filter prior to averaging. (**B**) Average image of the same 8 frames as in (**A**), this time unprocessed, with the distances between adjacent holes represented as white lines. (**A**) and (**B**) are images of areas 94 nm × 90 nm. (**C**) Cross-section representation of a TRAP-cage showing two adjacent TRAP rings on the surface, with a line segment representing the TRAP-cage radius *r* running from the center of the TRAP-cage to the midpoint of one of the TRAP rings. The linear distance between the center of the holes is denoted by *H*, the blue line segments *D* represent the diameter of the ring structures on the surface of TRAP-cage, and θ'represents the dihedral angle between two adjacent ring elements. (**D**) Distribution profile of *D* based on 73 measurements. (**E**) Distribution profile of θ' based on 73 measurements.

[22] Reprinted with permission from (Figure S2 of Imamura, *et al.*, *NanoLett.*). Copyright (2015) American Chemical Society

2.3.9. TRAP-cage ring stoicheometry

Given that the TRAP-cage appears to be composed of TRAP rings, the question arises as to how many rings form the structure. To answer this question, we used two approaches. The first approach was to estimate from the number of distinguishable rings **Figure 2.16 A**. Another approach was to estimate from a consideration of symmetry **Figure 2.16 B**. As described in **Figure 1.2** (page 20), globular proteins usually have either icosahedral symmetry or octahedral symmetry (icosa: twenty; octa: eight). Such symmetrical proteins have a certain discrete number of subunits. For example, icosahedral protein is composed of multiples of 60 subunits with 3, 5 and 2 rotational axes[23] [88, 89]. Therefore, to find symmetry axes is a clue to the number of rings on the TRAP-cage.

Surface area calculations

The surface area of TRAP-cage was estimated using area calculations from high-resolution HS-AFM images (**Figure 2.16 A).** The visible area of TRAP-cage was first determined from the Gauss and high pass frequency filtered image (shown in (iii), in red). This marked area was then converted into a binary image and superimposed onto the original image to clarify the area of TRAP-cage (iv), from which the area of TRAP-cage was measured. In the same way, the area of 8 distinguishable rings from a different frame (4.5 s later) was calculated as shown in v-viii. The visible surface area of TRAP-cage was estimated to be 1100 nm^2, while the surface area of the 8 rings was 690 nm^2. Therefore, the visible area of the TRAP-cage is equivalent to 13 TRAP rings. By assuming that the

[23] The multiply number of 60 is called Triangulation number (T), ($T = h^2 + hk + k^2$, h, k are non-negative integers ($\mathbb{N}$). If T=3, the protein is composed of $60 \times 3 = 180$ subunits

visible area of TRAP-cage under HS-AFM corresponds to half of the total area of the spheroid, the number of rings in the TRAP-cage was estimated as approximately 26.

From **Figure 2.16 A,** where the cages and individual rings are both present, it is also interesting to note that GNPs are not observed on the outer surface of the formed TRAP-cage. In these cases the rings all contain a bound GNP in the centre while the rings in the cage all appear "empty". This may be due to the fact that the two "flat" faces of a TRAP ring have different diameters and charge characteristics and one may favour GNP binding. If this face is on the inner surface of the cage, the HS-AFM image of the ring should look empty even if GNPs are bound to the face of the ring on the "inside" of the cage.

Symmetry of TRAP-cage

By averaging the frames, the ring structures can be also clearly seen at lower resolutions as seen in **(B)**. In some cases the TRAP rings on the cage were arranged in either equilateral triangular or square arrangements. The presence of four-fold rotational axes symmetry, along with three- and two-fold symmetry, raises the possibility of an overall octahedral symmetry, which would necessitate 24 rings (**Figure 2.16 B).**

Both surface area calculation and symmetry of TRAP-cage were based on the assumption that the packing of rings is regular, which is reasonable judging from the high monodispersity of the TRAP-cage. However, since distinguishable ring structures can be imaged only in the top surface of the cages, and the appearance of the rings was not always the same. Higher resolution imaging is necessary to make a clear answer. In this thesis, from two method of HS-AFM imaging, I would estimate that the TRAP-cage is composed of 20-30 rings.

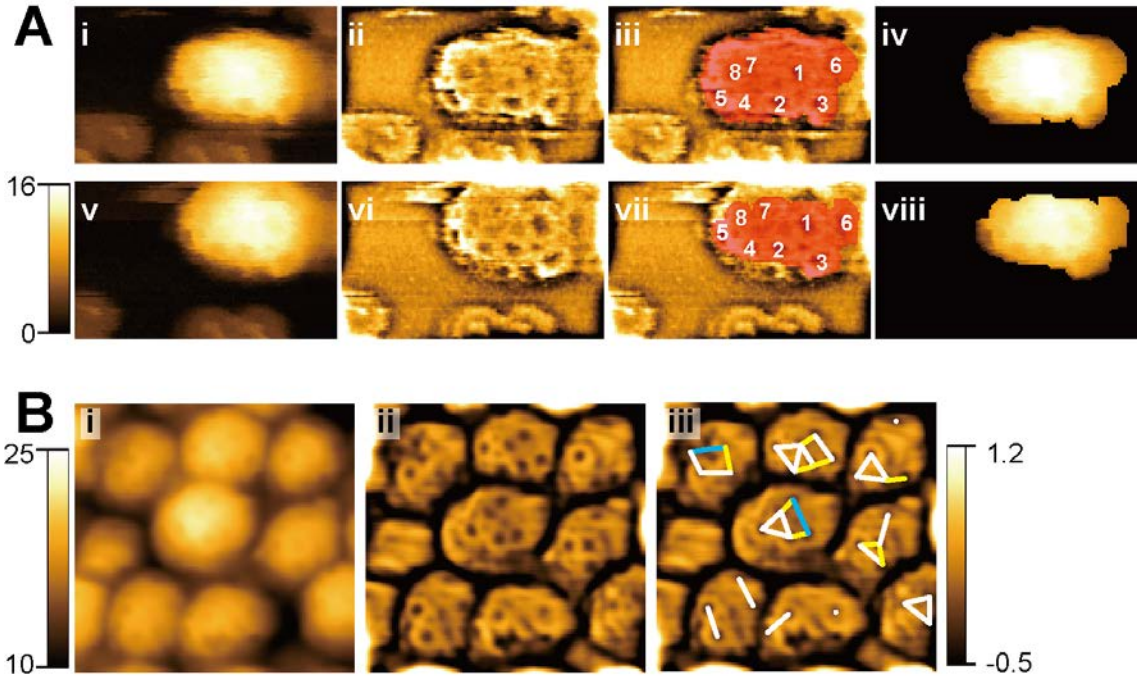

Figure 2.16. Estimating number of ring structures in the Au1.4MS TRAP-cage[24]
(**A**) Estimation based on area calculations. (i-iv) and (v-vii) correspond to two separate HS-AFM time frames of a single TRAP-cage structure, which is also the same as shown in **Figure 2.14**. (i) and (v) unprocessed images. (ii) and (vi) images processed as in **Figure 2.14.** (iii) same image as in (ii), with the visible area of TRAP-cage marked in red. (iv) same image as (i), with the area marked in (iii) elevated for emphasis. (vii) the area representing eight ring structures is marked in red, and (viii) superimposed upon the original image. The image size is 60 nm x 35 nm. **(B)** Estimating number of rings based on apparent symmetry elements. This image is the average of 23 frames selected from 26 s – 57 s after addition of 14 mM acetate buffer pH 4. The image size is 85 nm x 80 nm. (i) averaged image of 23 frames of average filtered HS-AFM images of TRAP-cage sample. (ii) the same averaged image with HP-FFT filter. (iii) location of isolated central holes of the ring structures (white dots) and distances between the central cavity of adjacent rings (lines). The colors of the lines represent the distance (yellow: 4 nm to 5.5 nm; white: 5.5 nm to 8 nm; blue: 8 to 10 nm). Apparent local 4-fold and 3-fold axes of symmetry are observed. Color scale on the left is for (i), and on the right is for (ii) and (iii).

[24] Reprinted with permission from (Figure S3 of Imamura, *et al*.). Copyright (2015) American Chemical Society

Nanogold

The diameter of ring structures on the TRAP-cage made with Nanogold were also measured using the same method as described in **Chapter 2.3.8** and the rotational symmetry was also investigated as described in **Chapter 2.3.9** (**Figure 2.17)**. From 47 measurements from 13 TRAP-cages, the mean distance of the holes (H_{adj}) was calculated as 8.2 nm $\pm$ 1.6 (SD). The average diameter of the ring (*D*) was calculated as 8.9 nm $\pm$ 2.1 (SD), and the average angle between rings was $137° \pm 9$ (SD). These values were close (within error derived from calculation methods and original image resolution) to the values calculated for TRAP-cage made with Au1.4MS. In addition, equilateral triangular or square arrangements were also found from the Nanogold TRAP-cage.

Therefore, TRAP-cage structure made from Au1.4MS and Nanogold are expected to be identical or very closely related structures.

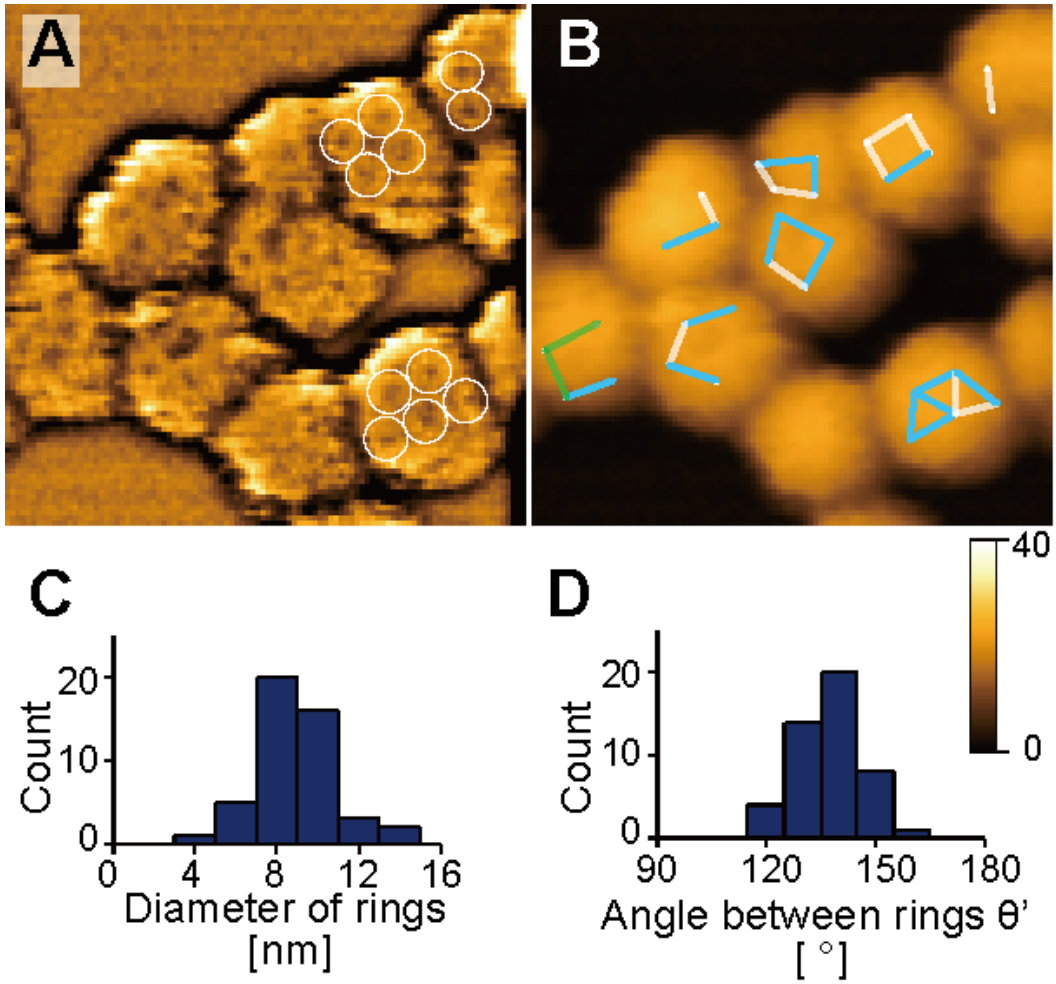

Figure 2.17.Ring structures in the Nanogold TRAP-cage
(**A**) HP-FFT frequency filter and Gaussian filtered image. (**B**) Gaussian image of the same frame as in (**A**) showing the distances between the central cavity of adjacent rings (lines). The colors of the lines represent the distance (white: 5.5 nm to 8 nm; blue: 8 nm to 10 nm; green: 10 nm to 12 nm) after adjusting the horizontal distortion. (**A**) and (**B**) are images of areas 150 nm × 150 nm. (**C**) Distribution profile of Diameter of rings based on 47 measurements. (**D**) Distribution profile of θ' as in **Figure 2.15 C** based on 47 measurements.

2.3.10. TRAP-cage with DTT

It was hypothesized that the TRAP-cage structure was formed via disulfide bonds between TRAP-K35C [50]. As shown in **Chapter 2.3.4** where reducing agent, DTT, was added during HS-AFM observation to probe real time break-up of the cage structure, causing reversion to the original ring structures (Au1.4MS TRAP-cage: **Figure 2.18** Nanogold TRAP-cage: **Figure 2.19**).

HP-FFT filtering showed some individual TRAP-K35C rings in the HS-AFM image of TRAP-cage formed with Au1.4MS (**Figure 2.18 B**). Upon addition of 1.4 mM DTT (at 0 s) the overall spherical shape was retained for several minutes, although cracks on the surface gradually increased in size (**D-I**), most noticeably in the processed images, presumably a consequence of the breaking of inter-ring disulfide bonds. By 154.5 s the overall form was still maintained, but at 155 s (0.5 s later) the entire TRAP-cage suddenly opened up in a "clam-shell" fashion (**J** and **K**). Upon opening, some of the cage material was lost to the surrounding medium, whereas some appeared to lie flat on the mica surface (**L** and **M**). At this stage the individual TRAP rings were hard to discern (**N**), however a gradual re-formation of discrete ring structures was observed from 156 s – 214 s through an unknown process (**L–T**), with the occasional sudden loss of individual TRAP rings to the surrounding medium (**P** and **Q**). The remaining material on the mica surface was estimated to be 13 TRAP-K35C rings (**S**). It is intriguing that the discrete and unambiguous ring structures present in the fully-formed TRAP-cage were not visible after "bursting" and recovered only gradually (e.g. compare panels (**L**) and (**T**)). This suggests dynamic rearrangements in protein structural conformation possibly due to non-synchronous disulfide bond reduction.

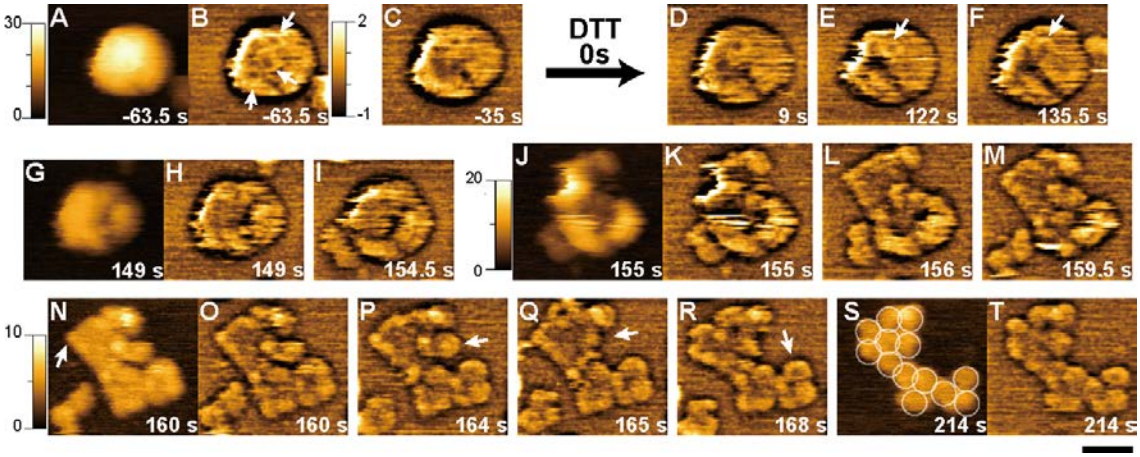

Figure 2.18 DTT-induced disassembly of Au1.4MS TRAP-cage[25].
Time course of structural changes observed in a TRAP-cage with the addition of DTT. The Gaussian and HP-FFT frequency filtered images were processed as in **Figure 2.14**. For certain key images, original images are also shown (**A**, **G**, **J**, **N** and **S**). DTT at 1.4 mM was added to the TRAP-cage sample on the mica surface at 0 s. (**A**) - (**I**) are 56 nm x 48 nm. (**J**) - (**T**) are 60 nm x 55 nm. In order to ensure better contrast, the color intensity height scale for the original images was changed over time and is as follows: 0 to 30 nm for (**A**) and (**G**), 0 to 20 nm for (**J**), and 0 to 10 nm for (**N**) and (**S**). The color scale for all processed images is shown between (**B**) and (**C**). Arrows in (**B**) and (**E**) show ring structures on the surface of the TRAP-cage. The arrow in (**F**) indicates a cleaved ring structure. The arrow in (**N**) shows irregular structures. Arrows in (**P**) and (**Q**) indicate a ring that was lost to the medium. The arrow in (**R**) indicates a ring structure resembling the original TRAP-K35C. The number of remaining ring structures are estimated in (**S**) indicated as white circles. Scale bar (bottom right) is 20 nm.

[25] Reprinted with permission from (Figure 4 of Imamura, *et al.*). Copyright (2015) American Chemical Society

This disassembly process was reproducible and showed almost the same effect with the TRAP-cage made with Nanogold **Figure 2.19**.

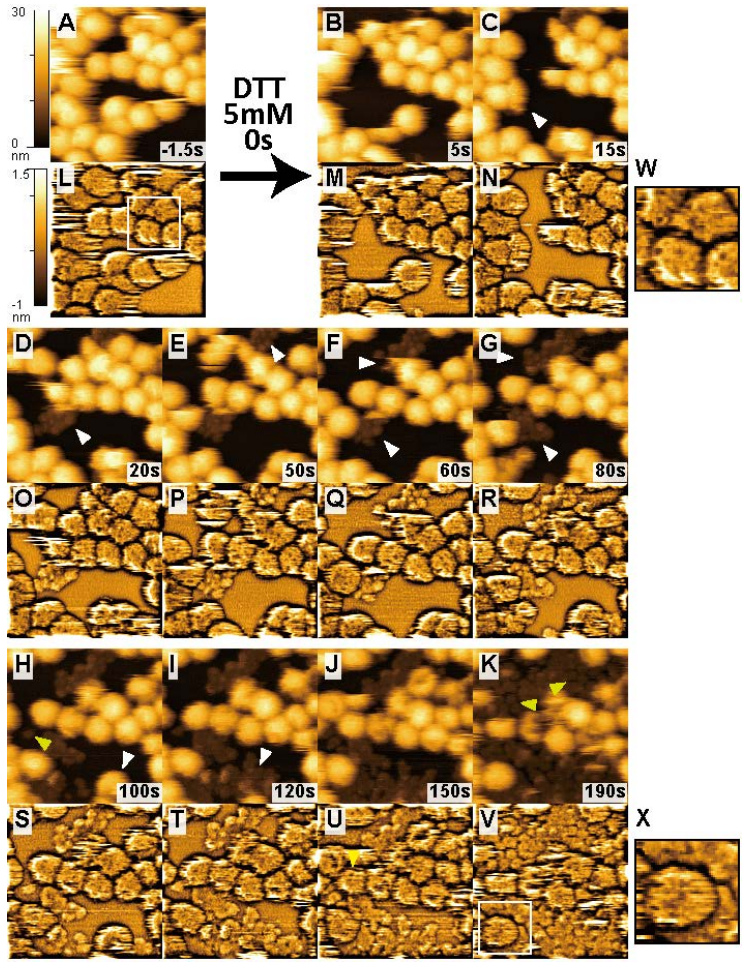

Figure 2.19. DTT-induced disassembly of Nanogold TRAP-cage.[26]
TRAP-cage was formed with Nanogold. Original images and processed (Same processing as in **Figure 2.14**) images of HS-AFM are shown together at each frame (above for original and below for the processed images). **(A)**, **(L)** are before addition of DTT and the rest of the images are after the addition of 5 mM DTT. The dramatic breakage of TRAP-cage structures are shown by white arrows in the original images. The isolated ring structures are shown by light green arrows in **(H)** and **(K)**. In the processed images, ring structures can be seen often before the addition of DTT, as seen in the 2x enlarged image (**W**) from (**L**). Most TRAP-cages were broken down after 100s. Ring structures were sometimes observed in TRAP cages, as shown in the 2x enlarged image (**X**) from (**V**). The color scale for original and processed images are 0 to 30 nm and -1 to 1.5 nm respectively. The size of the images of (**A**)-(**V**) are 150 nm x 150 nm, (**W**) and (**X**) are 50 nm x 50 nm.

[26] Same data but different image process from Figure S4 of Imamura, *et al*. 2015

2.3.11. TRAP-cage and TRAP-K35C under acidic conditions

To further test the hypothesis that TRAP-cage may include disulphide bonds between TRAP rings, the stability of the TRAP-cage under acidic conditions was compared to the stability of TRAP-K35C, which does not include disulphide bonds or indeed any covalent bonds between individual protein monomers. Breakdown of the TRAP-cage structure was observed by adding a strong acid under HS-AFM (**Figure 2.20 A**). The overall TRAP-cage structure appeared relatively stable under low pH conditions, with no discernible change in appearance under 28 mM sodium acetate (NaOAc). Further addition of HCl (up to 42 mM), led to the eventual degradation of the TRAP-cage structure which occurred via a "melting" of the entire cage structure, in contrast to the clam-shell style of breakage observed with the addition of DTT. This breakage could be caused by the local strong acid condition. The "melting" occurred only upon a second addition of HCl, but the breakage stopped after some time (possibly due to diffusion of the acid to the observation buffer) and further breakage did not occur after a third addition of HCl.

In comparison, TRAP-K35C ring structures were seen to be less resistant to acid-induced degradation compared to the TRAP-cage spheres (**Figure 2.20 B**). With TRAP-cage the overall structural integrity is preserved at 28 mM NaOAc, however in the case of TRAP-K35C, the ring structures began to degrade under these conditions, and seem to dissociate into individual TRAP subunits. The structural breakdown of TRAP-K35C rings under acidic conditions is also likely to be promoted by the tapping action of the AFM tip, since moving to fresh areas on the mica surface typically revealed TRAP-K35C in less advanced states of degradation.

These results suggest that the cage structure can tolerate acid conditions that individual ring structures cannot survive. This is consistent with the TRAP-cage being held together by a network of disulfide bonds strong enough to preserve the cage structure.

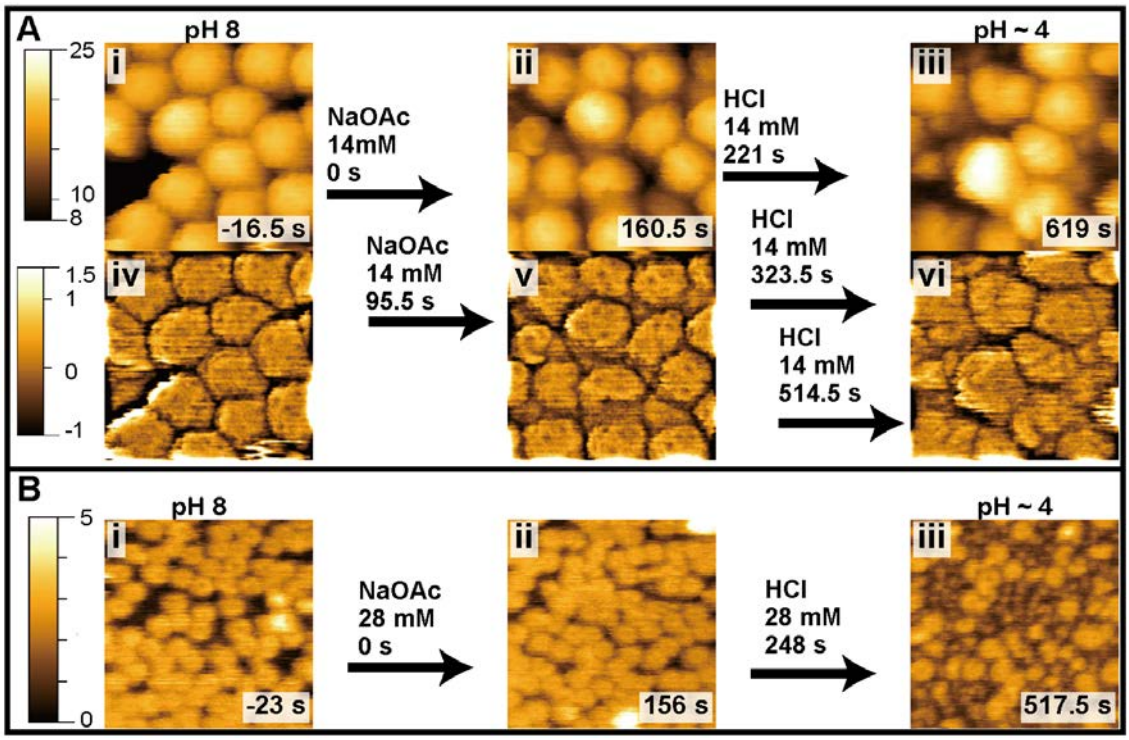

Figure 2.20.Au1.4MS TRAP-cage and TRAP-K35C against acid[27]
Effects of exposure to acidic conditions of **(A)** TRAP-cage and **(B)** TRAP-K35C. In both cases, the observation buffer contained 20 mM Tris-HCl, pH 8 before addition of acids, and the final sample was approximately pH 4, as indicated using pH paper. **(A)** (i)–(iii) unprocessed HS-AFM images of TRAP-cage; (iv)-(vi) the corresponding processed images (same process as in **Figure 2.14**). Times indicate seconds before or after the initial addition of NaOAc, pH 4.5. (iii) and (vi) were taken after addition of HCl. Concentrations indicated upon each acid injection shows the final concentrations of each addition with respect to the total sample volume. In total, 28 mM NaOAc pH 4.5, and 42 mM HCl was added to the TRAP-cage sample. **(B)** Similar to the experiment shown in **(A),** (i) shows TRAP-K35C before initial addition of NaOAc, pH 4.5, (ii) after addition of NaOAc pH 4.5, and (iii) after addition of HCl, with the corresponding elapsed times indicated.

[27] Reprinted with permission from (Figure S5 of Imamura, *et al*.). Copyright (2015) American Chemical Society

2.3.12. Disassembly of cage structures made without GNPs

In the TRAP-cage disassembly process via DTT, immediately after the loss of the sphere structure, individual protein subunits are not discernible as rings, as described in **Chapter 2.3.10**. This could be due to the co-existence of GNPs in solution together with DTT, which could have caused protein shuffling as seen clearly in **Figure 2.10** and **Figure 2.11.** To eliminate the effect of GNPs, TRAP-cage made without GNPs was tested for break down by DTT. (**Figure 2.21**). From the HS-AFM observation, the overall appearance was very similar to TRAP-cage made with GNPs, except the smaller size (the mean height of this cage was approximately 15 mm). The significant difference was the tolerance against DTT. The addition of DTT was not as efficient at causing TRAP-cage break-up compared to TRAP-cages made with GNPs. Even 20 min after the addition of DTT, there were cage structures which looked intact. In addition, after the cage disassembly, disordered structures remained and typical TRAP ring structures were not observed. This suggests that this cage structure could have been formed not only via disulfide bonds, but by additional interactions of proteins. This is probably because this cage structure was formed through urea denaturation which allow additional protein-protein confirmations to be explored. Compared to the strong stability against acid of TRAP-cage made with GNPs, this cage structure was broken easily in ultrapure (Milli-Q, Millipore Corporation) water (~ pH5-6) due to the tapping force of the AFM. A representative breakage is shown in **Figure 2.22**.

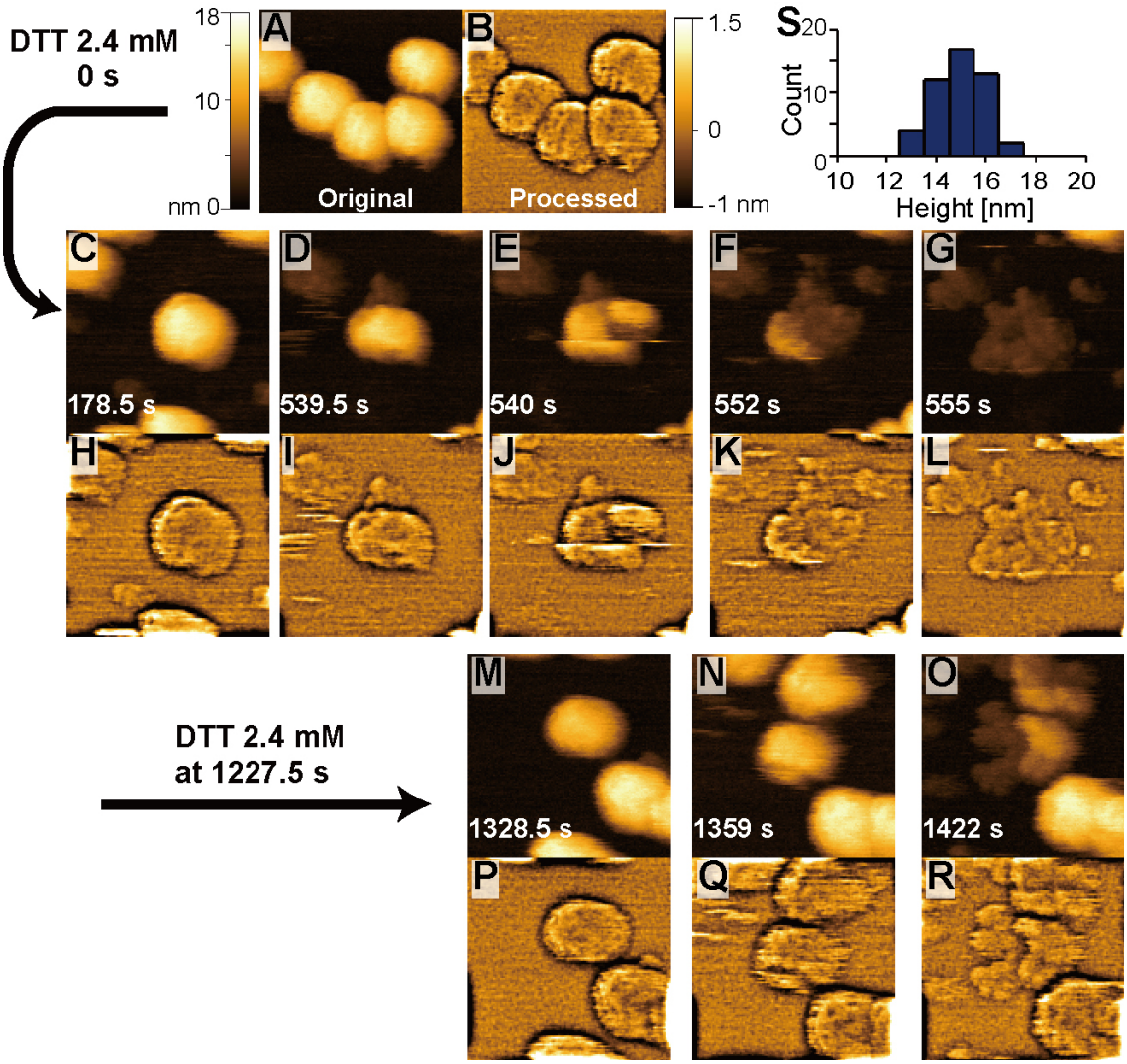

Figure 2.21 DTT disassembly of cage structures made without GNPs
AFM image of cage structures made without GNPs **(A)** and **(B),** and after addition of 2.4 mM (final concentration) DTT at 0 s and 1227.5 s (**C**)-(**R**). The processed image on the right, or beneath the original pictures, are Gauss filtered and high pass FFT frequency filtered (10nm). The histogram of the height of 48 cages made without GNPs before addition of DTT is shown in **(S).** The mean height was 15 nm ± 1 (SD). The size of images are 100 nm x 100 nm.

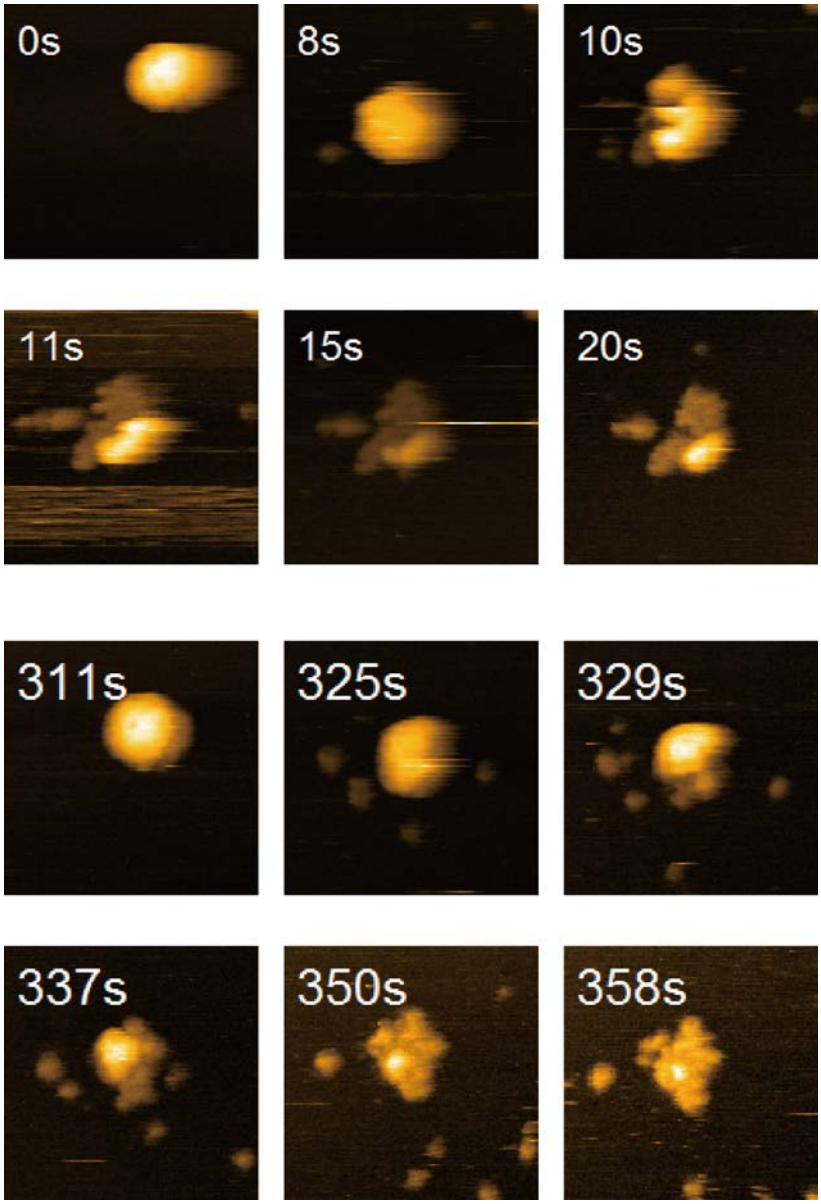

Figure 2.22 Breakage of cage structure made without GNPs in Milli-Q water
Continuous observation of different cage structure breakages (0 s -20 s and 311 s -358 s). Color scale was auto adjusted. The size of images are 100 nm x 100 nm

2.3.13. Analytical ultracentrifugation

So far, I have been shown only HS-AFM imaging results. Although HS-AFM images are convincing it is preferable to compare with results from other methods. Electron microscopy observation has previously been reported by the Heddle group [30] **Figure 2.2**, page 40. I have tried analytical ultracentrifugation (AUC) analysis to try to calculate the molecular weight (MW) of the TRAP-cage.

The benefit of using analytical ultracentrifugation is that the MW can be determined regardless of the shape of the molecule. Also, it can separate different types of material during the analysis (i.e. TRAP-cage and GNPs). And as compared to electron microscopy and HS-AFM, AUC gives general information for the sample as a whole such as distribution of the MW (size) and the dissociation constant between TRAP rings and TRAP-cage [90].

There are two types of analysis for AUC, one is sedimentation velocity, and the other is sedimentation equilibrium. In this experiment, I tried the former for identifying the MW of the TRAP-cage. This method is based on the conversion from the sedimentation coefficient (*s* [S]) following well-known Svedberg equation [91].

$$\mathrm{M} = \frac{sRT}{D(1 - \bar{v}\rho)} \qquad \textbf{(15)}$$

where M is molar weight [g mol^{-1}] (equal value to MW), $\bar{v}$ is the partial specific volume (0.7-0.75 [cm^3g^{-1}] for protein, ρ is the density of the solvent (1 [g cm^{-3}] for water), D is the diffusion coefficient [cm^3s^{-1}], R is the gas constant (8.314 [$JK^{-1}mol^{-1}$] or [kg m^2 s^{-2} $K^{-1}mol^{-1}$]) and T is the absolute temperature (293.15 [K]). The unit of sedimentation

coefficient is the Svedberg (S) (1 S = 10^{-13} sec). From this equation, solving for the sedimentation coefficient gives MW.

TRAP-cage composed of 20-30 TRAP rings would be 1.8 MDa- 2.7 MDa (One ring is 90.4 kDa). From the AUC result in **Figure 2.23**, the MW was calculated from the weight averaged main peak of 58.1 [S]. By assuming that D= 2.1 x 10^{-7} [cm^2s^{-1}] from **Equation (6)** with α= β=10 nm at 20 ℃ and $\bar{v}$ =0.73, 58.1 [S] is calculated as ~2.45 MDa (Equivalent to ~27 rings). MW was also calculated from SEDFIT software based on the fitted curve, and it was ~1.7 MDa (Equivalent to ~19 rings). This difference could be because of the friction ratio estimated from the software was low compared to the standard value of 1.2, which represent spherical shape. Although in this AUC experiment, the sedimentation coefficient was very broad due to the fast centrifugal speed for the TRAP-cage, the MW was approximately the same as calculated value from HS-AFM observation. The Heddle lab has tried another trial, in that case, sedimentation coefficient value was 63.5-66.6 [S] (data not shown), from this value, MW was 2.7-2.8 MDa (30~31 rings). The deviation between the first trial and the other trial could be due to the differences in purification of TRAP-cage. In the first trial, TRAP-cage was purified with sucrose density gradient to remove extra GNPs.

From AUC analysis, the MW was calculated as similar to that calculated using the number of rings per TRAP-cage as estimated from HS-AFM. And the distribution of the sedimentation coefficient suggested that TRAP-cage is a relatively monodisperse structure. However, the MW measured in this experiment could include a contribution from GNPs, since they seemed to bind to the TRAP-cage and were difficult to remove. Given stochastic binding, the amount of GNPs could be vary for each TRAP-cage.

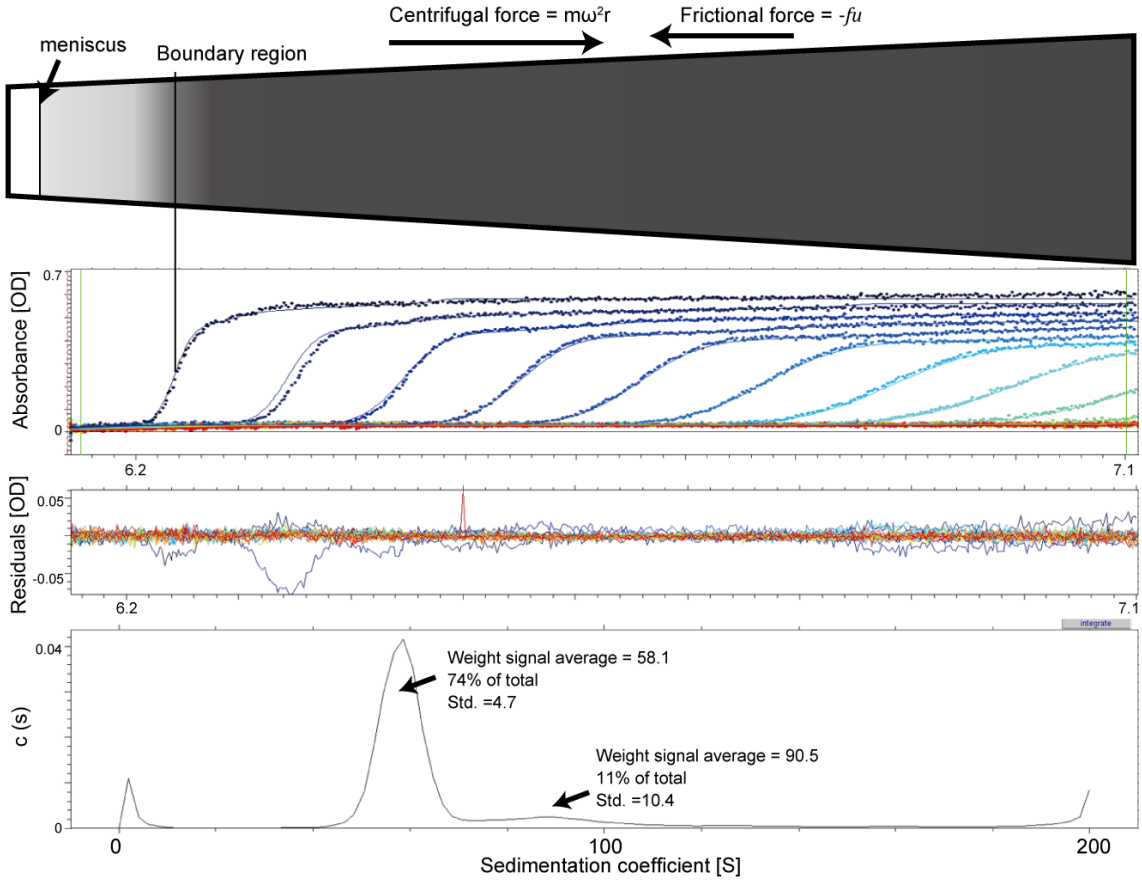

Figure 2.23 Analytical ultracentrifugation analysis of TRAP-cage produced using Nanogold

Analytical ultracentrifugation of TRAP-cage. Top graph is illustrative of a general sample solution in the AUC cell. Protein particles migrate due to centrifugal force − friction force. The second graph shows absorbance data against radius from center with fitted curves (each line represents different time, with time increasing in the positive x-direction); The third graph shows residuals [OD] from the fitted curve. The rmsd value was 0.0065 (below 0.01 is considered good fitting). The bottom graph shows distribution of sedimentation coefficient (s). The major peak at 58.1 [S] corresponds to ~2.5 MDa, and miner peak at 90.5 [S] corresponds to ~3.8 MDa. Other lower and higher peaks may be artifacts. This AUC experiment and data analysis was kindly done by Prof. Fumio Arisaka.

2.4. Summary

HS-AFM provided novel insights into the dynamics of the TRAP-cage structure that have not been revealed using other methods. A summary of the results related to HS-AFM is illustrated in **Figure 2.24**. Through AFM analysis of TRAP-cage and its component proteins under various conditions, I was able to address all three questions posed on page 48.

i) Conformational changes: These changes occurred not only within the single ring protein, but also appeared to occur between the rings via possible "subunit shuffling" with the addition of GNPs. Also, GNPs led to the aggregation of TRAP-K35C where individual rings were gradually became difficult to discern as discrete entities. Negatively charged Au1.4MS had quicker and greater effect compared to non-functional Nanogold. Compared to the mutant TRAP, TRAP-WT did not form aggregated structures, but GNPs were captured in the central cavity of the ring, which was probably due to the electro static interaction and size matching.

ii) Detail structure of TRAP-cage: A higher resolution AFM structure of TRAP-cage was obtained, and by combining the high resolution image with image processing, the TRAP-cage was revealed to be composed of ~20-30 close-packed TRAP-K35C rings. The AUC result also supported the idea that the TRAP-cage was composed of approximately 25 rings.

iii) Role of GNPs: GNPs probably function in TRAP-cage assembly as an initiator. Addition of GNPs lead to the aggregation of TRAP-K35C. GNPs also appear to have a role in conformational changes of TRAP-K35C. These changes may allow formation of a disulfide bond between cysteines. The similarity of TRAP-cage made using Nanogold

compared to Au1.4MS, along with the lack of structural change when TRAP-WT is used suggests that the interaction of GNPs with the central TRAP cavity (the proposed electrostatic interaction effect) was not involved in the formation of TRAP-cage, but instead a catalytic-like activity of GNPs in promoting disulfide bond formation was the key to TRAP-cage formation in the presence of GNPs. In comparison, a cage structure made without GNPs has similar shape, but a more irregular pattern. Urea denaturation may function in a similar fashion to GNPs, but the difference is that the resulting TRAP-cages are often misformed, which cannot be repaired by subsequent addition of GNPs.

In addition, HS-AFM revealed very clearly the break up process of the TRAP-cage, which was distinguishably different process from breakage by strong acid.

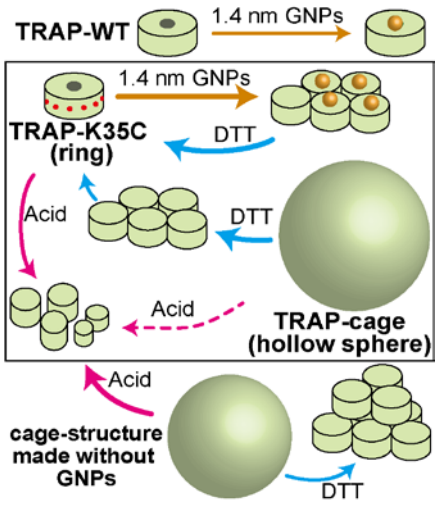

Figure 2.24. Summary of HS-AFM observation[28]
Processes viewed under HS-AFM is summarized. Orange arrow represents the addition of 1.4 nm GNPs; blue arrow represents the addition of DTT; and pink arrow represents the addition of acid. Black squared box are the main experiments, and the outside the box are the control experiments to see the difference. The thickness of arrow represents how quick the reaction occurs.

[28] Adapted with permission from (Figure 5 of Imamura, *et al.*). Copyright (2015) American Chemical Society

Chapter 3

Nanoengineering of DNA Minicircles as a template for gold nanoparticles

3.1. Introduction

In chapter 2, the thermostable ring protein TRAP was transformed into a sphere by the addition of GNPs. Observation of dynamic structural changes associated with this novel phenomenon was carried out in real time using HS-AFM. However, in terms of the original purpose of application for metamaterials, TRAP did not work well as a template of GNPs. Therefore, I used an even more robust and simple artificial circular biomolecule, a DNA minicircle (DNA-MC). The DNA-MC I used is a 168 bp long double stranded, closed circular DNA, approximately 20 nm in diameter (commonly known closed circular DNAs, plasmids, are typically 3 -5 kbp). In this chapter, I will discuss the DNA-MC as a template for gold nanoparticles for metamaterials.

3.1.1. DNA Minicircle

In 1986 Ulanovsky et al demonstrated that DNA containing a periodic repeat of six and five adenine-thymines (A-tract) can form a circular DNA structure with a minimum of 105 base-pairs (bp) [92]. This is because periodic A-tract sequences makes DNA take up an intrinsic curved structure. The main contributions to this curvature are a positive roll angle in the A-tract region, which makes the DNA bend towards the minor groove of the A-tract; and a negative roll at the G-C pair, which makes the DNA bends towards the major groove of the adjacent G/C sequences. Both of the bendings are in the same direction which results in the observed curvature [93]. From NMR spectroscopy experiments, a continuous ten bp sequence containing six continuous AT pairs was discovered to have intrinsic bend of 19° (i.e. ~189 bp equals to 360 °). The curvature of the DNA structure can be reduced by inserting G-C pairs within the six A-T repeats [94].

3.1.2. Modification of DNA minicircles

As described in **Chapter 1.4.1**, progress in nanoengineering with DNA has demonstrated that DNA is a good biomolecule for templating gold nanoparticles. The common strategy for attaching gold nanoparticles onto DNA employs DNA with a with 5′- end or 3′– end thiol modification of single stranded DNA (ssDNA), which makes strong Au-S covalent bond between gold nanoparticles and DNA [46, 54, 95]. The drawback of this technique is that GNPs can attach only at the end of DNA, this disallows ligating DNA ends. To apply the thiol technique for the closed circular DNA, I used phosphorothioate modified DNA (PS-DNA), where the thiol modification is on the phosphate backbone of the DNA. PS-DNA itself cannot attach GNPs, probably due to the steric hindrance, but this problem was solved by using the bifunctional linker, BIDBE [96].

3.1.3. Bifunctional linker BIDBE

N,*N*'-bis(a-iodoacetyl)-2,2'- dithiobis (ethylamine) (BIDBE) [97] facilitates the attachment of AuNPs onto thiol groups of DNA [96]. BIDBE contains an iodoacetamide group at both ends and a disulfide bond in the middle. The iodoacetamide functional group has been shown to react with the phosphorothioate group specifically, while the disulfide bond, upon reduction to a thiol group, can react with the GNPs. Combining the phosphorothioate modification and this BIDBE linker makes DNA-MCs a programmable attachment point for GNPs.

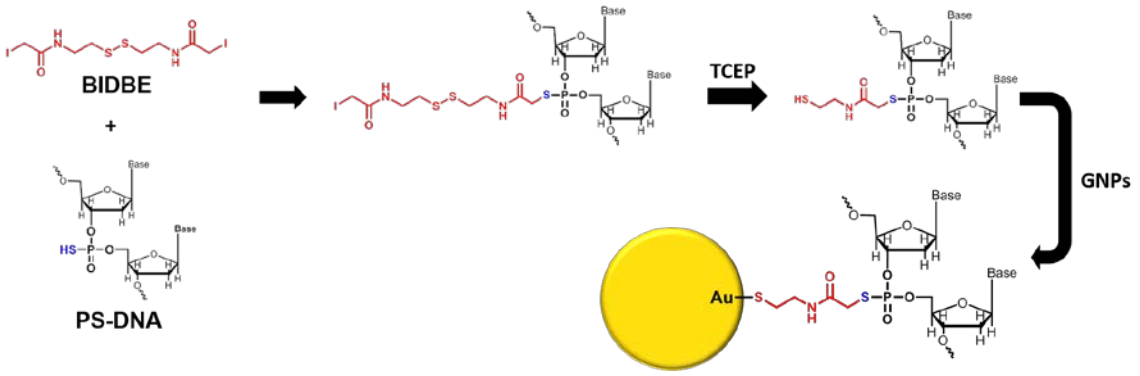

Figure 3.1. BIDBE: Reaction with PS-DNA and its usage as a linker.

3.1.4. Metamaterials with DNA gold nanoparticles

Recently, DNA has been investigated with the aim of producing metamaterials or optically responsive materials because of the programmable feature of DNA in which GNPs can be arrayed onto the DNA structure 2 dimensionally [98] or even 3 dimensionally [99, 100]. This arraying of GNPs gives them special optical characteristics which do not occur with GNPs on their own. For example, helical arrangement of GNPs using DNA origami showed chirality in a plasmonic response, which was confirmed with circular dichroism (CD) [99]. In the same way, GNPs arrayed in circle could work as a metamaterial as described in **Chapter 1.8**. If the small gaps between GNPs act as capacitors (C), and the circular structure in total act as a coil (L), this metamaterial unit would have a resonance frequency derived from this property as a LC circuit, whose resonance could be as fast as that of optical light if the structure is smaller than the wavelength of light **Figure 3.2.**

It has already been shown that circularly arrayed GNPs are able to react with optical light [101]. However, obtaining a high yield of designed structures is still challenging, but necessary if a strong and sharp response to the light is to be achieved.

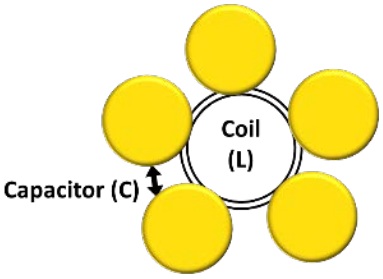

Figure 3.2. LC circuit composed of GNPs on a DNA-MC
The gap between GNPs works as capacitor (C) and the circular arrangement of GNPs works as coil (L), forming a LC circuit.

3.1.5. Gold nanoparticle ligand

GNPs were synthesized with citrate. However, addition of NaCl, which is required in the attachment process to DNA-MC, causes GNPs to aggregate because the negative charge of citrate was neutralized by the NaCl. To prevent this, a ligand which binds more strongly to GNPs is preferred. Therefore, the citrate ligand was exchanged with polyethylene glycol-substituted alkane thiol, HS-C11-$(EG)_6$-OH (MW= 468, ProChimia Surfaces, Sopot, Poland) ("PEG-alkane thiols", or "PEG" in this thesis). Alkane thiol can form a self-assembled monolayer on the GNPs to stabilize them as illustrated in **Figure 3.3**. In other reports [99, 101], phosphine based ligands BSPP (bis-(para-sulfonatophenyl)phenylphosphine dihydrate dipotassium salt) was also used, which is also a good candidate to stabilize GNPs, however, I used mainly PEG to form a stronger Au-thiol bond. In addition, the stabilizing effect can be adjusted by changing the length and properties of the PEG molecule.

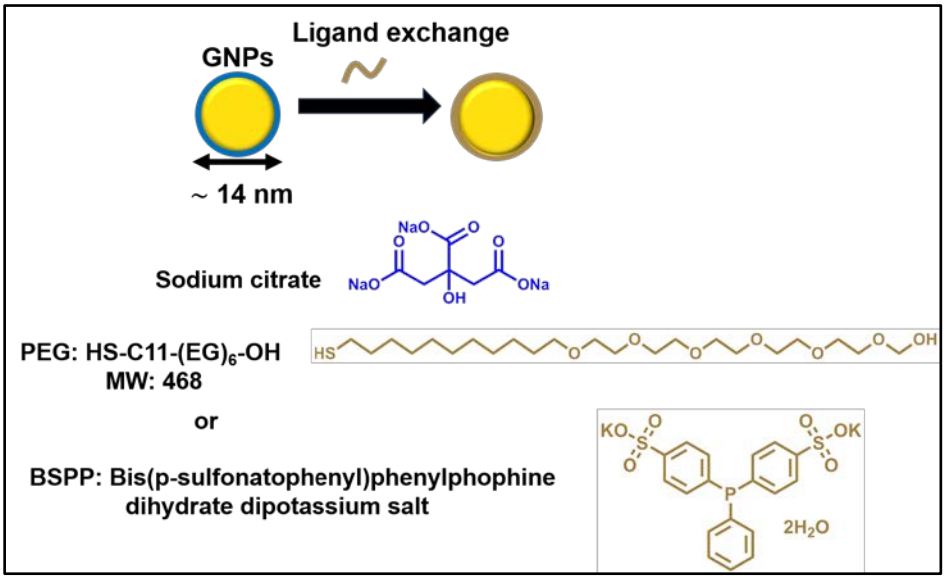

Figure 3.3. Ligands exchange of GNPs
See the text for the details.

3.1.6. Experimental scheme

The overall scheme is illustrated in **Figure 3.4**. (**Step I**) PS-DNA was mixed with the other ssDNAs (6 in total) followed by heating and cooling, which results in formation of a circular DNA structure. On this new structure, there are nicks which are ligated (bridging 5′ and 3′ end of deoxyribose phosphodiester bond) by a ligation enzyme to make a closed circular structure. The impurities were removed by exonuclease and then purified with a DNA purification column. (**Step II**) To this purified DNA-MC, BIDBE linker was attached at the phosphorothioate modifications, then the BIDBE is reduced with TCEP to expose the thiol group in the BIDBE linker. (**Step III**) To this exposed thiol group, GNPs stabilized with PEG-alkane thiols (PEG) were attached.

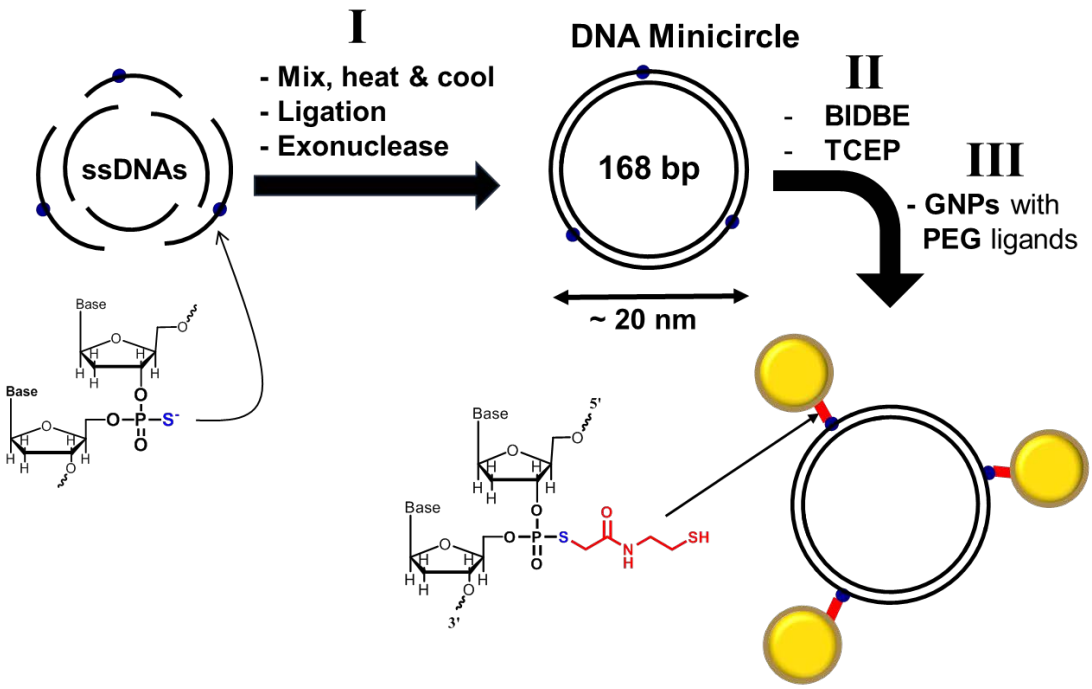

Figure 3.4. Scheme of the experiment
The each line represents ssDNA and blue spots on ssDNA are PS-modifications. Yellow circle represents GNPs and ochre circular line around GNPs represents PEG-alkane thiols (PEG). Red line between GNPs and PS-modification represent the reduced form of BIDBE.

3.2. Materials and Methods

3.2.1. Gold nanoparticle synthesis

Approximately 14 nm diameter GNPs were synthesized following the published method [102] which adapted the Turkevich –Frens method [41-43] with a kind support by Hadjer Salmi. A boiling solution of 1 mM (as opposed to the published 200 μM) of $HAuCl_4$ trihydrate in 200 mL of milli-Q was boiled and refluxed. While boiling, 20 mL of a hot (60 - 70 ℃) 40 mM aqueous solution of trisodium citrate was quickly mixed into the solution. The addition of citrate dramatically changed the color from yellow to a dark red wine color as shown in **Figure 3.5**. This was followed by reflux for 60 min. After reflux the mixture was allowed to cool to RT and was stirred overnight. Then it was filtered through a 0.45 μm Millipore filter. Note that it is better to dilute the $HAuCl_4$ solution from a high concentration stock rather than weighing the powder each time because it is hygroscopic.

The synthesized GNPs was analyzed using UV-vis analysis. The size and concentration of the GNPs were estimated based on literature values [103]. Furthermore, the size of the particle was measured using the differential centrifugal sedimentation method (DCS) (DC24000, CPS Instruments Inc.) and TEM. From UV-vis analysis, the size of GNPs can be estimated based on the ratio of the absorbance of GNPs between the highest value and absorbance at 450 nm (A_{450}). And the concentration is estimated from the extinction coefficient of the estimated size of the GNPs at 450 nm ε_{450}. i.e. Concentration of GNP = $A_{450}/\varepsilon_{450}$. [103]. DCS is conducted at a speed of 24000 rpm and in a 9 step sucrose density gradient (8-24 %), with a kind support of Adam M. Davidson.

This technique was previously used to distinguish the different lengths of PEG-alkane thiols [102].

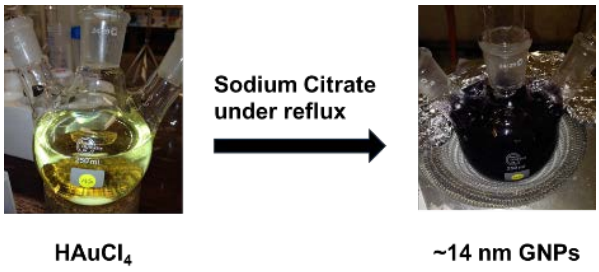

Figure 3.5. GNPs synthesis with Turkevich –Frens method.

3.2.2. Design of PS-modified DNA Minicircles

The sequence I used in this thesis is illustrated in **Figure 3.6**, and each ssDNA in **Table 2** was purchased from Eurofins Genomics GmbH (former Operon biotechnologies). PS modification in Circle 1_1PS was decided so that the PS modifications point outwards (part of the major groove of the A-tract) based on the literature [104]. The other two modifications are placed so that the three PS are located equidistantly (56 bp or 1/3 of 168 bp). The phosphate modification at the 5′ end in **Table 2** is for forming a phosphodiester bond to allow ligation to form closed circular DNA in the ligation step. 3 PS-DNA in the table is used as a control experiment.

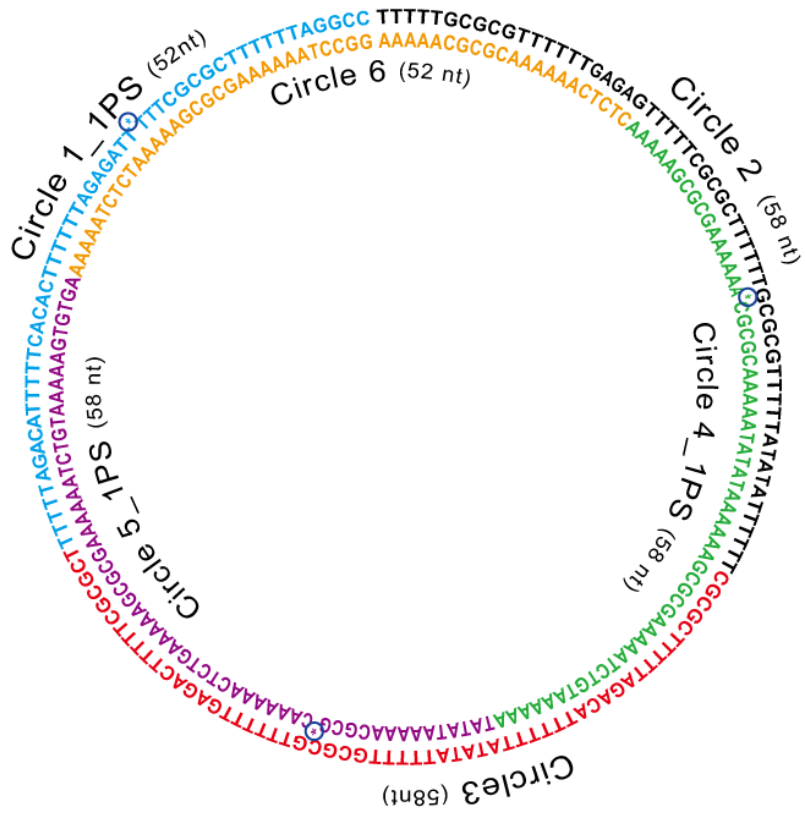

Figure 3.6. Sequence of DNA-MC (168 bp)
Different color of sequence represents different ssDNA. Three "*" inside blue circles in represent the locations of phosphorothioate modifications.

Table 2. Sequences of ssDNAs used for synthesis of DNA Minicircles

ssDNA	5′ [Phosphate] → 3′ (Phosphorothioate modification:*)
CIRCLE 1_1PS	TTTTTAGACATTTTTCACACTTTTTTAGAGATT*TTTCGCGCTTTTTTAGGCC
CIRCLE 2	TTTTTGCGCGTTTTTTGAGAGTTTTTCGCGCTTTTTTGCGCGTTTTTATATATTTTTTT
CIRCLE 3	CGCGCTTTTTTAGACATTTTTTTATATATTTTTTGCGCGTTTTTTGAGACTTTTTCGCGCT
CIRCLE 4_1PS	AAAAAATGTCTAAAAAGCGCGAAAAAATATATAAAAACGCGC*AAAAAAGCGCGAAAAA
CIRCLE 5_1PS	AGTGTGAAAAATGTCTAAAAAAGCGCGAAAAAGTCTCAAAAAAC*GCGCAAAAATATAT
CIRCLE 6	CTCTCAAAAAACGCGCAAAAAGGCCTAAAAAAGCGCGAAAAATCTCTAAAAA
3 PS-DNA	
CIRCLE 2_3PS	TT*TTTGCGCGTTTTTTGAGAGTT*TTTCGCGCTTTTTTGCGCGTT*TTTATATATTTTTTT
CIRCLE 3_3PS	CGCGCTT*TTTAGACATTTTTTTATATATT*TTTGCGCGTTTTTTGAGACTT*TTTCGCGCT

3.2.3. Synthesis of BIDBE

I followed the literature [97] for synthesizing BIDBE. 0.018 M of cystamine dihydrochloride (MW = 225.20), which was dissolved in 1 mL of 0.1 N NaOH was mixed with 0.22 M of iodoacetic anhydride (MW=353.88), which was dissolved in 0.25 mL of 1,2-dichloroethane (DCA)[29] (or in dichloromethane, DCM) in a 1.5 mL Eppendorf tube. After mixing, the tube was agitated on a vortex mixer for 1 min. The resulting white product was precipitated via centrifugation 12,000 g, 15 min at 20 ℃. Supernatant was discarded and dried in vacuo (centrifugal evaporator). This crude product was dissolved in acetone (0.5 ml), and centrifuged 12,000 g, 15 min at 15 ℃. The supernatant, containing BIDBE was transferred into a new Eppendorf tube (weighed beforehand). The white pellet, which did not dissolve consisted largely of by-product, iodoacetate. The acetone was evaporated completely under a stream of N2/Ar gas. During the reaction and after the synthesis, light was avoided to prevent degradation. The synthesis scheme is illustrated in **Figure 3.7**.

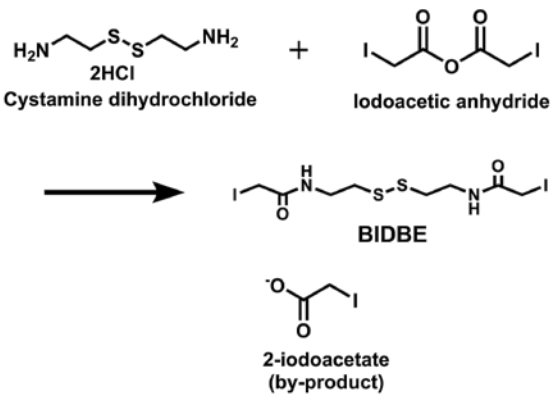

Figure 3.7. BIDBE synthesis
See the text for details.

[29] Pipetting was done with glass pipet.

3.2.4. Attachment of BIDBE and GNPs to PS-DNA

Step I. Synthesis of DNA-MCs

This is the summary of the method used in the literature [104]. BIDBE-attached PS DNA (100 pmol) and other oligonucleotides (200 pmol) were mixed in TAE-Mg^{2+} Buffer (20mM Tris, adjust pH = 7.4 with acetic acid, 1.25 mM EDTA, 6.25 mM $MgCl_2$), 88 µl in total. The mixture was heated at 94 ℃ for 30 seconds and cooled down slowly by turning off the PCR machine for ~45 min. Alternatively, the sample in a tightly closed Eppendorf tube was put in to stirring boiled water ~ 800 mL, and left to cool to room temperature. After cooling, 10 µl of ligase buffer and 2 µl of T4 DNA ligase (400 Unit/µl)[30] from New England BioLabs Inc. were added and solution was incubated at 16 ℃ for 10 hours. 50 µl of BAL-31 2x buffer and 3 µl of BAL-31 exonuclease (1U/µl) from New England BioLabs Inc.[31] were added and incubated for 2 hours at 30 ℃. Sample was purified again using a PCR purification kit (QIAGEN).

Step II. Attaching BIDBE linker to PS-DNA

I followed the literature [96] for attaching BIDBE onto single stranded DNA (ssDNA) or onto DNA-MC. 0.5 nano mol of PS-DNA was dissolved in 50-60 µl of 10 mM sodium phosphate pH 7. 2 µl of 50mM BIDBE (100 nano mol), which was dissolved in DMF (Dimethyl sulfoxide), was added to this 1-PS-DNA. The amount of BIDBE was increased to keep the molar ratio of phosphorothioate : BIDBE = 1 : 200. The mixture was incubated at 50 ℃ for 5-6 h in the dark. The product was purified using a Zeba Micro Spin Desalting Column (Thermo Scientific) against pure (Milli-Q) water and kept at -

[30] 1 Unit = 50 % of 20 µl of 0.12 µM λ DNA is ligated after incubating 16 ℃ for 30 min.

[31] 1 Unit = remove 200 base pairs DNA (40ng/ul) if incubate 10 min at 30 ℃.

20 ℃ until used for attaching GNPs. Concentration and purity was measured with a NanoDrop spectrophotometer (single stranded DNA mode or UV-vis mode).

3.2.5. Reaction of GNPs with DNA

BIDBE on the PS-DNA was reduced via 1 mM TCEP for 1 hour in 0.5 mM acetate buffer (pH5.2). After reduction, to remove all free BIDBE and free BFs, sample was purified twice with the same Zeba Column. After reduction, this BF formed DNA was reacted with the following different conditions to achieve the optimum reaction with GNPs.

Optimum ratio of PEG against GNPs

Both PEG-alkane thiols and PS-DNA form S-Au bonds, therefore, once GNPs are fully covered with PEG, PS-DNA cannot access them. Therefore, it is important to not cover 100 % of the GNPs surface with PEG molecules to leave a space for PS-DNA to attach, while the amount of PEG is still sufficiently high enough to stabilize the GNPs. Therefore the optimum ratio of GNPs and PEG molecules was studied.

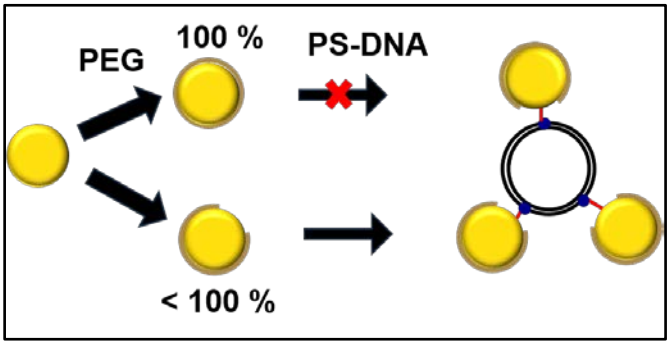

Figure 3.8. Schematic image of coverage of PEG ligands on GNPs
In reality, the PEG molecules are supposed to homogeneously distribute on the GNPs, but for the convenience, the figure is drawn as if the GNPs are localized.

Step III. Attachment of GNPs onto DNA-MCs

Since DNA and GNPs have negative charge (especially for citrate or BSPP coatings), it is difficult to attach GNPs onto DNA. The standard method to avoid this problem is to increasing NaCl concentration after incubating GNPs with DNA [46, 96]. The salt neutralizes the charge around GNPs and the thiol group of the DNA attach to GNPs. However, if the ratio of DNA is small compared to GNPs, GNPs tends to aggregate by addition of salt from my experience. In my thesis, to prevent irregular aggregation, GNPs and PS-DNS should be 1 **:** 1. Therefore, PEG molecules are required to stabilize the GNPs and the ratio between PEG molecule and PS-DNA is important. Based on the optimum ratio to stabilize GNPs, the ratio of PS-DNA and PEG were also studied.

3.3. Results

3.3.1. GNP synthesis

From UV-vis analysis the size of the GNPs was estimated to be around 14 nm and the concentration was estimated to be around 7 nM from the estimated extinction coefficient (ε). From DSC analysis the GNPs were estimated to be around 12 nm (**Figure 3.9**). From TEM analysis the average size of the particle was 14 nm (**Figure 3.10**). I estimated that the synthesized GNPs was 14 nm for this thesis.

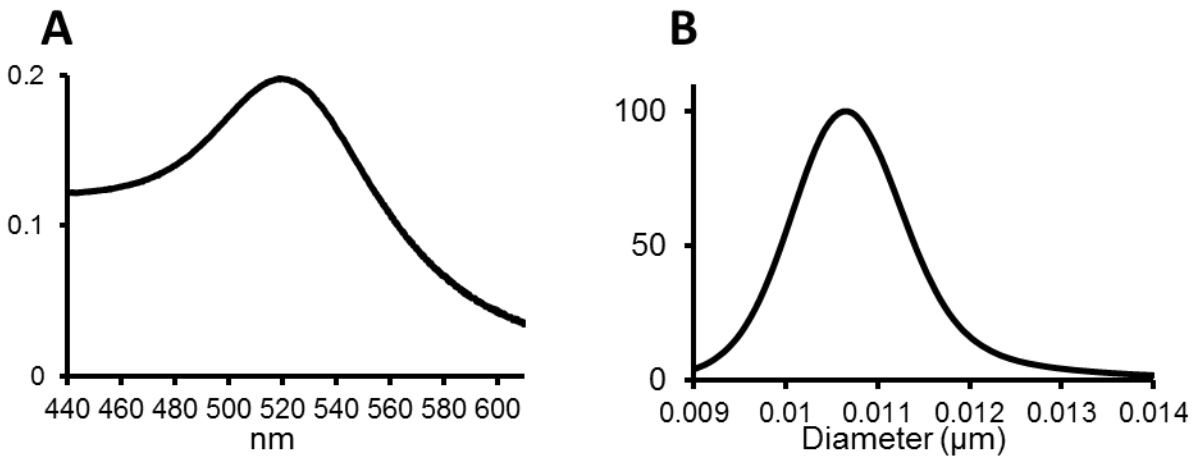

Figure 3.9. UV-vis analysis and DSC analysis
UV-vis analysis (**A**) and DSC analysis (**B**) of GNPs. Peak of the UV-vis was 520 nm and A_{450}/A_{520} was 1.6. DSC results showed weighted mean diameter was11.7 nm ±2.9 (SD).

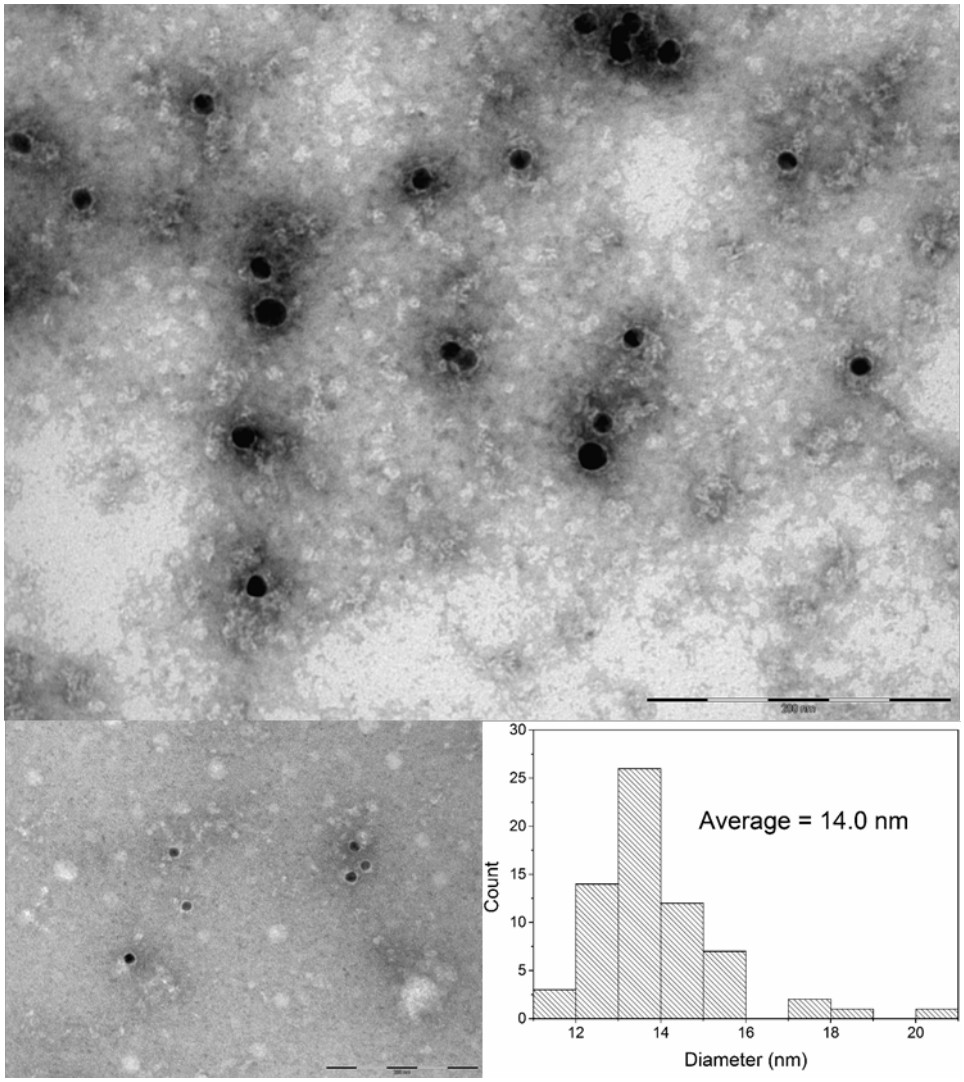

Figure 3.10. TEM image of GNPs and histogram of the particle size
Two TEM images were taken at the same magnification (scale bar = 200 nm) Since this sample was incubated with TRAP-K35C, a protein "corona" was formed around GNPs (no TRAP-cage structures as seen in **Chapter 2**). From several TEM images, histogram shows particle size (n=33).

3.3.2. GNPs stabilization with PEG

To find the optimum concentration of PEG to stabilize GNPs, while allowing other molecules to attach, several series of PEG concentrations were mixed with GNPs. The estimated number of gold atoms on the surface of a 14 nm GNP is ~2,050. Therefore, this "2050 times" of the concentration of GNPs is considered here as "1x". By assuming

that GNPs are 14 nm spheres, the surface area of a GNP is 615 nm^2. Therefore, "1x" is equal to 3.3 PEG/nm^2. In the common case where stabilizing GNPs with PEG-alkane thiols, "10x" of the PEG molecules are used. **Figure 3.11** shows that approximately 1 x or more of PEG molecules are necessary to stabilize GNPs. Originally the GNPs were red but when as they start to aggregate the color becomes blue, therefore the stabilized GNPs are red. However, after adding 100 mM of NaCl it was determined that 1 x of PEG molecules was not sufficient. From this experiment between 1x and 2 x of PEG molecules should be the optimum concentration (enough to stabilize GNPs but room for PS-DNA to attach).

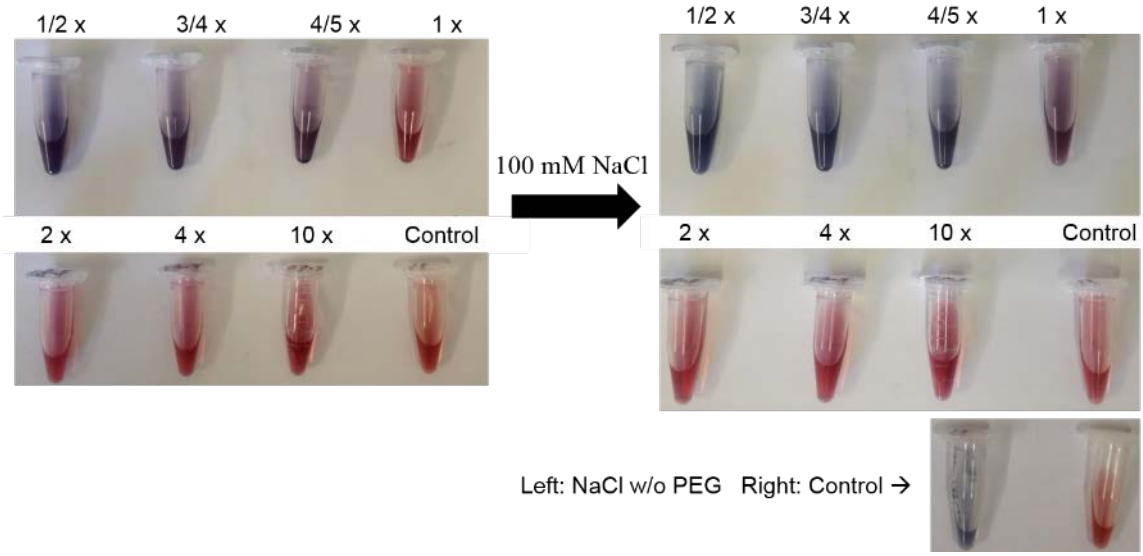

Figure 3.11. GNPs with PEG and the addition of NaCl
The two left panels show the different concentrations of PEG molecules added to GNPs. The two panels on the right show the same tubes after the addition of NaCl. The control tube did not have any additions of PEG molecules or NaCl, but it is known that the addition of NaCl makes a blue color the same as 1/2 x of PEG molecules.

Additional analysis of PEG precipitation

Since PEG molecules were expected to stabilize GNPs, but not cause precipitattion, the effect of the amount of PEG molecules for GNPs was further analyzed. I confirmed this phenomenon in stirring conditions. First I added 1/3 x of PEG and then after 20 minutes the color slightly changed. Then I added 1/6 x of PEG to make the final 1/2 x concentration. By comparing with the control I noticed it was a slightly different color. Over time, the color continued to darken in comparison with the control. Even after adding 1/10 x of PEG to the final 3/5 x concentration the color didn't change. However the addition of PEG molecules to make the final 10 x concentration brought back a reddish color as seen below. Note that compared to the previous experiment in the Eppendorf tube, this stirred dark blue mixture did not form precipitation even after stirring ceased.

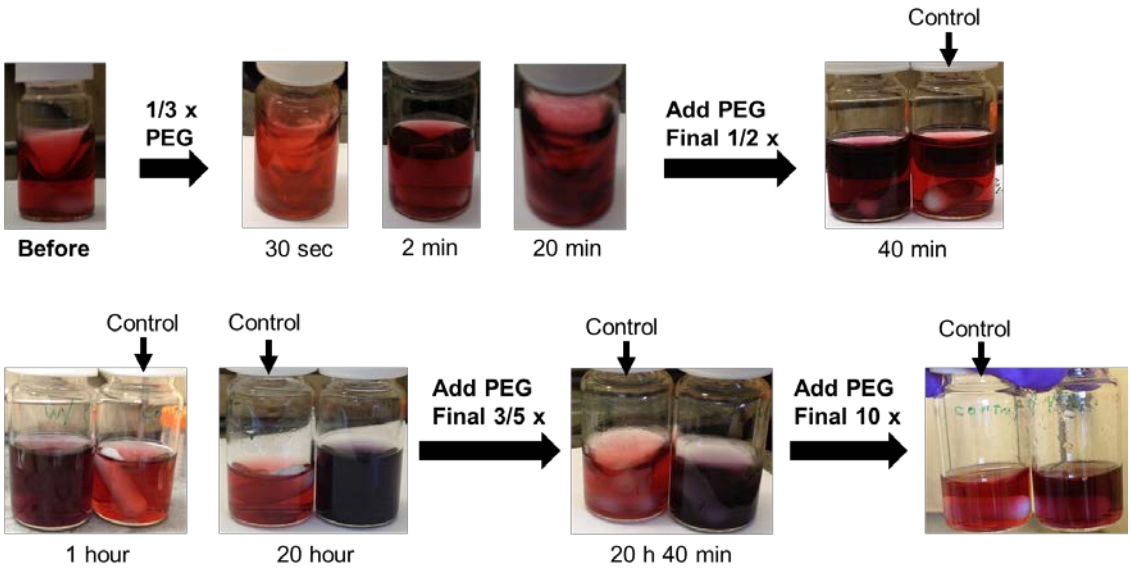

Figure 3.12. Time course of color change of GNPs depending on the concentration of PEG molecules in the solution.
By comparing with control (w/o PEG), the color change (= aggregation of GNPs) was easily recognized. Between times, the slight color changes were difficult to compare, sometimes because the light condition was not the same.

The UV-vis and Zeta potential of the control, 1/2 x PEG and 10 x PEG were measured as seen below. The control and 10 x PEG had similar absorbance from UV-vis spectrometry but 1/2 x PEG has a different spectrum from the others as expected. However, from Zeta potential, all of the solutions had a negative charge which was surprising because I expected the aggregated solution to have charge closer to neutral.

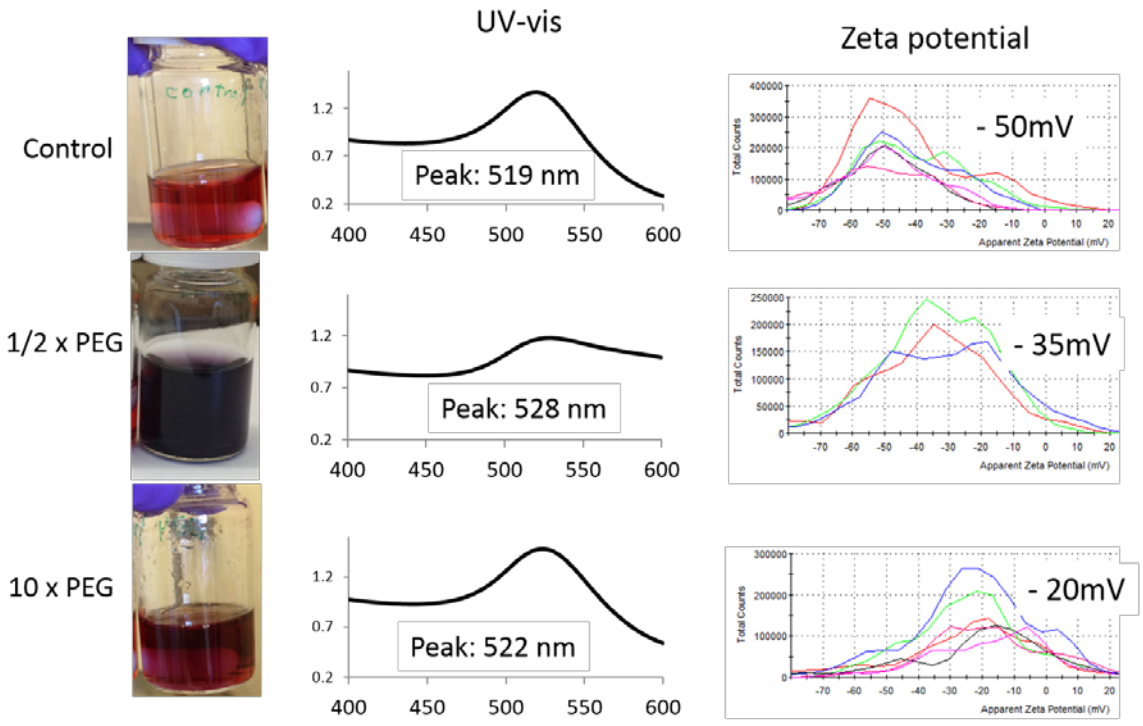

Figure 3.13. UV-vis and Zeta potential analysis of aggregated GNPs with PEG
UV-vis analysis and Zeta potential results shown alongside the actual solution. The peak is indicated in each figure

3.3.3. Synthesis and analysis of BIDBE

The BIDBE (MW= 488.15) was synthesized with a yield of approximately 78 % (6.4 mg, 13 µmol). The purity of synthesized BIDBE was confirmed with micromass LCT mass spectrometry. From the spectra, there was a major peak of 510.8, expected to be be $[BIDBE + Na]^+$ (theoretically 511.1). Other small peaks at 488.9, 511.9, 526.8 should be $[BIDBE + H]^+$, $[BIDBE + Na]^+$ (with isotopes e.g. C^{13}), $[BIDBE + K]^+$.

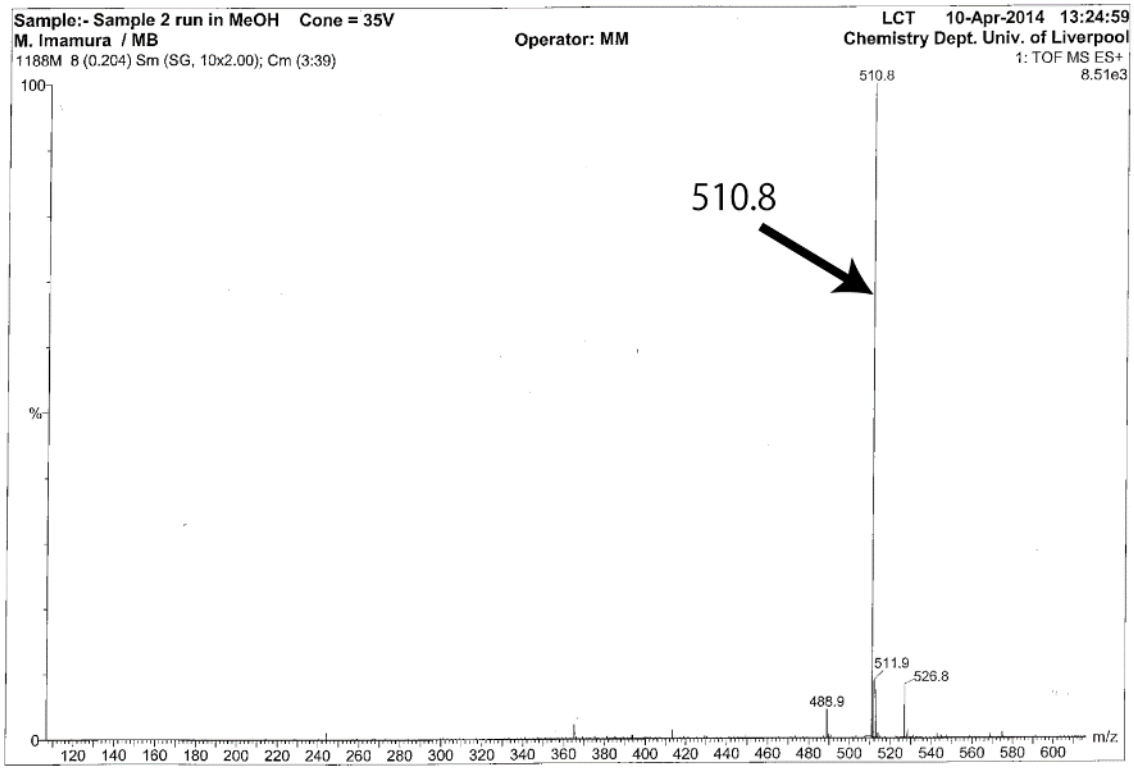

Figure 3.14. Micromass LCT Mass spectrometry results of BIDBE synthesis
Electron spray ionization mode, and BIDBE was dissolved in Methanol. This measurement was done by Moya McCarron, Department of Chemistry Mass Spectrometry Service, University of Liverpool, UK

3.3.4. Synthesis of DNA-MC

Electrophoresis of DNA-MC

After the synthesis of DNA-MC, the formation was first confirmed with electrophoresis. On the acrylamide gel, DNA-MC migrated very slowly.

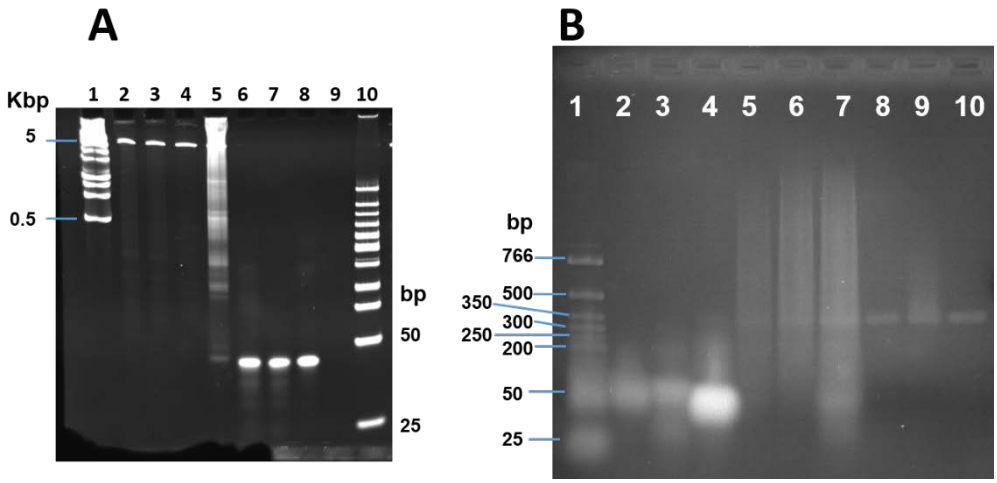

Figure 3.15. Polyacrylamide gel and agarose gel electrophoresis of DNA-MC
(**A**) Polyacrylamide gel (10%) and (**B**) agarose gel (2 %) electrophoresis. (**A**) Electrophoresis was carried out at 180 V, 14 mA for 47 min. Lane 1: 1kb DNA ladder (NEB); 2-4: DNA-MC (different number of PS-modifications, but identical length, 168 bp); 5: after ligation reaction, but before exonuclease treatment and purification; 6-8: ssDNAs with different numbers of PS-modifications, but identical length (52 bases) and 10: Low MW (LMW) DNA ladder (NEB). (**B**) Electrophoresis carried out at 100 V for 60 min. Lane 1: LMW DNA ladder (NEB); 2: ssDNA (Circle 1 of DNA-MC); 3: ssDNA (Circle 2 of DNA-MC); 4: dsDNA (Circle 1 and its complementary strand); 5-7: Before digesting with exonuclease (after purified with PCR purification kit; samples in lanes 6 and 7 were purified from the flow through of the sample in lane 5); and 8-10: DNA-MC (the sample in 9 is purified from flow through of the column purified sample in 8; lane 9 is digested with exonuclease and purified from the sample in lane 6).

Atomic force microscope (AFM) of DNA-MCs

To confirm that the DNA-MC was actually formed, AFM was used. From the results the DNA-MC were approx. 20 nm in diameter, which is the same as estimated judging from the length of the DNA (168 bp). The AFM image was taken as described in the literature [104] TAE-Mg^{2+} buffer (40 mM Tris acetic acid pH 7.4, 2.5 mM EDTA,

12.5 mM $MgCl_2$). Polyornithin was pre-incubated on the fleshly cleaved mica, and the DNA-MCs in TAE-Mg^{2+} buffer was observed in aqueous tapping mode.

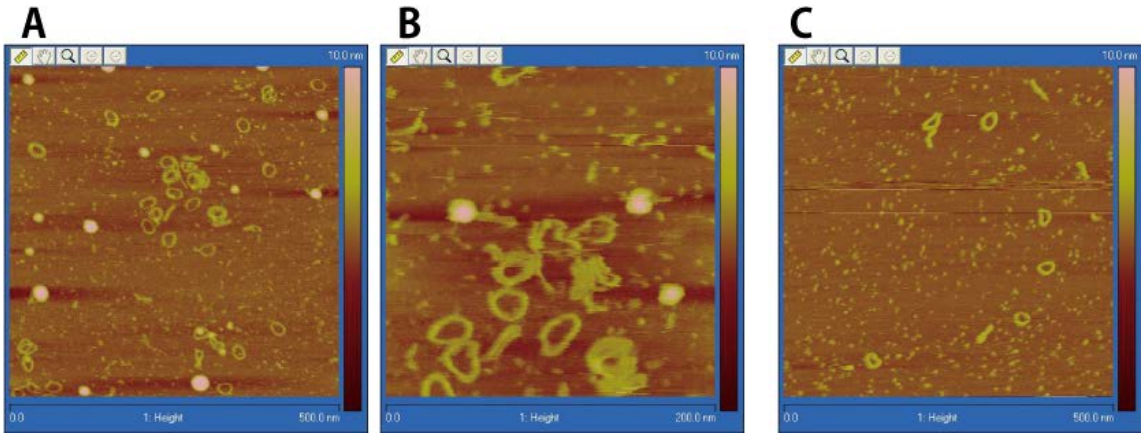

Figure 3.16. AFM image of DNA Minicircles
(**A**) and (**B**) are the sample seen in lane 2 of **Figure 3.15 A**. (**C**) is further purified sample by cutting the band from the same lane 2. (**A**) and (**C**) are 500 nm x 500 nm, and the (**B**) is 200 nm x 200 nm. The AFM image was taken by Dr. Koji Sumitomo, NTT Basic Research Laboratories, Kanagawa, Japan.

3.3.5. Attachment of GNPs onto DNA

Electrophoresis

GNPs, GNPs with PEG molecules, ssDNA, DNA-MC, and DNA with GNPs from different preparation methods were run together in agarose gel electrophoresis **Figure 3.17**. The migration of each sample was different. Remarkably, GNPs with PEG molecules migrated towards the cathode. That means that PEG molecules are positively charged which the opposite result from the Zeta potential results mentioned in **Figure 3.13**. However, this result is more convincing based on the idea that small concentrations of PEG molecules are close to neutral while large concentrations are not. Note that PEG molecules are supposed to be neutral Due to –OH group at the end. Among the bands, lane 9 migrated uniquely, also, only in lane 19, both the band of GNPs (dark band) and DNA (close to the well) exist in the same lane.

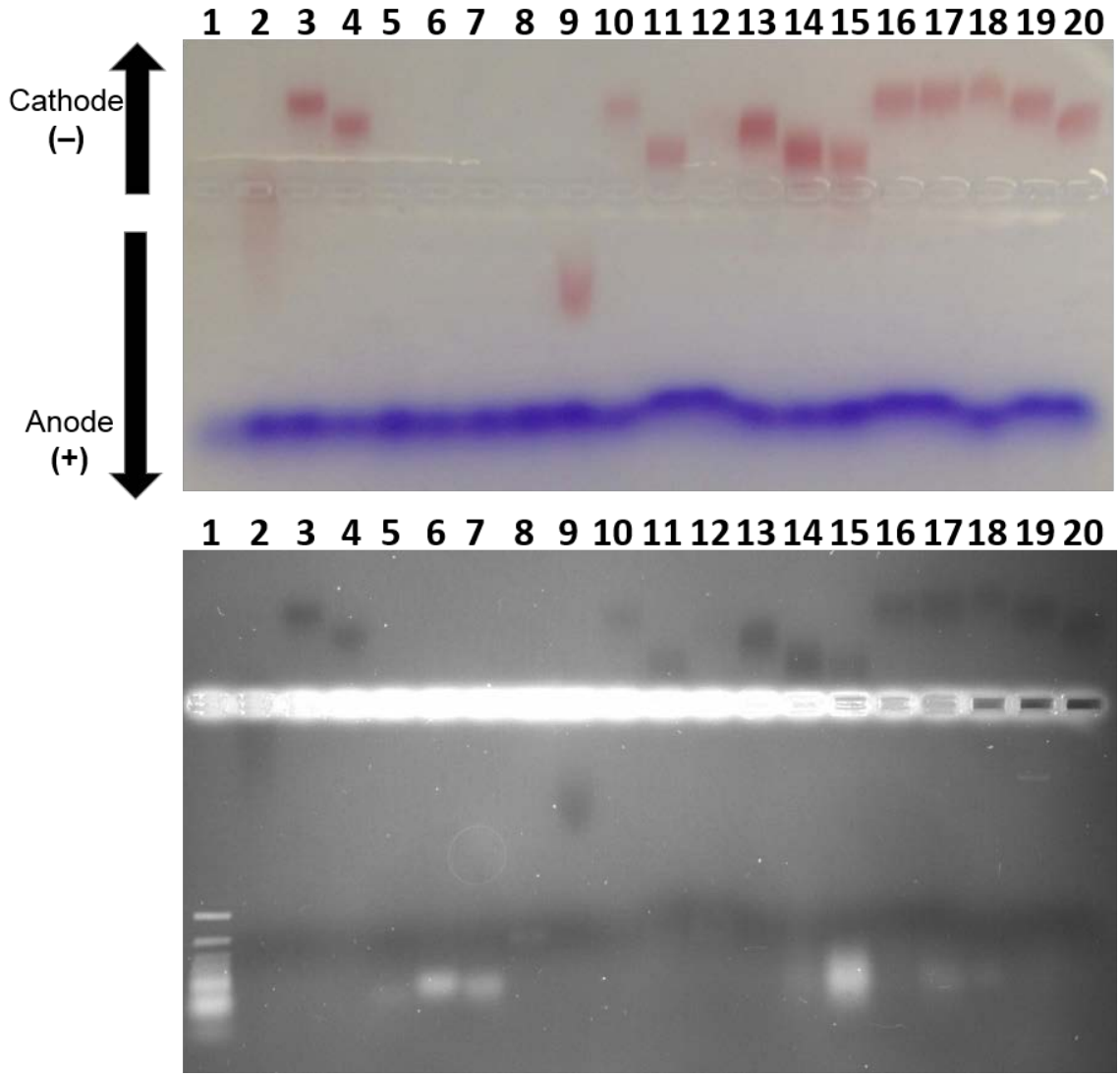

Figure 3.17. Agarose gel (1%) electrophoresis with visible light (Top) and viewed under UV lamp after staining with ethidium bromide (Bottom).

lane	Sample	lane	Sample
1	LMW DNA ladder	11	GNP with PEG 2x →DNA-MC
2	GNPs	12	DNA-MC **:** PEG = 1 **:** 2000, mixed with GNPs
3	GNPs with 10x PEG	13	2x (Circle 1_1PS and Circle 6 mix) + GNPs + 1.5x PEG withogut NaCl
4	GNPs with 1.5x PEG	14	10x (Circle 1_1PS and Circle 6 mix) + GNPs + 1.5x PEG withogut NaCl
5	ssDNA (Circle 1-1PS) (100 ng)	15	100x (Circle 1_1PS and Circle 6 mix) + GNPs + 1.5x PEG withogut NaCl
6	ssDNA (Circle 2-3PS)	16	10x Circle 1_1PS + GNPs
7	Circle 1-1PS and Circle 6 mix (100 ng)	17	100x Circle 1_1PS + GNPs
8	DNA-MC (25 ng)	18	Circle 2_3PS **:** GNPs = 1 **:** 200
9	DNA-MC + GNPs +1.5x PEG mix	19	Circle 2_3PS **:** GNPs = 1 **:** 2000
10	DNA-MC **+** GNPs mix → + 10x PEG	20	GNP + PEG 2x → Circle 2_3PS

3.3.6. SEM

Firstly, a scanning electron microscope (SEM), FEI QUANTA, FEG 250 was used to see if GNPs arrayed on DNA-MCs. Sample was viewed under SEM in vacuum conditions which was supported by Dr. Casper Kunstamann-Oslen. There were some expected triangular arrangements of GNPs (circled in yellow below), but the majority was composed of larger aggregates. This could be because the sample was dried in order to observe under SEM. From control samples, GNPs attached onto PS-modified ssDNA or onto PEG molecules, there were still some stochastic triangular arrangements and the ratio of triangular arrangements from DNA-MC with GNPs was not significantly high compared to those of the control, therefore, from this SEM images it was difficult to conclude that GNPs were arranged in a triangular fashion on the DNA-MCs.

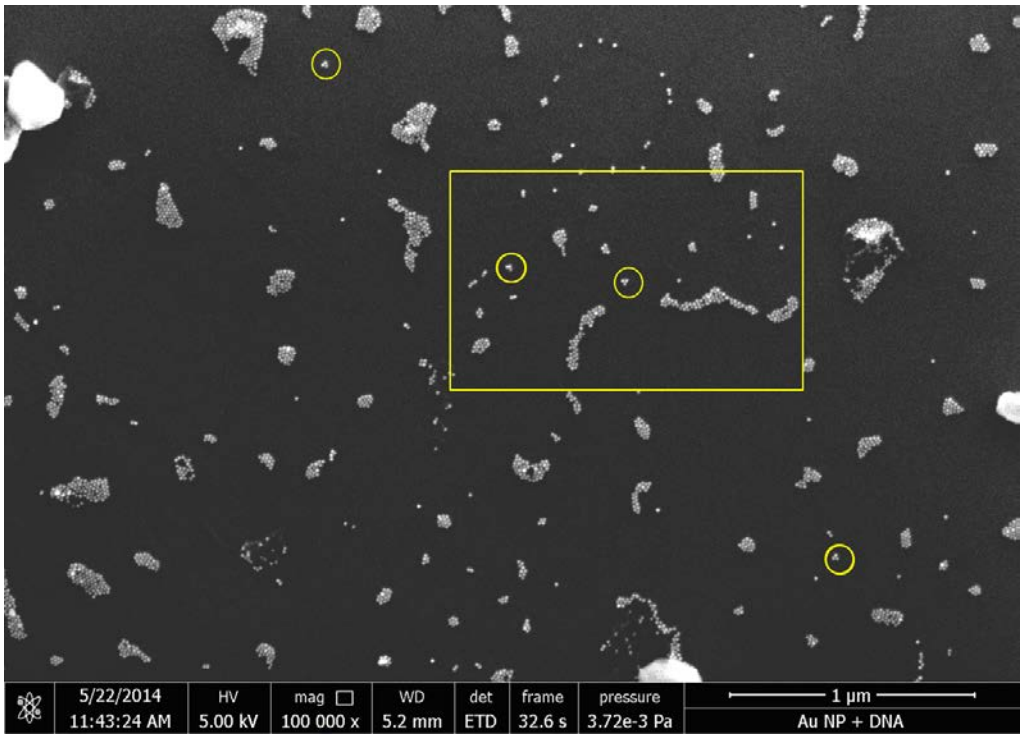

Figure 3.18. Large area of SEM image of DNA-MC with GNPs.
The GNPs with triangular arrangement were circled in yellow.

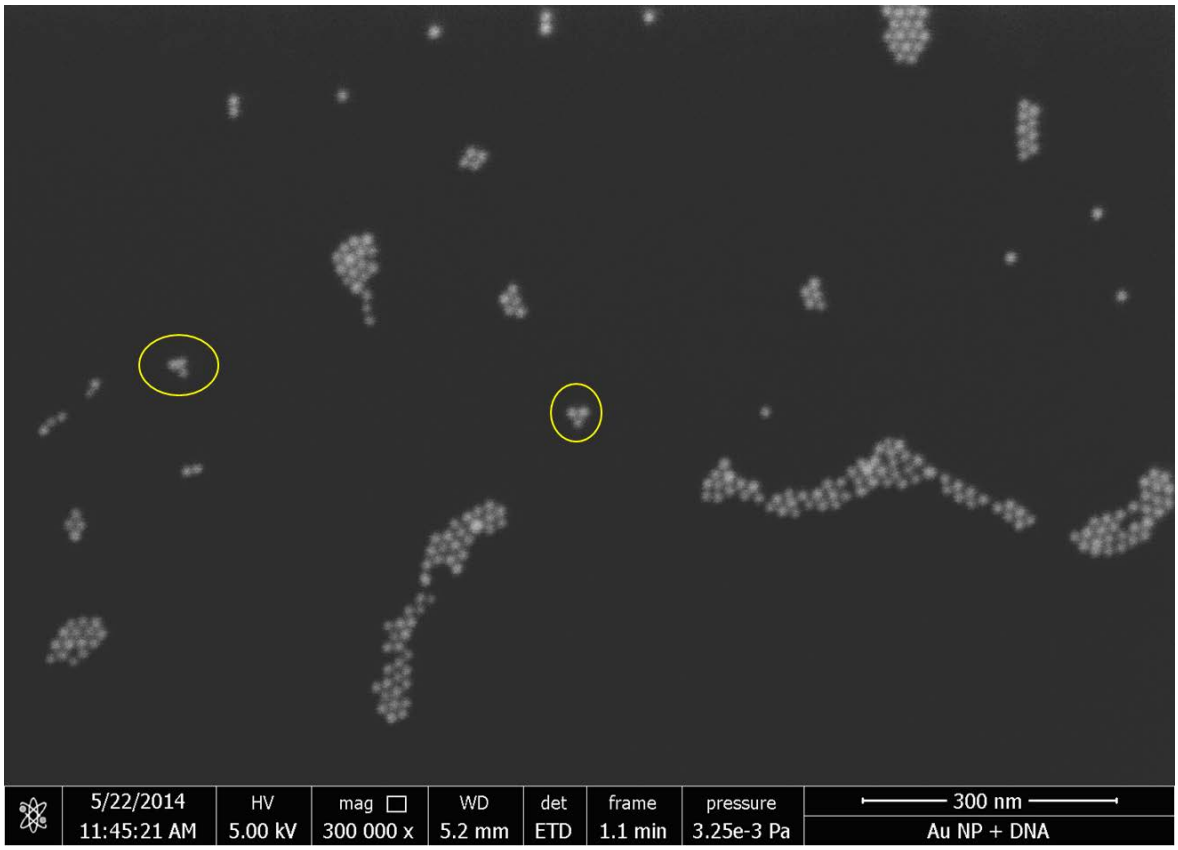

Figure 3.19. Enlarged image of the area within the yellow box in the previous figure

.

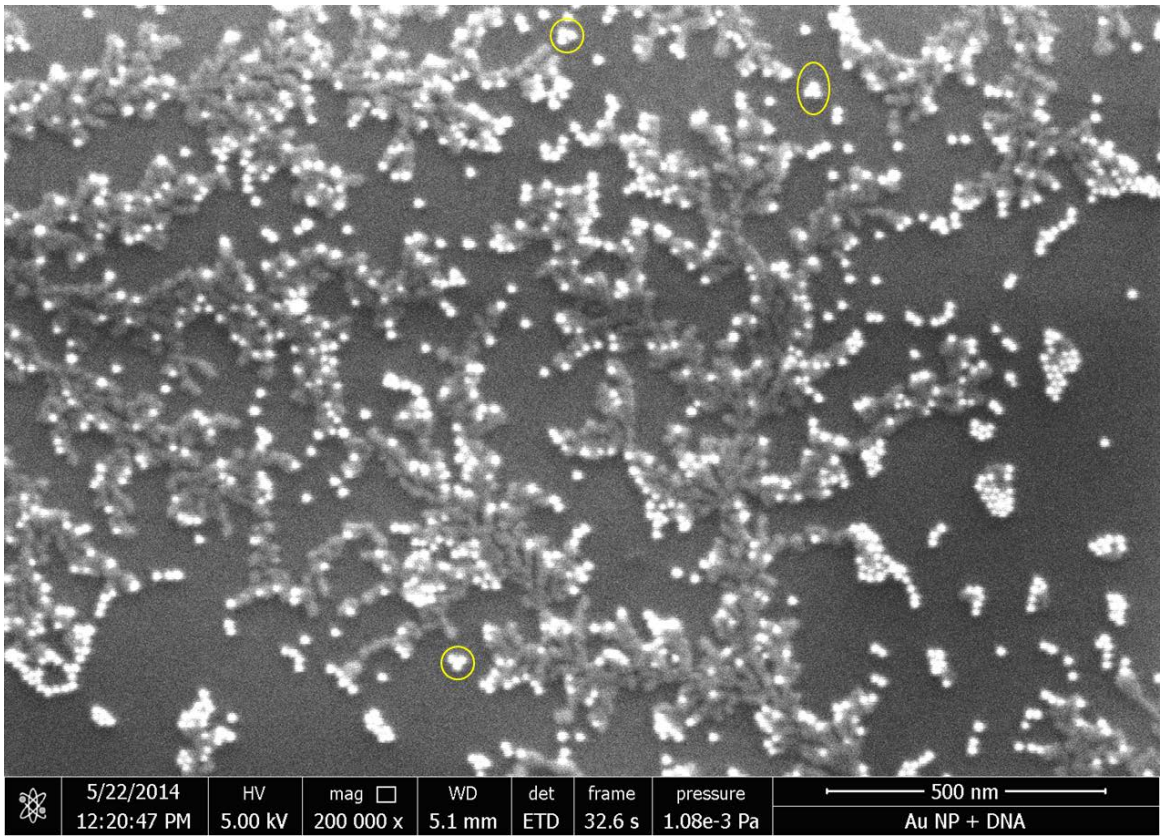

Figure 3.20. ssDNA with GNPs.
Triangular arrangements are circled in yellow.

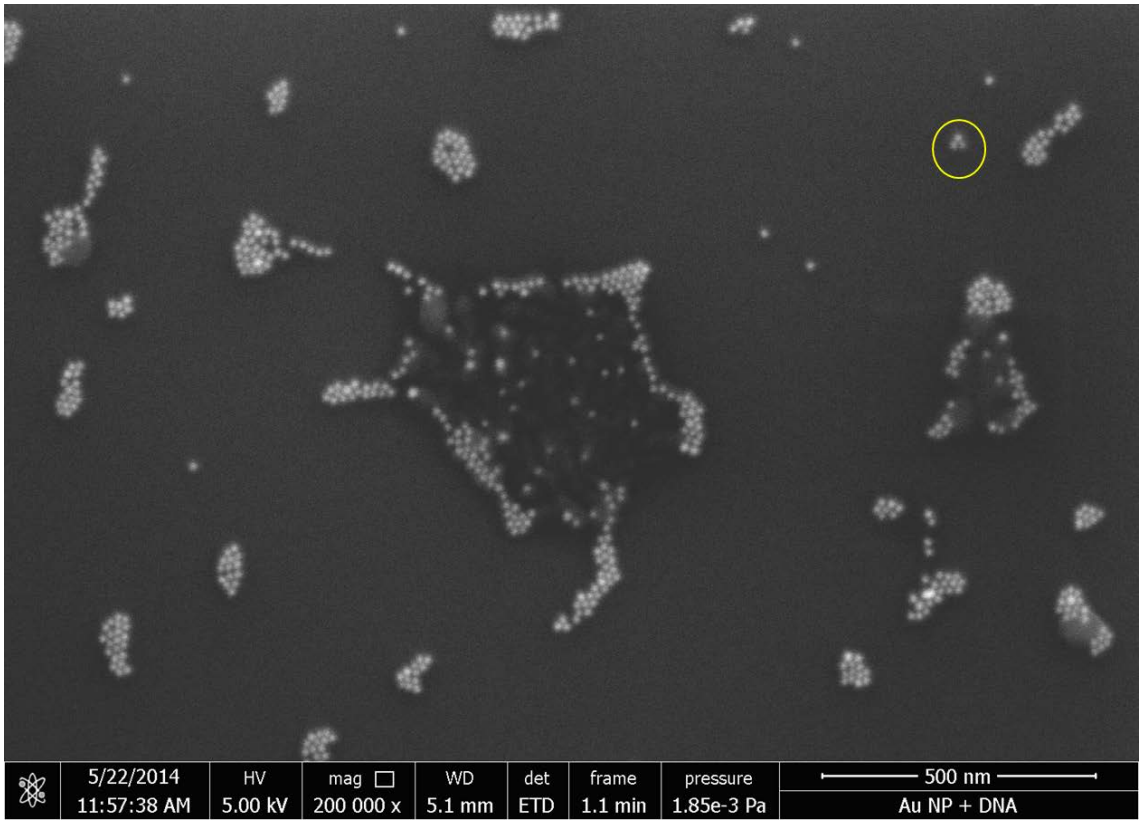

Figure 3.21. GNPs with PEG molecules.
The triangular forms have been circled in yellow.

Environmental SEM

Since it was difficult to evaluate in dry conditions, DNA-MCs with GNPs from lane 9 in **Figure 3.17** were evaluated under humid conditions, so called environmental SEM (ESEM) with the help of Dr. Domagoj Belić. It was very difficult to view such small nanoparticles and it was also difficult to find the optimum observation conditions using this technique. Especially, the target objects were moving while under observation, and background noise became high at high magnification, making it very difficult to view nm scale structures. However, one triangular arrangement of GNPs was found from the limited images.

Figure 3.22. Wide area of humid environmental SEM image.
Triangular arrangement of GNPs are circled with the small yellow circle and the big circle shows unknown circular structures.

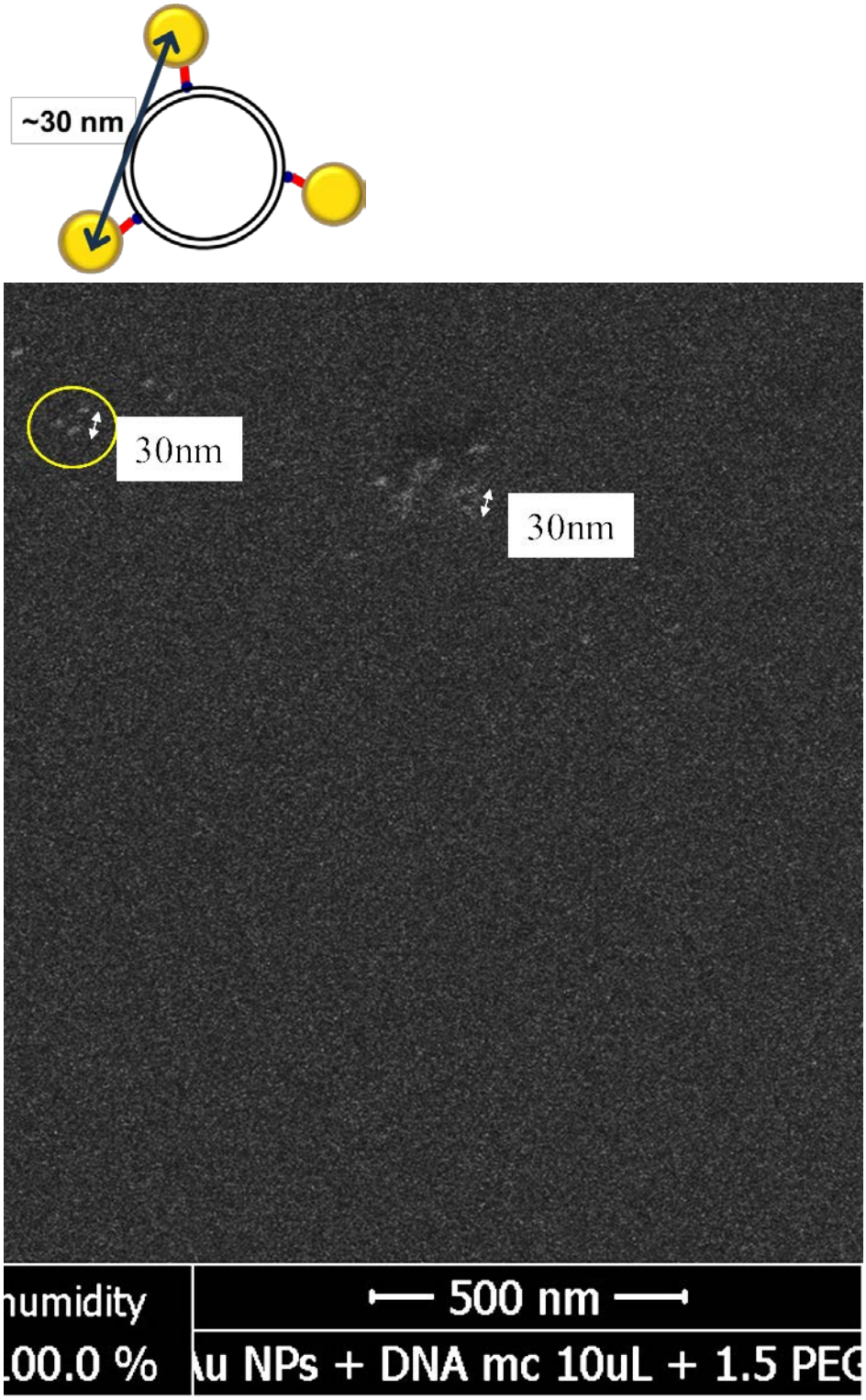

Figure 3.23. Enlarged image of previous image.
The yellow circle shows three GNPs were arranged approx. 30 nm equidistant.

Since the humid condition was very difficult to observe, semi-humid conditions (humidity is slightly less than 100 %, but the pressure was the same as ESEM) was tried, where there were still small droplets of water on the silicone surface. In the semi humid conditions, there was a higher ratio of triangularly arranged GNPs. However the ratio of triangular arrangement was too low to conclude that triangular formation of GNPs was achieved. This requires more optimization of reaction conditions and further purification.

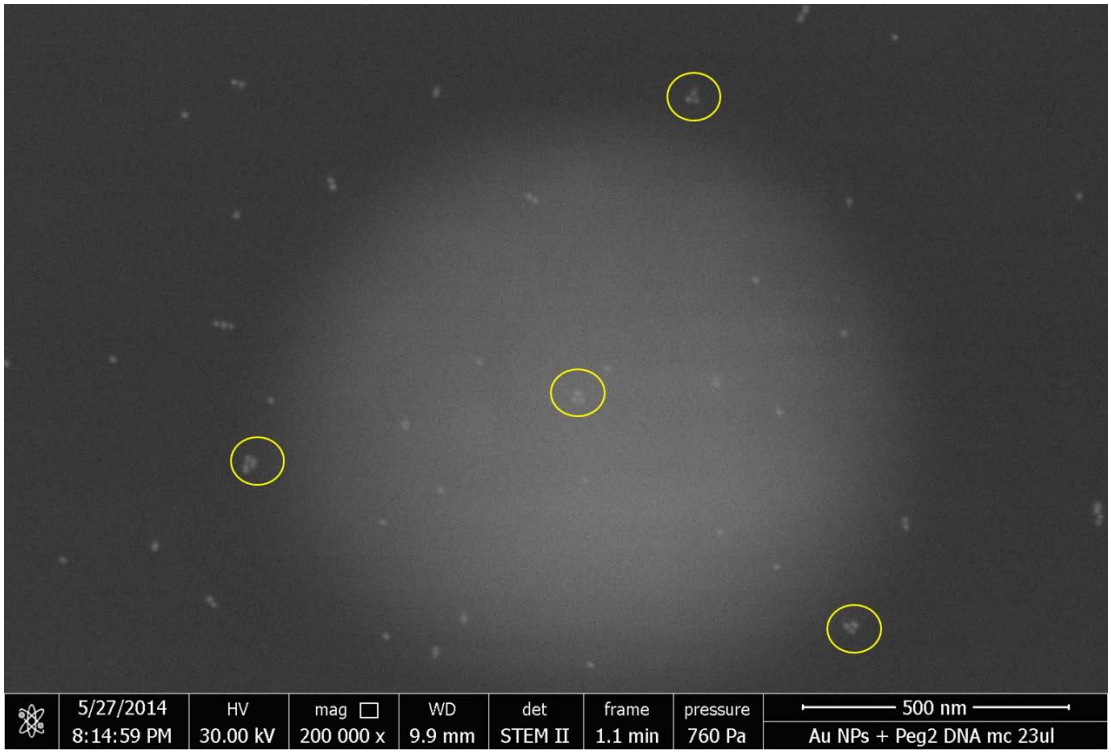

Figure 3.24. Semi-dry condition SEM image.
Water droplets is the blurred light gray spot and the GNPs with a triangular arrangement are circled in yellow. This image was viewed in STEM mode.

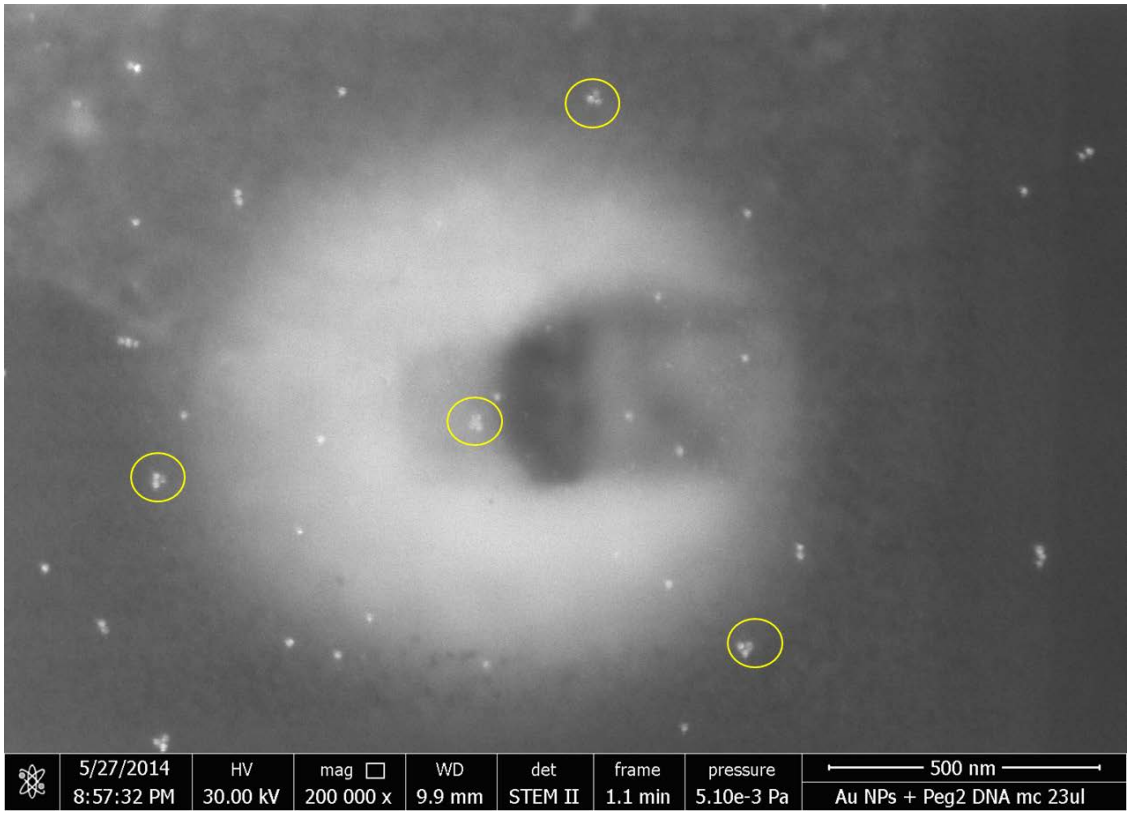

Figure 3.25. The same area as the previous image, but under vaccuum conditions. The large white spot is a dried water droplet.

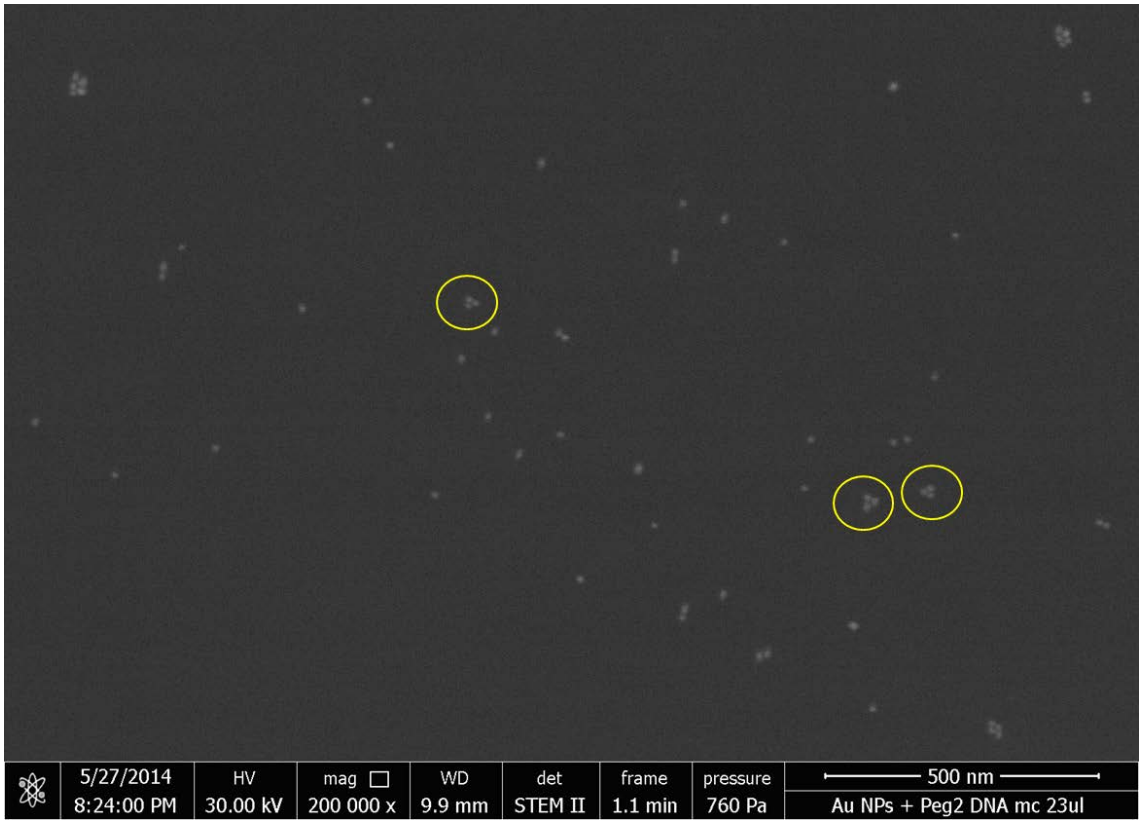

Figure 3.26. Another representative image of semi-dry condition SEM.

3.4. Summary

From electrophoresis analysis DNA-MC with GNPs migrated differently from other samples, however, from SEM analysis, it was not convincing that GNPs formed in a triangular shape around the DNA-MC. I expected three GNPs to attach to the outside of each DNA-MC, however, based on SEM images this might not be the case. This could be because the size of the DNA-MCs and the GNPs are similar and because DNA-MC could be flexible enough to attach one GNP onto all three PS-modifications. However, viewing many more images from different conditions are required to evaluate the yield of triangular arrangement of GNPs. As a side experiment, PEG-alkane thiols which were supposed to stabilize GNPs instead aggregated GNPs at small concentrations, probably due to the charge of the GNPs becoming neutral. Further addition of PEG molecules (~4100 times of the concentration of GNPs) seemed to make the GNPs become positively charged and stabilize the GNPs again.

Chapter 4

Conclusions and Perspectives

4.1. HS-AFM

HS-AFM was able to show dynamic transformation of protein structures. In particular, the ability to observe close to subunit resolution allowed insight into the mechanism of TRAP-cage formation and break-up process to be achieved. From the observation, a protein shuffling effect may be a key effect to allow the dramatic ring to sphere transformation to occur in a very regular manner. This shuffling effect, especially occurring in such a highly thermostable protein is unexpected. In this thesis, I used mainly HS-AFM techniques, and some of the phenomenon observed should be checked using other techniques. For example, this protein shuffling could be tested in a simple way as illustrated in **Figure 4.1**.

Another insight from HS-AFM was into the function of GNPs. Since the TRAP-cage formation occurs for both neutral and negatively charged GNPs, a catalytic activity of 1.4 nm GNPs to form disulfide bonds between cysteine could be involved. Much remains to be studies regarding the mechanism of GNPs catalysis. This particualr catalytic activity of small GNPs could be used as new approach for a bimolecular reactor, e.g. a column immobilizing these small GNPs could be a used as catalytic column for disulfide formation. To identify the catalytic activity, other methods such as Raman spectrometry is required to know the chemical reactions.

TRAP-cage has very unique characteristics; a “hollow” cage, “thermostable” and “degradable by reducing agent”. Although this originated as unexpected outcome from metamaterials research, understanding the detailed characteristics and mechanism of TRAP-cage formation will be useful for bionano science.

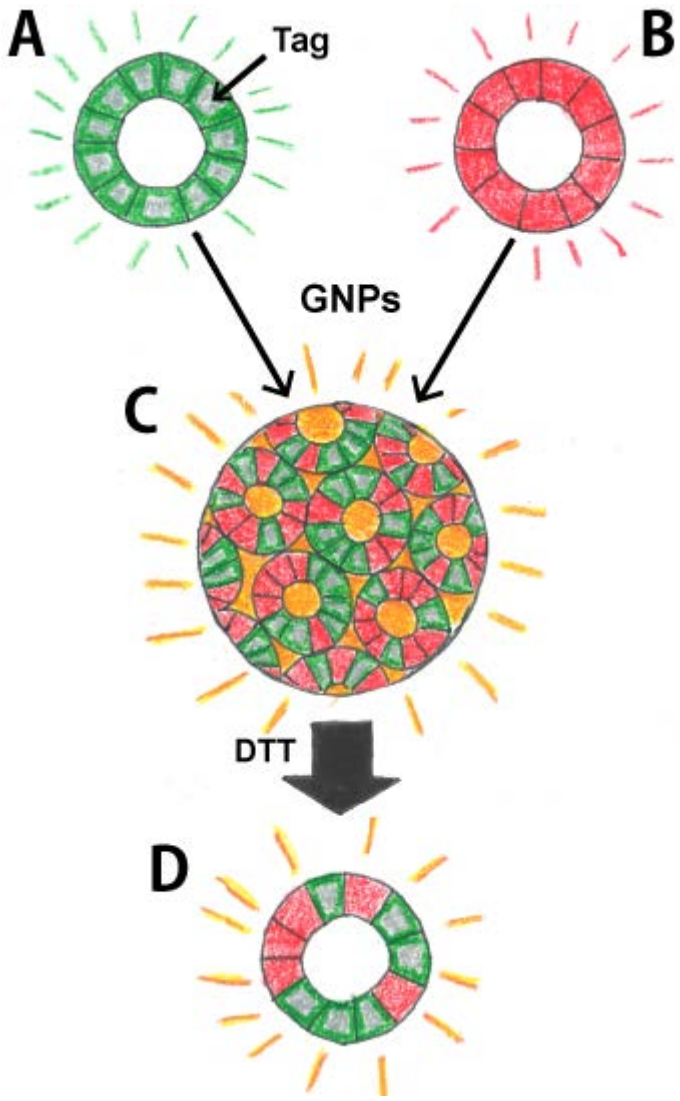

Figure 4.1 Proposal for a protein shuffling test with a system of two fluorophores and one tag
(**A**)TRAP-K35C with a green fluorophore possesses a tag for binding specific column, while red TRAP-K35C (**B**) doesn't. If the shuffling is occurring, the subunits in TRAP-cage (**C**) and the ring structures (**D**) after the addition of DTT, should be mixed. Therefore, subsequent purification of this mixed TRAP-K35C using the green specific tag should look yellow. This illustration was kindly drawn by Allison Imamura.

4.2. DNA-MC

Since the HS-AFM showed a clear image of the protein dynamics, many synthesis conditions of forming GNPs arrangement onto DNA-MCs should be observable. To

obtain a high yield of GNPs attachment to DNA-MCs, it is also better to consider attaching GNPs to ssDNA first and then synthesize the DNA-MCs from GNP- attached ssDNAs. However, the enzymes for ligation and exonuclease reaction would probably not work well when using ssDNA with GNPs attached to them. Also, a standard DNA purification column may be difficult to use because the property of GNPs attached DNA is different from DNA itself. In addition, high density salt precipitation methods could lead to irreversible precipitation. It is better to have more than 20 nm diameter GNPs in order to have a plasmonic effect, but DNA-MC is only 168 bp and 20 nm in diameter, therefore, DNA-MC may be too small to template 20 nm GNPs. Therefore, another robust and larger scaffold would probably be required. After figuring out the solution to these problems, GNPs could be increased around the DNA-MCs in order to obtain a strong metamaterial effect.

4.3. Final observations

Designing nanostructures from biomolecules is a promising field of research, however, outcomes can be difficult to predict in advance. Therefore, building nano structures from biomolecules is still challenging. However, the progress of science is so quick that to design and build reproducible biological nano devices may not be a dream for much longer. For example, in the early 2000s, when metamaterials were becoming very popular, little research was done at the nano scale (mostly micro or sub micro scale) [105]. But now, metamaterial units, which have been fabricated using similar methods as in this thesis, have already been reported [101, 106]. Although in these cases purification from electrophoresis gel is required in order to select the designed structure,

To achieve synthesis/construction of uniform circular metallic structures is still challenging via the bionano method. Therefore, more research into the metamaterial fabrication techniques must be carried out before it can be useful. In order to apply the bionano technique to metamaterial fabrication, much more must be understood about the behavior of these systems as the molecular and atomic scale in real time. The development in new observational and analytical techniques opens a new way to understand mechanistic details of biomolecular machines, which is essential if precise control of bionano fabrication processes is to be achieved. Even though we increasingly know many things about this small world compared to a couple of decades ago, there is still much to be explored.

References

1. Faraday, M., *The Bakerian Lecture: Experimental Relations of Gold (and Other Metals) to Light.* Phil. Trans. R. Soc. Lond., 1857. **147**(1): p. 145-181.
2. Taniguchi, N., *On the Basic Concept of 'Nano-Technology'.* Bulletin of the Japan Society of Precision Engineering, 1974: p. 18-23.
3. 高見誠一 and 阿尻雅文, *top-down method*, in *Comprehensive Nano-Bio Handbook* 2007, 株式会社テクノシステムズ. p. 359.
4. 嶋本伸雄, *ナノバイオ入門 ナノバイオロジーとナノバイオテクノロジー*. 新・生命科学ライブラリ-バイオと技術３2005, Tokyo: サイエンス社.
5. Moore, G.E., *Cramming More Components onto Integrated Circuits.* Electronics, 1965. **38**(8): p. 114-117.
6. Mulkens, J., et al. *Across scanner platform optimization to enable EUV lithography at the 10-nm logic node*. 2014.
7. Higashiguchi, T., A. Endo, and H. Mizoguchi, *Progress in Extreme Ultraviolet (EUV) Source Development.* J. Plasma Fusion Res., 2013. **89**(6): p. 341-348.
8. Heddle, J.G., *Protein cages, rings and tubes: useful components of future nanodevices?* Nanotechnology, science and applications, 2008. **1**: p. 67-78.
9. 科学技術庁研究開発局, *生体ナノ機構の解明のための基盤技術の開発に関する研究成果報告書* 1995.
10. 科学技術庁研究開発局, *生体ナノ機構の解明のための基盤技術の開発に関する研究成果報告書* 1998.
11. 嶋本伸雄, *ナノバイオロジー入門: 時間と空間の生物学* 1994, Tokyo: Kodansha.
12. 富澤純一, *分子生物学研究の流れ.* Protein, nucleic acid and enzyme, 1994. **39**(8): p. 1399-1409.
13. Hopcroft, N.H., et al., *The interaction of RNA with TRAP: the role of triplet repeats and separating spacer nucleotides.* Journal of molecular biology, 2004. **338**(1): p. 43-53.
14. Lundberg, K.S., et al., *High-fidelity amplification using a thermostable DNA polymerase isolated from Pyrococcus furiosus.* Gene, 1991. **108**(1): p. 1-6.
15. Shah, S.N., et al., *Template-free, hollow and porous platinum nanotubes derived from tobamovirus and their three-dimensional structure at the nanoscale.* RSC Advances, 2014. **4**(74): p. 39305-39311.
16. Watson, J.D. and F.H. Crick, *Molecular structure of nucleic acids; a structure for deoxyribose nucleic acid.* Nature, 1953. **171**(4356): p. 737-8.
17. Kendrew, J.C., et al., *A Three-Dimensional Model of the Myoglobin Molecule Obtained by X-Ray Analysis.* Nature, 1958. **181**(4610): p. 662-666.
18. Seeman, N.C., *Nucleic acid junctions and lattices.* Journal of theoretical biology, 1982. **99**(2): p. 237-47.
19. Chen, J.H. and N.C. Seeman, *Synthesis from DNA of a molecule with the connectivity of a cube.* Nature, 1991. **350**(6319): p. 631-3.
20. Mao, C., et al., *A nanomechanical device based on the B-Z transition of DNA.* Nature, 1999. **397**(6715): p. 144-6.

21. Rothemund, P.W., *Folding DNA to create nanoscale shapes and patterns.* Nature, 2006. **440**(7082): p. 297-302.

22. Douglas, S.M., et al., *Self-assembly of DNA into nanoscale three-dimensional shapes.* Nature, 2009. **459**(7245): p. 414-8.

23. Douglas, S.M., I. Bachelet, and G.M. Church, *A logic-gated nanorobot for targeted transport of molecular payloads.* Science, 2012. **335**(6070): p. 831-4.

24. He, Y., et al., *Hierarchical self-assembly of DNA into symmetric supramolecular polyhedra.* Nature, 2008. **452**(7184): p. 198-201.

25. Hamada, S. and S. Murata, *Substrate-assisted assembly of interconnected single-duplex DNA nanostructures.* Angewandte Chemie, 2009. **48**(37): p. 6820-3.

26. Goodsell, D.S. and A.J. Olson, *STRUCTURAL SYMMETRY AND PROTEIN FUNCTION.* Annual Review of Biophysics and Biomolecular Structure, 2000. **29**(1): p. 105-153.

27. Heddle, J.G., et al., *Using the ring-shaped protein TRAP to capture and confine gold nanodots on a surface.* Small, 2007. **3**(11): p. 1950-6.

28. Heddle, J.G., et al., *Rounding up: Engineering 12-membered rings from the cyclic 11-mer TRAP.* Structure (London, England : 1993), 2006. **14**(5): p. 925-33.

29. Miranda, F.F., et al., *A self-assembled protein nanotube with high aspect ratio.* Small (Weinheim an der Bergstrasse, Germany), 2009. **5**(18): p. 2077-84.

30. Malay, A.D., et al., *Gold Nanoparticle-Induced Formation of Artificial Protein Capsids.* Nano letters, 2012. **12**(4): p. 2056-2059.

31. King, N.P., et al., *Accurate design of co-assembling multi-component protein nanomaterials.* Nature, 2014. **510**(7503): p. 103-8.

32. Chen, C.-S., et al., *How to change the oligomeric state of a circular protein assembly: switch from 11-subunit to 12-subunit TRAP suggests a general mechanism.* PloS one, 2011. **6**(10): p. e25296-e25296.

33. Girit, Ç.Ö., et al., *Graphene at the Edge: Stability and Dynamics.* Science, 2009. **323**(5922): p. 1705-1708.

34. Sapsford, K.E., et al., *Analyzing Nanomaterial Bioconjugates: A Review of Current and Emerging Purification and Characterization Techniques.* Analytical chemistry, 2011. **83**(12): p. 4453-4488.

35. Ando, T., T. Uchihashi, and S. Scheuring, *Filming biomolecular processes by high-speed atomic force microscopy.* Chemical reviews, 2014. **114**: p. 3120-3188.

36. Ando, T., T. Uchihashi, and T. Fukuma, *High-speed atomic force microscopy for nano-visualization of dynamic biomolecular processes.* Progress in Surface Science, 2008. **83**(7-9): p. 337-437.

37. Uchihashi, T., N. Kodera, and T. Ando, *Guide to video recording of structure dynamics and dynamic processes of proteins by high-speed atomic force microscopy.* Nature protocols, 2012. **7**(6): p. 1193-206.

38. Ando, T., et al., *A high-speed atomic force microscope for studying biological macromolecules.* Proceedings of the National Academy of Sciences of the United States of America, 2001. **98**(22): p. 12468-72.

39. Ando, T., et al., *High-speed AFM and nano-visualization of biomolecular processes.* Pflugers Archiv : European journal of physiology, 2008. **456**(1): p. 211-25.

40. Imamura, M., et al., *Probing Structural Dynamics of an Artificial Protein Cage Using High-Speed Atomic Force Microscopy.* Nano letters, 2015. **15**(2): p. 1331-1335.

41. Turkevich, J., P.C. Stevenson, and J. Hillier, *A study of the nucleation and growth processes in the synthesis of colloidal gold.* Discussions of the Faraday Society, 1951. **11**(0): p. 55-75.

42. Frens, G., *Particle size and sol stability in metal colloids.* Kolloid-Zeitschrift und Zeitschrift für Polymere, 1972. **250**(7): p. 736-741.

43. Frens, G., *Controlled Nucleation for the Regulation of the Particle Size in Monodisperse Gold Suspensions.* Nature Physical Science, 1973. **241**(105): p. 20-22.

44. Brust, M., et al., *Synthesis of thiol-derivatised gold nanoparticles in a two-phase Liquid-Liquid system.* Journal of the Chemical Society, Chemical Communications, 1994(7): p. 801-802.

45. Elghanian, R., et al., *Selective colorimetric detection of polynucleotides based on the distance-dependent optical properties of gold nanoparticles.* Science, 1997. **277**(5329): p. 1078-81.

46. Storhoff, J.J., et al., *One-Pot Colorimetric Differentiation of Polynucleotides with Single Base Imperfections Using Gold Nanoparticle Probes.* Journal of the American Chemical Society, 1998. **120**(9): p. 1959-1964.

47. Saha, K., et al., *Gold nanoparticles in chemical and biological sensing.* Chemical reviews, 2012. **112**(5): p. 2739-79.

48. Tsukuda, T., *Toward an Atomic-Level Understanding of Size-Specific Properties of Protected and Stabilized Gold Clusters.* Bulletin of the Chemical Society of Japan, 2012. **85**(2): p. 151-168.

49. Corma, A., et al., *Exceptional oxidation activity with size-controlled supported gold clusters of low atomicity.* Nature chemistry, 2013. **5**(September): p. 775-81.

50. Heddle, J., *Gold Nanoparticle-Biological Molecule Interactions and Catalysis.* Catalysts, 2013. **3**(3): p. 683-708.

51. Yamazoe, S., K. Koyasu, and T. Tsukuda, *Nonscalable Oxidation Catalysis of Gold Clusters.* Accounts of Chemical Research, 2013. **47**(3): p. 816-824.

52. Taketoshi, A. and M. Haruta, *Size- and Structure-specificity in Catalysis by Gold Clusters.* Chemistry Letters, 2014. **43**(4): p. 380-387.

53. Corma, A., T. Ródenas, and M.J. Sabater, *Aerobic oxidation of thiols to disulfides by heterogeneous gold catalysts.* Chemical Science, 2012. **3**(2): p. 398-398.

54. Macfarlane, R.J., et al., *Topotactic interconversion of nanoparticle superlattices.* Science, 2013. **341**(6151): p. 1222-5.

55. Katz, E. and I. Willner, *Integrated Nanoparticle–Biomolecule Hybrid Systems: Synthesis, Properties, and Applications.* Angewandte Chemie International Edition, 2004. **43**(45): p. 6042-6108.

56. Daniel, M.-C. and D. Astruc, *Gold Nanoparticles: Assembly, Supramolecular Chemistry, Quantum-Size-Related Properties, and Applications toward Biology, Catalysis, and Nanotechnology*. Chemical reviews, 2004. **104**(1): p. 293-346.

57. Smith, D.R., J.B. Pendry, and M.C.K. Wiltshire, *Metamaterials and Negative Refractive Index.* Science, 2004. **305**(5685): p. 788-792.

58. Pendry, J.B., et al., *Magnetism from conductors and enhanced nonlinear phenomena.* Microwave Theory and Techniques, IEEE Transactions on, 1999. **47**(11): p. 2075-2084.

59. Tanaka, T., *Plasmonic metamaterials.* Ieice Electronics Express, 2012. **9**(2): p. 34-50.

60. Robinson, S. and R. Nakkeeran, *Photonic Crystal Ring Resonator Based Optical Filters*. Advances in Photonic Crystals2013.

61. Nazina, T.N., et al., *Taxonomic study of aerobic thermophilic bacilli: descriptions of Geobacillus subterraneus gen. nov., sp. nov. and Geobacillus uzenensis sp. nov. from petroleum reservoirs and*

transfer of Bacillus stearothermophilus, Bacillus thermocatenulatus, Bacillus thermoleovorans, Bacillus kaustophilus, Bacillus thermodenitrificans to Geobacillus as the new combinations G. stearothermophilus, G. th. International Journal of Systematic and Evolutionary Microbiology, 2001. **51**(2): p. 433-46.

62. Coorevits, A., et al., *Taxonomic revision of the genus Geobacillus: emendation of Geobacillus, G. stearothermophilus, G. jurassicus, G. toebii, G. thermodenitrificans and G. thermoglucosidans (nom. corrig., formerly 'thermoglucosidasius'); transfer of Bacillus thermantarcticus to the genus as G. thermantarcticus comb. nov.; proposal of Caldibacillus debilis gen. nov., comb. nov.; transfer of G. tepidamans to Anoxybacillus as A. tepidamans comb. nov.; and proposal of Anoxybacillus caldiproteolyticus sp. nov.* International Journal of Systematic and Evolutionary Microbiology, 2012. **62**(Pt 7): p. 1470-1485.

63. Notomi, T., et al., *Loop-mediated isothermal amplification of DNA.* Nucleic Acids Research, 2000. **28**(12): p. e63-e63.

64. Gollnick, P., et al., *The mtr locus is a two-gene operon required for transcription attenuation in the trp operon of Bacillus subtilis.* Proceedings of the National Academy of Sciences, 1990. **87**(22): p. 8726-8730.

65. Antson, A.A., J. Otridge, and A.M. Brzozowski, *The structure of trp RNA-binding attenuation protein.* Nature, 1995. **374**(20): p. 693-700.

66. Chen, X.P., et al., *Regulatory features of the trp operon and the crystal structure of the trp RNA-binding attenuation protein from Bacillus stearothermophilus.* Journal of molecular biology, 1999. **289**(4): p. 1003-1016.

67. Antson, a.a., et al., *Structure of the trp RNA-binding attenuation protein, TRAP, bound to RNA.* Nature, 1999. **401**(6750): p. 235-42.

68. Watanabe, M., et al., *The nature of the TRAP-Anti-TRAP complex.* Proceedings of the National Academy of Sciences of the United States of America, 2009. **106**(7): p. 2176-81.

69. Malay, A.D., et al., *Crystal structure of unliganded TRAP: implications for dynamic allostery.* The Biochemical journal, 2011. **434**(3): p. 427-34.

70. Gollnick, P., *Regulation of the Bacillus subtilis trp operon by an RNA-binding protein.* Molecular microbiology, 1994. **11**(6): p. 991-7.

71. Babitzke, P., *Regulation of transcription attenuation and translation initiation by allosteric control of an RNA-binding protein: the Bacillus subtilis TRAP protein.* Current opinion in microbiology, 2004. **7**(2): p. 132-9.

72. Gollnick, P., et al., *Complexity in regulation of tryptophan biosynthesis in Bacillus subtilis.* Annual review of genetics, 2005. **39**: p. 47-68.

73. Bayfield, O.W., et al., *Trp RNA-Binding Attenuation Protein: Modifying Symmetry and Stability of a Circular Oligomer.* PloS one, 2012. **7**(9): p. e44309.

74. Watanabe, M., Y. Mishima, and I. Yamashita, *Intersubunit linker length as a modifier of protein stability: crystal structures and thermostability of mutant TRAP.* Protein science, 2008. **17**: p. 518-526.

75. Leifert, A., et al., *Molecularly stabilised ultrasmall gold nanoparticles: synthesis, characterization and bioactivity.* Nanoscale, 2013. **5**(14): p. 6224-6242.

76. Leifert, A., et al., *Differential hERG ion channel activity of ultrasmall gold nanoparticles.* Proceedings of the National Academy of Sciences, 2013. **110**(20): p. 8004-8009.

77. Broda, J., G. Schmid, and U. Simon, *Size- and Ligand-Specific Bioresponse of Gold Clusters and Nanoparticles: Challenges and Perspectives*, in *Gold Clusters, Colloids and Nanoparticles I*, D.M.P. Mingos, Editor 2014, Springer International Publishing. p. 189-241.

78. Schmid, G., et al., *Large transition metal clusters—VI. Ligand exchange reactions on Au55(PPh3)12Cl6—the formation of a water soluble Au55 cluster.* Polyhedron, 1988. **7**(8): p. 605-608.

79. Periyasamy, G. and F. Remacle, *Ligand and Solvation Effects on the Electronic Properties of Au55 Clusters: A Density Functional Theory Study.* Nano letters, 2009. **9**(8): p. 3007-3011.

80. Schmid, G., *The relevance of shape and size of Au55 clusters.* Chemical Society reviews, 2008. **37**(9): p. 1909-1930.

81. Pan, Y., et al., *Size-dependent cytotoxicity of gold nanoparticles.* Small, 2007. **3**(11): p. 1941-9.

82. Ando, T., T. Uchihashi, and N. Kodera, *High-speed AFM and applications to biomolecular systems.* Annual review of biophysics, 2013. **42**: p. 393-414.

83. Yamamoto, D., et al., *High-speed atomic force microscopy techniques for observing dynamic biomolecular processes*. 1 ed. Vol. 475. 2010: Elsevier Inc. 541-64.

84. Nečas, D. and P. Klapetek, *Gwyddion: an open-source software for SPM data analysis.* Central European Journal of Physics, 2012. **10**(1): p. 181-188.

85. Schrodinger, LLC, *The PyMOL Molecular Graphics System, Version 1.3r1*, 2010.

86. Buxbaum, E. and SpringerLink (Online service), *Biophysical chemistry of proteins an introduction to laboratory methods*, 2011, Springer Science+Business Media, LLC,: New York. p. 1 online resource (xvi, 510 p.) ill. (some col.).

87. Lesne, A. and M. Laguës, *Diffusion*, in *Scale Invariance*2012, Springer Berlin Heidelberg. p. 109-165.

88. Arisaka, F., *バイオサイエンスのための蛋白質科学入門*. 第 3 版 ed2009: 裳華房.

89. Branden, C. and J. Tooze, *Introduction of Protein Structure (Japanese Edition)*. 2nd ed2000: Newton Press.

90. Arisaka, F., *超遠心分析*, in *バイオ高性能機器・新技術利用マニュアル* 2004, 共立出版. p. 1660-1667.

91. Lebowitz, J., M.S. Lewis, and P. Schuck, *Modern analytical ultracentrifugation in protein science: a tutorial review.* Protein science : a publication of the Protein Society, 2002. **11**(9): p. 2067-79.

92. Ulanovsky, L., et al., *Curved DNA: design, synthesis, and circularization.* Proceedings of the National Academy of Sciences, 1986. **83**(4): p. 862-866.

93. Hizver, J., et al., *DNA bending by an adenine--thymine tract and its role in gene regulation.* Proceedings of the National Academy of Sciences of the United States of America, 2001. **98**(15): p. 8490-5.

94. MacDonald, D., et al., *Solution structure of an A-tract DNA bend.* Journal of molecular biology, 2001. **306**(5): p. 1081-98.

95. Mirkin, C.A., et al., *A DNA-based method for rationally assembling nanoparticles into macroscopic materials.* Nature, 1996. **382**(6592): p. 607-9.

96. Lee, J.H., et al., *Site-Specific Control of Distances between Gold Nanoparticles Using Phosphorothioate Anchors on DNA and a Short Bifunctional Molecular Fastener.* Angewandte Chemie, 2007. **119**(47): p. 9164-9168.

97. Luduena, R.F., et al., *N,N-Bis(alpha-iodoacetyl)-2,2'-dithiobis(ethylamine), a reversible crosslinking reagent for protein sulfhydryl groups.* Analytical biochemistry, 1981. **117**(1): p. 76-80.

98. Zheng, J., et al., *Two-dimensional nanoparticle arrays show the organizational power of robust DNA motifs.* Nano letters, 2006. **6**(7): p. 1502-4.

99. Kuzyk, A., et al., *DNA-based self-assembly of chiral plasmonic nanostructures with tailored optical response.* Nature, 2012. **483**(7389): p. 311-4.

100. Young, K.L., et al., *Using DNA to Design Plasmonic Metamaterials with Tunable Optical Properties.* Advanced Materials, 2014. **26**(4): p. 653-659.

101. Watanabe-Tamaki, R., et al., *DNA-Templating Mass Production of Gold Trimer Rings for Optical Metamaterials.* The Journal of Physical Chemistry C, 2012. **116**(28): p. 15028-15033.

102. Krpetić, Ž., et al., *High-Resolution Sizing of Monolayer-Protected Gold Clusters by Differential Centrifugal Sedimentation.* ACS Nano, 2013. **7**(10): p. 8881-8890.

103. Haiss, W., et al., *Determination of Size and Concentration of Gold Nanoparticles from UV–Vis Spectra.* Analytical chemistry, 2007. **79**(11): p. 4215-4221.

104. Schmidt, T.L. and A. Heckel, *Pyrrole/imidazole-polyamide anchors for DNA tertiary interactions.* Small, 2009. **5**(13): p. 1517-20.

105. Liu, Y. and X. Zhang, *Metamaterials: a new frontier of science and technology.* Chemical Society reviews, 2011. **40**(5): p. 2494-2507.

106. Ohshiro, T., et al., *A facile method towards cyclic assembly of gold nanoparticles using DNA template alone.* Chemical communications, 2010. **46**(33): p. 6132-4.